

Phenomenology of Nonlinear Aeroelastic Responses of Highly Deformable Joined-wings Configurations

Rauno Cavallaro,* Andrea Iannelli† Luciano Demasi ‡ Alan Márquez Razón §

Dynamic aeroelastic behaviour of structurally nonlinear Joined Wings is presented. Three configurations, two characterized by a different location of the joint and one presenting a direct connection between the two wings (Sensorcraft-like layout) are investigated.

As a first step, the snap-divergence is studied from a dynamic perspective in order to assess the real response of the configuration. Later on, the investigations focus on the flutter occurrence (critical state) and go further in analyzing postcritical phenomena: Limit Cycle Oscillations (LCOs) are observed followed by a lost of periodicity of the solution as speed is further increased. In some cases, it is also possible to ascertain the presence of period doubling (flip-) bifurcation.

Differences between flutter (Hopf's bifurcation) speed evaluated with linear and nonlinear analyses are discussed in depth, in order to understand if a less computationally intense approach may be used with confidence.

Both frequency and time-domain approaches are compared. Moreover, aerodynamic solvers based on the potential flow are critically examined and discussed. In particular, it is assessed in what measure the use of more sophisticated (and computationally more intensive) aerodynamic and interface models impacts the aeroelastic predictions. These differences range from the methods adopted for load transferring to the models employed to describe the wake.

When the use of the tools gives different results, a physical interpretation of the leading mechanism generating the mismatch is provided. In particular, for PrandtlPlane-like configurations the aeroelastic response is very sensitive to the wake's shape. As a consequence, it is suggested that a more sophisticated modelling of the wake positively impacts the reliability of aerodynamic and aeroelastic analysis.

For Sensorcraft-like configurations some LCOs are characterized by a non-synchronous motion of the inner and outer portion of the lower wing: the wings' tip exhibits a small oscillation during the descending or ascending phase, whereas the mid-span station describes a sinusoidal-like trajectory in the time domain.

I. Introduction

THERE is currently great interest in innovative aircraft configurations. Among them, joined-wing concept [1, 2] has captured the attention as a possible candidate for the airplane of the future. However, it was argued and also demonstrated that a reasonably accurate conceptual/preliminary design is hard to be pursued due to inherent structural nonlinearities that may invalidate the results obtained with fast lower-fidelity tools, which are a necessity when exploring the large parameter's space typical of the early design stages. For example, references [3–5] showed non-negligible differences when comparing structural responses obtained with linear and nonlinear capabilities. As a consequence, consolidated design strategies and tools developed in decades, and effectively used by the industry, have to be reviewed. This represents one of the major barriers to the development of Joined Wings [6].

*PhD Candidate, Department of Aerospace Engineering, San Diego State University and Department of Structural Engineering, University of California San Diego, AIAA Member

†Visiting Graduate Student, San Diego State University, MS Candidate at the Dipartimento di Ingegneria Aerospaziale, Università di Pisa.

‡Associate Professor, Department of Aerospace Engineering, San Diego State University, Lifelong AIAA Member

§Undergraduate Student, Department of Aerospace Engineering, San Diego State University

The need to include these structural nonlinearities early in the design has pushed the researchers to try to achieve computational efficiency with reduced order models [7, 8]. However, results in this direction have not been quite encouraging. Some recent results are shown in references [9, 10].

The situation outlined in reference [11] goes well beyond a bad prediction of the critical condition. It is in fact shown that, bi-stability is possible and thus, catastrophic branch-jumping may eventually arise well before the static limit condition is reached. The only tool to detect such regions is a nonlinear full post-critical analysis (branch tracking). Actually, this may not be enough to plot the complete static equilibrium diagram: in reference [12] *isola*-type of bifurcations are shown.

When assessing joined-wing behaviour from a static aeroelastic perspective, similar problems were noticed [13] in terms of presence of bi-stable regions, and the snap-divergence concept was introduced. The strong structural nonlinearities have demonstrated to be dominant also for small angles of attack and attached flow, which can be considered linear.

However, a complete scenario of the aeroelastic properties may be sketched only by nonlinear dynamic investigations. To the best of authors' knowledge, nonlinear aeroelastic dynamic analysis was pursued only in a few efforts, i.e. references [14, 15]. The first of these preliminary studies showed how the flutter speed prediction varied when using a nonlinear modelling of the structure, whereas the second studied a limit cycle oscillation.

The effort of the present paper is in the direction of showing, studying and gaining insight into the dynamic aeroelastic phenomena inherent to these configurations, and which have potential impact on the design of Joined Wings.

II. Contribution of the Present Study

The numerical investigations presented in references [4, 5, 11, 13, 16] characterized the response of Joined Wings on a conceptual level. In particular, a snap-instability was first found when statically loading the structure with mechanical forces. The occurrence of such kind of instability (saddle-node bifurcation, refer to [17] for more details) was also observed when mechanical forces of a follower type or aerodynamic loads were considered. For the true aeroelastic case, the static instability was named *snap-divergence*, in order to resemble the true snap-phenomenon that was arising in the pure mechanical case, even if a real snap may practically not occur due to the nonconservative nature of aerodynamic forces. One of the contributions of this paper is the study of this phenomenon from a dynamic point of view: after assessing, by means of a series of linearized frequency-domain analyses, that the flutter speed is higher than the snap-divergence one, the true dynamic response will be shown.

In reference [13] the *snap-divergence* was compared to the traditional divergence analysis, performed through an eigenvalue analysis about particular configurations (usually the undeformed one). Discrepancy between the critical speeds predicted by these two approaches was substantial. Moreover, the traditional eigenvalue approach was overpredicting the divergence speed. It is then expected a mismatch also between flutter speeds evaluated by means of linear and nonlinear flutter analyses. This will be shown to be important and to have a similar trend as the one found for the divergence analysis: linear tools overpredict the flutter speed, at least for the considered configurations. The above comparison is further augmented by considering different damping ratios and by incorporating time domain analyses.

Assessment of flutter speed gives a local information about loss of stability (Hopf's bifurcation), however, does not provide a picture of what happens in the post-critical region (see the works cited in reference [18] for a comprehensive literature review). With the aid of different time-domain capabilities LCOs are shown. For the Sensorcraft-like case, it is found an asynchronous motion between the outer and inner part of the lower wing: while the inner part moves in a wave-like pattern, the outer part has a small localized oscillation during the ascending or descending portion of the periodic motion.

A peculiarity of some joined-wing configurations is that, for higher speed, further bifurcation phenomena as *period doubling* [17–20] occur. Moreover, loss of periodicity can also be observed when speed is further increased, suggesting that a transition to chaos may be in place. On the other hand, for other joined-wing layouts experiencing an LCO, increasing the speed may have the opposite effect, leading to a stable state.

A very important and often neglected fact is the level of confidence that should be given to solvers employed for investigating the aeroelastic problem. A first differentiation is made by frequency domain and time domain tools. In some of the present numerical experiments both of these techniques are used. For the time domain approach, different options are provided. However, some preliminary theoretical discussions are

necessary. For example, studies on delta wings showed that when the structural nonlinearities are important they may also drive the limit cycle oscillation much more than the aerodynamic effects do. References [21–23] are a good example: the response was mainly driven by the structural nonlinearities. Considering the strongly nonlinear (on the structural side) response of Joined Wings, it is then natural to investigate under which conditions the structural geometric nonlinearities play an important role in the development of limit cycle oscillation, which may appear even for a completely attached flow and linear aerodynamics. Even within these reasonable assumptions there are different level of approximations. In this paper effects of load/displacements transferring methods (splining, [24], meshless [25]), different way of distributing the aerodynamic singularities (on an undeformable reference plane or attached to the body) as well as modelling of the wake (rigid or free) are evaluated. It will be shown that solvers implementing different assumptions may lead to considerably different results. This is especially true for PrandtlPlane configurations, for which aerodynamic load redistribution have a major impact on aeroelastic performances: wake deformation is then a factor to take account of.

It is important to collocate this effort in an historical and bibliographical context. Flutter analysis of Joined Wings was first performed in reference [26], for a box-wing layout [27]. It was found that the flutter instability was a limitation to the design of the configuration. Later, [28, 29] the so called *PrandtlPlane* [30–32] configuration was studied on an aeroelastic perspective and the encountered flutter problems were alleviated with the introduction of a double fin. In the above references linear flutter prediction methods were used. Moreover, the analyses were carried out on a *realistic* (i.e, inertial and stiffness distributions were assessed considering real-like operative conditions) aircraft, whereas conceptual investigations on wind-tunnel-like models will be pursued in this paper.

However, as shown in reference [13] for the static aeroelastic case and in this paper for the dynamic aeroelastic one, linear results could be non-conservative since higher critical speeds may be predicted. If a large discrepancy between the linear and nonlinear predicted aeroelastic instability speeds is found on the conceptual models, then a qualitative indication on the actual aircraft is implicitly provided.

Very few results have been proposed for different layouts of Joined Wings [15], and a lack of understanding of the physics of the phenomenon is evident: additional studies are then necessary.

III. Theoretical Highlights of the Present Computational Tools

In a generic aeroelastic code the basic aerodynamic and structural solvers need to interact, passing to each other the information regarding the deformations (which directly influence the aerodynamic forces) and the forces (which deform the structure). It goes well beyond the goals of this paper to present a summary of all the possible strategies that could be adopted. The authors refer the reader to excellent works as [33–35] and the herein cited references.

In the following, the *components* of the in-house aeroelastic capabilities are described separately. They consist in a finite element method for the computational structural dynamics (CSD) and an unsteady vortex lattice method (UVLM) for the time domain aerodynamic simulations. A doublet lattice method (DLM) for the frequency domain unsteady aerodynamics calculations is also employed: details about this particular solver could be found in literature, see references [36–38].

Hereinafter, different interface (load/displacement transferring) strategies are analyzed.

Finally, the coupling is treated, and the different aeroelastic solvers are discussed.

A. Structural Finite Element Model

The geometrically nonlinear finite element [39–42] is based on the linear membrane constant strain triangle (CST) and the flat plate discrete Kirchhoff triangle (DKT). The capability has also embedded the calculation of the structural tangent matrix \mathbf{K}_T , which is the sum of two contributions: the elastic stiffness matrix, \mathbf{K}_E , and the geometric stiffness matrix, \mathbf{K}_G . Composite materials are implemented. A corotational approach is used, and thus, rigid body motion is eliminated from elements and the pure elastic deformations are found.

The post-critical capability of the structural, and also aeroelastic code, are here omitted for brevity. The reader is referenced to [11, 13] for details.

B. Dynamic Solver

1. Newton's Law and Definition of the Residual

According to the second Newton's law, at each time dynamic equilibrium has to be satisfied. Let \mathbf{s} be the generalized coordinate array (arising from the FE discretization) and $\dot{\mathbf{s}}$, $\ddot{\mathbf{s}}$ its time derivatives. Assume \mathbf{M} to be the mass matrix, and that the damping forces, related to the structural damping, are proportional to $\dot{\mathbf{s}}$ through the damping matrix \mathbf{C}_d , constant with time. The internal structural forces are indicated with \mathbf{F}_{int} . Since only elastic materials are considered, these forces are function of the deformation only. The external loads are here specialized to be the aerodynamic forces acting on the body, and are a generical function of t , \mathbf{s} , $\dot{\mathbf{s}}$ and $\ddot{\mathbf{s}}$. These dependencies are related to the history (wake evolution), current configuration (steady production of aerodynamic forces), velocity of deformation (which changes the local angle of attack) and acceleration of deformation, respectively.

The dynamic equilibrium law reads as follows:

$$\mathbf{M} \ddot{\mathbf{s}} + \mathbf{C}_d \dot{\mathbf{s}} = \mathbf{P}_{\text{ext}}(\mathbf{s}, \dot{\mathbf{s}}, \ddot{\mathbf{s}}, t) - \mathbf{F}_{\text{int}}(\mathbf{s}) \quad (1)$$

The residual is then defined as:

$$\mathcal{R}(\mathbf{s}, \dot{\mathbf{s}}, \ddot{\mathbf{s}}, t) = \mathbf{M} \ddot{\mathbf{s}} + \mathbf{C}_d \dot{\mathbf{s}} - (\mathbf{P}_{\text{ext}}(\mathbf{s}, \dot{\mathbf{s}}, \ddot{\mathbf{s}}, t) - \mathbf{F}_{\text{int}}(\mathbf{s})) \quad (2)$$

In order to obtain the dynamic equilibrium the residual has to be zero at each generic time t . However, when the problem is discretized in respect to the time, it is possible to enforce the dynamic equilibrium only at some temporal points. In literature several methods exist for the time discretization of dynamic structural problems, see for example [43–45].

In the following, the framework of the Newmark's β -Method and successive improvements leading to the *Generalized α -Method* (GAM) are introduced. The reasons that led to the introduction of the so called *Generalized Energy-Momentum Method* (GEMM) and its implementation are then presented (see reference [46] for more details).

2. From Newmark β -Method to the Generalized α -Method

Before further proceeding, the notation used to state the evaluation of the quantity \mathbf{A} at the generic time t is introduced:

$${}^t \mathbf{A} = \mathbf{A}|_t \quad (3)$$

If the generic quantity \mathbf{A} has both a direct and indirect dependence on time, for example $\mathbf{A}(\mathbf{s}(t), t)$, then the notation is the following:

$${}^t \mathbf{A} = \mathbf{A}|_{(\mathbf{s}|_t, t)} \quad (4)$$

In reference [47], to advance in time from t to $t + \Delta t$, Newmark proposed the following relation between acceleration, velocity and displacement vectors:

$$\begin{aligned} {}^{t+\Delta t} \dot{\mathbf{s}} &= {}^t \dot{\mathbf{s}} + (1 - \gamma) \Delta t {}^t \ddot{\mathbf{s}} + \gamma \Delta t {}^{t+\Delta t} \ddot{\mathbf{s}} \\ {}^{t+\Delta t} \mathbf{s} &= {}^t \mathbf{s} + \Delta t {}^t \dot{\mathbf{s}} + (1 - 2\beta) \frac{\Delta t^2}{2} {}^t \ddot{\mathbf{s}} + \beta \Delta t^2 {}^{t+\Delta t} \ddot{\mathbf{s}} \end{aligned} \quad (5)$$

The process was driven by Taylor's expansion and mean value theorem. The choice of γ and β determines important characteristics as accuracy, rate of convergence, stability and the alternatively explicit or implicit nature of the scheme [43]. Common choice is to take:

$$\gamma = \frac{1}{2} \quad \beta = \frac{1}{4} \quad (6)$$

which gives an unconditionally stable (irrespective of the size of the time step Δt) and quadratic convergent scheme (this has been proven for linear problems [48]).

With reference to eq.(2), it is straightforward to impose the dynamic equilibrium at the generic time $t + \Delta t$,

$${}^{t+\Delta t} \mathcal{R} = \mathbf{M} {}^{t+\Delta t} \ddot{\mathbf{s}} + \mathbf{C}_d {}^{t+\Delta t} \dot{\mathbf{s}} - ({}^{t+\Delta t} \mathbf{P}_{\text{ext}} - {}^{t+\Delta t} \mathbf{F}_{\text{int}}) = \mathbf{0} \quad (7)$$

and apply the scheme proposed in eq.(5).

It is desirable in structural dynamic problems solved through step-by-step time integration algorithms to possess *algorithmic damping*. Particularly, it is necessary to control the dissipation on the high frequency modes since using standard FEM to discretize the spatial domain, the spatial resolution of these modes is poor. Thus, spurious high frequency modes should be damped out, and this should affect neither the low frequency modes nor the accuracy of the scheme. For example, the Newmark β -method family algorithms provide high-frequency dissipation if a different choice of the parameters in eq.(6) is made, with the drawbacks of an only first-order accuracy in time and too much dissipation on the low frequency modes [49]. This has driven the formulation of improved methods that enable to overcome these limitations, maintaining second-order accuracy: the HHT- α [50] and the WBZ- α [51] methods are just some examples. All these schemes are particular cases of the more general *Generalized α -method* (GAM), which represents a family of implicit time-integration schemes, and has been introduced in reference [49].

The scheme giving the relationships between the values of \mathbf{s} , $\dot{\mathbf{s}}$ and $\ddot{\mathbf{s}}$ is the same carried out in eq.(5), but now the additional equation needed to close the problem is a modified version of the standard choice of eq.(7): the idea is to force the dynamic equilibrium using convex combinations of these variables. Defining the following quantities:

$$\begin{cases} {}^{t+\alpha_f\Delta t}\mathbf{s} = (1 - \alpha_f) {}^t\mathbf{s} + \alpha_f {}^{t+\Delta t}\mathbf{s} \\ {}^{t+\alpha_f\Delta t}\dot{\mathbf{s}} = (1 - \alpha_f) {}^t\dot{\mathbf{s}} + \alpha_f {}^{t+\Delta t}\dot{\mathbf{s}} \\ {}^{t+\alpha_m\Delta t}\ddot{\mathbf{s}} = (1 - \alpha_m) {}^t\ddot{\mathbf{s}} + \alpha_m {}^{t+\Delta t}\ddot{\mathbf{s}} \end{cases} \quad (8)$$

where, differently from the previously adopted notation, the superscripts are here used to indicate a convex combination of the values at the beginning (t) and at the end ($t + \Delta t$) of the time step and not values evaluated at time $t + \alpha\Delta t$. Clearly, $\alpha_m = \alpha_f = 1$ gives rise to the Newmark family of methods.

The task is now to determine the relations between the algorithmic parameters α_m , α_f , γ and β to gain the desired numerical features. It can be demonstrated [49] that the generalized α -method is second-order accurate, provided that

$$\begin{aligned} \gamma &= \frac{1}{2} + \alpha_m - \alpha_f \\ \beta &= \frac{1}{4} (1 + \alpha_m - \alpha_f)^2 \end{aligned} \quad (9)$$

The stability property of an algorithm applied to linear problems depends upon the eigenvalues of its amplification matrix, in particular on spectral radius ϱ (defined as the largest of the eigenvalues). The spectral radius is also important because it is a measure of the numerical dissipation, that is a smaller spectral radius value corresponds to a larger numerical dissipation; to obtain a numerical algorithm which gives the desired numerical damping at the high frequencies without an excessive dissipation in the low frequency region, its spectral radius should then be close to unity in the low frequency domain and smoothly decrease as the frequency increases. Summarizing, see [49] for details, it is possible to have a second order (in time) accurate unconditionally stable (for linear problems) scheme, which has a user-defined dissipation on the high frequencies and minimizes the dissipation on lower frequencies if, along with eq.(9), the following is also satisfied:

$$\begin{aligned} \alpha_f &= \frac{1}{1 + \varrho_\infty} \\ \alpha_m &= \frac{2 - \varrho_\infty}{1 + \varrho_\infty} \end{aligned} \quad (10)$$

where ϱ_∞ denotes the value of the spectral radius in the high-frequency limit (ϱ_∞ is then the user-specified value to control high-frequency dissipation).

Application of this method to eq.(2) is not straightforward. In fact, in literature [44, 49], this procedure has been developed mainly for linear cases in which the forces were depending on time or displacements only. Thus, using the convex combination of eq.(8) would be completely identical to the case in which the convex combination is used for the different term of the residual. However, in the present case, there is a force term depending nonlinearly from the displacement (\mathbf{F}_{int}) and one term depending on t , \mathbf{s} , $\dot{\mathbf{s}}$ and $\ddot{\mathbf{s}}$ (\mathbf{P}_{ext}).

Focus is now on the external forces. One option is to remain consistent with the evaluation in time dictated by eq.(8), i.e., to set the external/aerodynamic forces evaluated at different convex combinations of the displacement and derivatives vectors:

$$\mathbf{P}_{\text{ext}} \Big|_{({}^{t+\alpha_f\Delta t}\mathbf{s}, {}^{t+\alpha_f\Delta t}\dot{\mathbf{s}}, {}^{t+\alpha_m\Delta t}\ddot{\mathbf{s}}, t+\alpha_f\Delta t)} \quad (11)$$

A peculiarity of such an approach is that, in cases for which an explicit linear dependence of the external forces on the displacements, velocities, accelerations, and a dependence (not necessarily linear) on time is found, the residual (eq.(2)) could be written as:

$$\mathcal{R}(\mathbf{s}, \dot{\mathbf{s}}, \ddot{\mathbf{s}}, t) = \left(\mathbf{M} - \mathbf{M}^A \right) \ddot{\mathbf{s}} + \left(\mathbf{C}_d - \mathbf{C}_d^A \right) \dot{\mathbf{s}} - \mathbf{K}^A \mathbf{s} - \left(\mathbf{P}_{\text{ext}}^A(t) - \mathbf{F}_{\text{int}}(\mathbf{s}) \right) = \mathbf{0} \quad (12)$$

where \mathbf{M}^A , \mathbf{C}_d^A and \mathbf{K}^A express the linear dependence of the aerodynamic forces, and $\mathbf{P}_{\text{ext}}^A(t)$ represents the time dependence. Thus, except for the internal forces, the application of the GAM closely matches what explained in reference [49]. Applying this first approach also to the internal forces, the discrete equation for the residual can be written as:

$${}^{t+\Delta t}\mathcal{R} = \mathbf{M} {}^{t+\alpha_m\Delta t}\ddot{\mathbf{s}} + \mathbf{C}_d {}^{t+\alpha_f\Delta t}\dot{\mathbf{s}} - \mathbf{P}_{\text{ext}}|_{(t+\alpha_f\Delta t, \mathbf{s}, {}^{t+\alpha_f\Delta t}\dot{\mathbf{s}}, {}^{t+\alpha_m\Delta t}\ddot{\mathbf{s}}, t+\alpha_f\Delta t)} + \mathbf{F}_{\text{int}}|_{(t+\alpha_f\Delta t, \mathbf{s})} \quad (13)$$

Consider now the internal forces. If the structural model is linear, then

$$\mathbf{F}_{\text{int}}|_{(t+\alpha_f\Delta t, \mathbf{s})} = {}^{t+\alpha_f\Delta t}\mathbf{F}_{\text{int}} \quad (\text{for linear structures}) \quad (14)$$

which is equivalent to consider a convex combination of the terms of the residual equation or the displacement. This no longer holds if the forces are nonlinear. Thus the question arises as to which form should be considered.

3. Generalized Energy-Momentum Method

To apply a convex combination directly to the edge values of the internal and external loads and not to the displacements, proves to be very important for the properties of the numerical scheme, in particular the stability one. In fact, algorithms which are unconditionally stable for linear dynamics often lose this stability in the non-linear case, see for example references [44, 48, 52–56]. This is also true if algorithmic damping, as evaluated with linear approach (like in [49]) is introduced. A further criterion for the stability of time-integration algorithms (other than the eigenvalue analysis shown earlier for the Generalized α -method) is the conservation of energy, motivated by the theorem presented in reference [57] which states that, when applied to Hamiltonian systems, a numerical algorithm is stable in energy if the sum of kinetic and internal energies are bounded within each time step relative to the external work, kinetic and internal energies in the previous time step.

The first algorithm which guaranteed unconditional stability in nonlinear dynamics of three-dimensional elastic bodies was the Energy-Momentum Method [58]. Actually, its appeal has been redimensioned by some numerical experiments, see [55, 56, 59]. In fact, convergence problems were observed, and small time steps were needed to obtain a stable and converged solution. These difficulties have been put in relation to high modes which are responsible of numerical collapse driven by an unphysical highly oscillatory response. It seems then advisable to introduce some form of damping in order to keep under control difficult cases [56].

A strategy to introduce controllable numerical dissipation to the Energy-Momentum Method, denoted as Generalized Energy-Momentum Method was presented in references [55, 46], applied to three-dimensional truss element and nonlinear dynamics of shells. It includes numerical dissipation adopting the Generalized α -method to advance the solution within time and guarantees the energy conservation or decay using the convex combination of the internal forces at the beginning and at the end of the time interval, ${}^{t+\alpha_f\Delta t}\mathbf{F}_{\text{int}}$ instead of considering it applied at the generalized midpoint, $\mathbf{F}_{\text{int}}|_{(t+\alpha_f\Delta t, \mathbf{s})}$.

Unfortunately, is it not possible to automatically extend this approach to the aerodynamic forces, since the simultaneous dependence on acceleration, velocity and displacement does not make straightforward the use of a unique convex combination: it would be an open question which value between α_f and α_m should be used on this regard. In this effort, both the option ${}^{t+\alpha_f\Delta t}\mathbf{P}_{\text{ext}}$, namely:

$${}^{t+\alpha_f\Delta t}\mathbf{P}_{\text{ext}} = (1 - \alpha_f) {}^t\mathbf{P}_{\text{ext}} + \alpha_f {}^{t+\Delta t}\mathbf{P}_{\text{ext}} \quad (15)$$

and the one previously introduced in eq.(11), have been used. Notice also that, in other works like [60], different convex combinations were suggested for the external forces. Summarizing, the strategy adopted to discretize in time the equations of motion is the GEMM, whereas the aerodynamic term is evaluated with a GAM or also a GEMM-like approach. Notice that, for the particular considered cases, no appreciable differences were noticed between the two approaches.

In the following, the derivation of the Newton process for convergence is shown for the GEMM-like approach only. The residual equation becomes:

$${}^{t+\Delta t}\mathcal{R} = \mathbf{M} \left((1 - \alpha_m) {}^t\ddot{\mathbf{s}} + \alpha_m {}^{t+\Delta t}\ddot{\mathbf{s}} \right) + \mathbf{C}_d \left((1 - \alpha_f) {}^t\dot{\mathbf{s}} + \alpha_f {}^{t+\Delta t}\dot{\mathbf{s}} \right) - (1 - \alpha_f) {}^t\mathbf{P}_{\text{ext}} - \alpha_f {}^{t+\Delta t}\mathbf{P}_{\text{ext}} + (1 - \alpha_f) {}^t\mathbf{F}_{\text{int}} + \alpha_f {}^{t+\Delta t}\mathbf{F}_{\text{int}} \quad (16)$$

It is important to notice that, considering a generic time t in which all the quantities are known, and wishing to advance in time to $t + \Delta t$, it is possible, by means of eqs.(5), to reduce the residual to a function of only one variable. Thus,

$${}^{t+\Delta t}\mathcal{R} = \mathcal{R} ({}^{t+\Delta t}\mathbf{s}) \quad (17)$$

4. Newton's Method Applied to the Residual

A generic zero finding methods could be applied to eq.(16) (or alternatively, eq.(13)) in order to drive to zero the residual and thus obtain the dynamic equilibrium. If Newton's method is used then the residual is locally approximated with an affine model and the new linearly predicted zero is considered. A single Newton's iteration reads:

$$\mathbf{0} = {}^{t+\Delta t}\mathcal{R}^{\text{iter } n} + \left[\frac{d\mathcal{R}}{d\mathbf{s}} \right]^{\text{iter } n} \cdot {}^{t+\Delta t}\mathbf{u}^{\text{iter } n} \quad (18)$$

where the superscript "iter n " specifies the iteration at which the quantities are considered. The symbolism

$$\left[\frac{d\mathcal{R}}{d\mathbf{s}} \right]^{\text{iter } n} \quad (19)$$

indicates the tangent matrix evaluated at ${}^{t+\Delta t}\mathbf{s}^{\text{iter } n}$, and it holds:

$${}^{t+\Delta t}\mathbf{s}^{\text{iter } n+1} = {}^{t+\Delta t}\mathbf{s}^{\text{iter } n} + {}^{t+\Delta t}\mathbf{u}^{\text{iter } n} \quad (20)$$

The tangent matrix for the system is:

$${}^{t+\Delta t} \left[\frac{d\mathcal{R}}{d\mathbf{s}} \right] = \frac{\alpha_m}{\beta \Delta t^2} \mathbf{M} + \frac{\alpha_f \gamma}{\beta \Delta t} \mathbf{C}_d - \alpha_f \left(\frac{d {}^{t+\Delta t}\mathbf{P}_{\text{ext}}}{d {}^{t+\Delta t}\mathbf{s}} - \frac{d {}^{t+\Delta t}\mathbf{F}_{\text{int}}}{d {}^{t+\Delta t}\mathbf{s}} \right) \quad (21)$$

where the iteration superscript has been dropped for clarity. Notice that eq.(21) changes during iterations only if the internal structural forces \mathbf{F}_{int} or the external (aerodynamic) loads \mathbf{P}_{ext} are nonlinear with ${}^{t+\Delta t}\mathbf{s}$. Notice also the contribution of the structural tangent matrix and force (aerodynamic) tangent matrix to the system's/global tangent one.

Once the iterative process reaches a convergent state, then a new time step could be taken and the iterative sequence repeated.

5. Structural Damping

The structural model provides the possibility to reproduce more consistently the dynamic behaviour taking into account the presence of structural damping, represented by the damping matrix \mathbf{C}_d ; the approach consists in the extrapolation of structural modal damping from the system. Considering a problem with one degree of freedom, the free spring-damping-mass system is described by the equation

$$m \ddot{s} + 2c \dot{s} + k s = 0 \quad (22)$$

being s the generic coordinate describing the motion, m the mass, c the damping coefficient and k the spring constant. Rearranging the equation, the canonical form is easily obtained:

$$\ddot{s} + 2\zeta \omega_n \dot{s} + \omega_n^2 s = 0 \quad (23)$$

where ω_n represents the natural frequency of the system and ζ the damping ratio (common values are in the range of $0.01 \div 0.05$). Once eq.(22) is stated in canonical form and ζ is chosen, the damping coefficient c is automatically set.

If the system has more than one degree of freedom, and the differential equations of motion are *linear*, it is possible, by means of the so called light damping approximation [61], to describe the evolution of the system decoupling the evolution of each natural mode. Thus, for the generic i -th mode the following relation holds:

$$\ddot{q}_i + 2\zeta_i\omega_{n_i}\dot{q}_i + \omega_{n_i}^2q_i = 0 \quad (24)$$

which in matrix form is written as

$$\ddot{\mathbf{q}} + \mathbf{C}_\Delta \dot{\mathbf{q}} + \mathbf{\Omega} \mathbf{q} = \mathbf{0} \quad (25)$$

The introduction of damping to the lower frequencies influences the solution so it is necessary only to model a physical phenomenon and in this sense eq.(24) represents a convenient strategy that gives the possibility to set this damping factor for each mode independently.

The next step is to be able to relate the modal form of the equation (where the modal damping ratio ζ_i could be set) to the generic n -dimensional system which describes the dynamic behaviour of the degrees of freedom of the structure (\mathbf{s}):

$$\mathbf{M} \ddot{\mathbf{s}} + \mathbf{C}_d \dot{\mathbf{s}} + \mathbf{K} \mathbf{s} = \mathbf{0} \quad (26)$$

The matrices are constant, and it is possible to write the response as a superposition of elementary solutions through the modal coordinates \mathbf{q} :

$$\mathbf{s} = \mathbf{\Phi} \mathbf{q} \quad (27)$$

where $\mathbf{\Phi}$ is the modal matrix. Substituting eq.(27) into eq.(26) and pre-multiplying by $\mathbf{\Phi}^T$, it holds

$$\hat{\mathbf{M}} \ddot{\mathbf{q}} + \hat{\mathbf{C}} \dot{\mathbf{q}} + \hat{\mathbf{K}} \mathbf{q} = \mathbf{0} \quad (28)$$

where, using the properties of the modal coordinates, it is possible to show that the modal mass $\hat{\mathbf{M}}$ and stiffness $\hat{\mathbf{K}}$ matrices are diagonal. The aim is to define \mathbf{C}_d through $\hat{\mathbf{C}}$. The first step is to assume that $\hat{\mathbf{C}}$ is diagonal, so that it is straightforward to write eq.(24) for the generic i -th generalized coordinate. It is then possible to define the damping ratios for each mode in this form, and reconstruct the matrix \mathbf{C}_d using the inverse of relation eq.(27) and left-multiplying by $\mathbf{\Phi}^{-T}$, namely:

$$\mathbf{C}_d = \mathbf{\Phi}^{-T} \hat{\mathbf{C}} \mathbf{\Phi}^{-1} \quad (29)$$

Actually the dynamic behaviour of a system is ruled by the most meaningful modes that are associated with the low natural frequencies, so it can be preferable both from a computational and (numerical) accuracy point of view to consider the process for just n modes on which it is significant to apply the damping, see reference [37]. If N is the total number of degrees of freedom of the structure, $\mathbf{\Phi}$ is now an $N \times n$ matrix; eq.(29) could not be used since $\mathbf{\Phi}$ is not a square matrix. To perform a similar equivalence, but in a least square sense, the following operations are performed starting from eq.(27):

$$\begin{aligned} \mathbf{\Phi}^T \mathbf{s} &= \mathbf{\Phi}^T \mathbf{\Phi} \mathbf{q} \\ \mathbf{T} &= [\mathbf{\Phi}^T \mathbf{\Phi}]^{-1} \mathbf{\Phi}^T \\ \mathbf{T} \mathbf{s} &= \mathbf{q} \\ \mathbf{C}_d &= \mathbf{T}^T \hat{\mathbf{C}} \mathbf{T} \end{aligned} \quad (30)$$

C. Aerodynamic model

1. Introduction

The present section introduces the aerodynamic model adopted in the study. The hypotheses of potential and incompressible flow are assumed to be valid.

2. Geometry Definition and Evaluation of Induced Velocity

Unsteady Vortex Lattice Method (UVLM) is used as aerodynamic solver: the main advantage of such a formulation is the required simple programming effort, which makes it preferable when operating with thin wings; for a detailed treatise refer to [62].

The singularities are vortex ring elements, each of which is composed by four constant-strength vortex line segments with the same value of circulation Γ . The wing is discretized by an arbitrary user selected

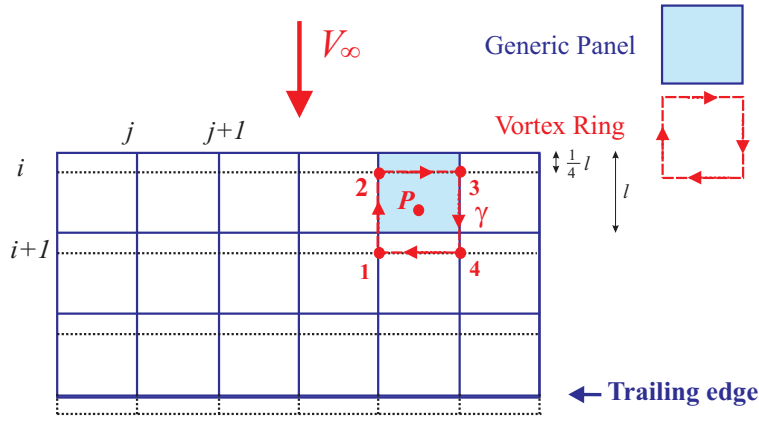


Fig. 1. Location of the vortex rings in the aerodynamic grid.

number of quadrilateral aerodynamic panels as shown in Fig. 1. The vortex ring associated with each panel is shift downstream along each lateral edge of one fourth of the same edges. The velocity induced at an arbitrary point P by the generic vortex segment of circulation Γ is obtained from the Biot-Savart law. In particular, assume $\mathbf{V}_{\text{SI}_{km}}$ to be the velocity induced in the k -th collocation (or control) point by m -th ring of unitary circulation. Moreover, consider that the generic k -th collocation point (where the wall tangency condition has to be enforced), lies on the *center* of the k -th vortex ring, whose local direction is \mathbf{n}_k . Then, it is possible to define the generic km -th term of matrix of body influence coefficients \mathbf{A} :

$$\mathbf{A}_{km} = \mathbf{V}_{\text{SI}_{km}} \cdot \mathbf{n}_k \quad (31)$$

3. Wake Model

For an unsteady flow a key role is played by the modelling of the wake. The most accurate model prescribes that each vortex moves with the local stream velocity since the vortex wake is force free, obtaining the so called *wake roll-up*. However this approach is quite time consuming and so often a simpler one, consisting in assuming a prescribed shape for the wake, is adopted. The effects of wake modelling on the aeroelastic responses will be discussed later.

In both cases, the wake is modelled with several rows of vortex rings of different strength, each shed at a certain time-step. When impulsively starting from a rest condition, only wing bound vortex rings exist. Consequently, there are no wake panels and the solution is easily found by specifying the zero normal flow boundary condition on the collocation points. During the second time step, the wing moves along its flight path and each trailing edge vortex panel sheds a wake ring with a vortex strength equal to its circulation in the previous time step (automatically satisfying the Kelvin condition). For the case of prescribed wake, it is enough to impose that each wake's point is convected by the free-stream velocity and so the procedure can be continued at each successive time step determining in such a way a wake of known geometry. Notice that, a wake vortex ring does not change its circulation (consequence of Helmholtz theorem). If the free wake is modelled, at the end of each timestep, once the problem is solved and the unknown intensity of the circulation Γ of every ring of the body is known, the evaluation of the induced velocity (u, v, w) at each vortex ring corner point l is performed in order to move the vortex elements by:

$$(\Delta x, \Delta y, \Delta z)_l = (u, v, w)_l \cdot \Delta t \quad (32)$$

This is the only difference between the two methods, because once the wake geometry is defined, the calculation of influence matrices and thus, the solution of the problem at the next time step are established in an identical manner. The modelling of the wake is completed and so it is possible to evaluate the contribution of each wake ring r -th to the local velocity in the k -th control point and store it in the \mathbf{A}_w matrix of wake influence coefficients, where

$$\mathbf{A}_{w_{kr}} = \mathbf{V}_{\text{WI}_{kr}} \cdot \mathbf{n}_k \quad (33)$$

with $\mathbf{V}_{\text{WI}_{kr}}$ being the wake-induced velocity from wake ring r at the collocation point k .

Before further proceeding with the description of the model, it is worth to highlight a few important aspects concerning the roll-up modelling. The use of discrete vortex segments to account for the vorticity in the shed wake originates accuracy issues due to the singularity that arises from a straight application of the Biot-Savart law when the induced point is located very close to the vortex line, leading to nonphysical values of the local velocity assigned to it. This usually occurs when a wake encounters another body or when the wake has an intense roll-up causing self-intersections. Aeroelastic response of a highly deformable wing seems to emphasize this aspect, since the trailing edge of the body changes position with time and so the position where the wake is shed, calling for a more complicated roll-up of the wake compared to the pure aerodynamic case. To prevent this kind of numerical problems and lack of accuracy, many techniques have been introduced, as for example the vortex-core model. The basic idea, as shown in [63], is that the formation of the wake behind any lifting surface must be considered as a viscous phenomenon, with the vorticity contained in the vortex core diffused radially outward with time. This observation is corroborated, for example, by experimental measurements of the distribution of tangential velocity surrounding a tip vortex shed from a blade at various wake ages [64]. According to a potential theory, this region is infinitesimal because all the vorticity is concentrated along the axis of each vortex filament and this leads to singularity in the evaluation of the Biot-Savart law near the vortex. In a more realistic model, this line should have an inner part, that is a finite core, where the flow rotates almost as a rigid body, whereas in the outer part behaves almost as a potential flow. With this line of reasoning, it is possible to define the core radius r_c both as the radial location where the tangential speed induced by the vortex has a maximum and as the boundary from the inner rotational flow field and the outer potential flow. Now that the physical meaning of the sought de-singularization of the induction estimate is pointed out, a revisited version of the Biot-Savart law is presented:

$$\mathbf{V} = \frac{\Gamma}{4\pi} \frac{h}{(r_c^{2n} + h^{2n})^{\frac{1}{n}}} (\cos\theta_1 - \cos\theta_2) \cdot \mathbf{e} \quad (34)$$

where the reader is referred to [64] for the notation and a plausible choice of the size of core radius.

The other important aspect is related to the issue of reducing as much as possible the time needed to evaluate at each timestep the influence of the *far* vortex rings. With this aim, thanks to the equivalence between vortex ring and doublet panels [65], application of the far field formulas of point-doublet may be employed [62].

Another option to reduce the computational costs is the truncation of the wake domain: a threshold is defined so that beyond that distance the contribution of the wake on the local velocity on the control points over the body is assumed negligible. As a consequence, the *far wake panels* could be neglected. This wake truncation is thought to be sufficiently reliable because there is only interest in the wake influence over the body.

4. Boundary Condition

In order to be able to write the wall tangency condition, which states the *no normal velocity* condition on the control points over the body, all the contributions have to be taken into account: the velocity induced by the body rings \mathbf{V}_{SI} , and wake rings \mathbf{V}_{WI} , the kinematic velocity \mathbf{V}_{KIN} , which is the velocity of wind on the surface (in particular it is of interest the one at the collocation points) due to relative motion of the wing, as viewed in the body frame of reference. This last contribution depends on the free-stream velocity, the rigid motion of the body but also on the elastic deformation of the body \mathbf{V}_{rel} (this is relevant in aeroelastic problems). The terms \mathbf{V}_{WI} and \mathbf{V}_{KIN} contribute to the right hand side, whereas \mathbf{V}_{SI} is unknown (byproduct of the multiplication of matrix \mathbf{A} of eq.(31) with the unknown intensity of the body vortex rings). Thus, it is possible to write in a matrix form the following system

$$\mathbf{A} \cdot \mathbf{\Gamma} = \mathbf{RHS} \quad (35)$$

where $\mathbf{\Gamma}$ is the array containing the unknowns (strength of the vortex rings), and

$$\mathbf{RHS}_k = -(\mathbf{V}_{WI_k} + \mathbf{V}_{KIN_k}) \cdot \mathbf{n}_k \quad (36)$$

is the vector containing the known part of the normal velocity components.

5. Evaluation of Loads

Once solved the linear set of equations, next step is the evaluation of the pressure over each body panel and subsequently the applied loads. The Bernoulli equation for incompressible and irrotational flow with the hypothesis of negligible body forces states that the sum of the left-hand side terms of eq.(37) are a function of time only

$$\frac{p}{\rho} + \frac{v^2}{2} + \frac{\partial\phi}{\partial t} = C(t) \quad (37)$$

where p is the pressure, ρ is the density, v is the local fluid velocity and ϕ its potential. Evaluating the left-hand side of eq.(37) in two points of the fluid, an arbitrary point and a reference point at infinity (where $\phi = 0$ and $\mathbf{v} = \mathbf{0}$ having chosen the wind reference system), eq.(38) is obtained:

$$\frac{p_\infty - p}{\rho} = \frac{v^2}{2} + \frac{\partial\phi}{\partial t} \quad (38)$$

It is then possible to integrate the pressure and, with aid of Kutta-Joukowski theorem, assess the lift produced by each panel.

D. Interface Algorithms

1. Infinite Plate Splines

THEORY The Infinite Plate Spline concept was introduced in reference [24] and is the basis of several of the interpolation schemes used in today's commercial software. This method is based on a superposition of the solutions of the equilibrium equation describing an infinite plate subjected to small deflections. The key idea is to consider a set of discrete points (x_i, y_i) lying within a two-dimensional domain, each of them has associated a deflection w_i that defines the *vertical* position of the surface on which both structural and aerodynamic points are presumed to be. Using a superposition of solutions it is possible to calculate the values of a set of *fictitious* concentrated loads acting at the known set of points that give rise to the required deflection w . In this way, given the deflections of the structural grid points the concentrated forces are obtained and it is possible, by an interpolation process, to calculate the values on a set of aerodynamic grid points. The interpolated function is differentiable everywhere.

The main drawback of the method is that it is inherently 2-D and so it is limited to interpolate out-of-plane displacement only. Moreover, a piecewise flat planform for the wing has to be assumed, also when the wing is deformed. In the following, the entire mathematical procedure to gain the desired results is omitted and just the major features are outlined; for details about the derivation of the scheme the reader is referred to reference [66].

The governing equation for a plate (bending case) that extends to infinity in both directions is:

$$D_{11} \frac{\partial^4 w}{\partial x^4} + 2(D_{12} + 2D_{66}) \frac{\partial^4 w}{\partial x^2 \partial y^2} + D_{22} \frac{\partial^4 w}{\partial y^4} = p \quad (39)$$

where p is the applied pressure. Then, a series of hypotheses are considered. First, the material is assumed to be isotropic, giving this a specific value for the D_{11} , D_{12} , D_{22} , D_{66} stiffness terms. Then, radial symmetry is imposed, and a concentrated load is applied at the origin. After that, with the argument that no singular displacement is acceptable at the origin, some terms in the closed form of the solution w are set to zero. Final adjustments are done to avoid oscillations. With all these hypotheses, the final form for the vertical displacement w is:

$$w(x, y) = a_0 + a_1 x + a_2 y + \sum_{i=1}^{\tilde{N}} \tilde{F}_i r_i^2 \ln r_i^2 \quad (40)$$

with:

$$\begin{aligned}
a_0 &= \sum_{i=1}^{\tilde{N}} [A_i + B_i (x_i^2 + y_i^2)] \\
a_1 &= -2 \sum_{i=1}^{\tilde{N}} B_i x_i \\
a_2 &= -2 \sum_{i=1}^{\tilde{N}} B_i y_i
\end{aligned} \tag{41}$$

where \tilde{N} is the number of fictitious loads (or alternatively, the number of known value w_i), A_i , B_i and r_i are known quantities and \tilde{F}_i are the fictitious concentrated loads used to reconstruct the shape of the plate, given the actual position of the set of known points.

APPLICATION TO THE DISPLACEMENT AND LOAD TRANSFER The goal of this interface algorithm is to provide both a relation between structural and aerodynamic mesh displacements and to aerodynamic and structural loads. In other word, it consists in two phases: given a displacement vector \mathbf{U} (and also its derivatives), representing the unknowns associated with the structural nodes, it extrapolates the displacement at the aerodynamic mesh points, so that the aerodynamic forces, may be evaluated by the aerodynamic solver; given the aerodynamic forces, it projects them to the structural nodes, so that the computational mechanics capability can calculate the structural displacements. The way these phases are arranged depends on the way the aeroelastic coupling is performed. In the present effort, the goal is to get an explicit expression of the aerodynamic loads applied at the structural nodes, given a structural deformation \mathbf{U} .

Before further proceeding, the interface algorithm is specialized. The reference planes where the splines are specified are planar, and have the local x -axis (x^S) along the (initial) free-stream direction. The local vertical displacements (which are then perpendicular to the spline plane but not necessarily coincident with the vertical displacement in the global coordinates z) are denoted with Z^S and \mathcal{Z}^S for the generic structural node and aerodynamic control point, respectively.

Eq.(40) shows how IPS are employed to evaluate the z^S coordinate of a generic point of the system once both its position through the local coordinates x^S and y^S and the required coefficients are given. The expression of the aerodynamic loads is calculated starting from the boundary condition applied on the *control points* and the involved quantities are thus related to the derivative of the vertical displacement with respect to the x^S direction $\frac{d\mathcal{Z}^S}{dx^S}$ (which, as it will be shown in the following is related to the changes of relative angle of attack), the speed $\dot{\mathcal{Z}}^S$ and the acceleration $\ddot{\mathcal{Z}}^S$ of this set of points, so that the sought algorithm should provide relations between them and the degrees of freedom in the structural nodes. Eq.(40) can be advantageously applied to the structural points in matricial form, it can be written as

$$\mathbf{Z}^S = \mathbf{G} \tilde{\mathbf{F}} \tag{42}$$

Inverting this expression, the unknown array $\tilde{\mathbf{F}}$ containing the fictitious concentrated loads is obtained; now the coefficients that have to be used for the spline interpolation (see eq.(41)) are known.

In order to avoid the time consuming task of obtaining the vector $\tilde{\mathbf{F}}$ at each timestep, the assumption that during the deformation process the original local coordinates x_i^S and y_i^S of the generical point i do not change is made, i.e. the vertical projection is always corresponding (or at least in good approximation) to the initial position of the structural point considered. If this hypothesis is not satisfied, \mathbf{G} changes during the simulation and has to be continuously evaluated.

Carrying on the interpolation for the desired variables, the following relations are obtained

$$\begin{aligned}
\dot{\mathcal{Z}}^S &= \mathbf{H} \dot{\mathbf{Z}}^S \\
\ddot{\mathcal{Z}}^S &= \mathbf{H} \ddot{\mathbf{Z}}^S \\
\frac{d\mathcal{Z}^S}{dx^S} &= \mathbf{H}^D \mathbf{Z}^S
\end{aligned} \tag{43}$$

where \mathbf{H} easily derives from eq.(42) now applied to the vertical displacement field \mathbf{Z}^S of the aerodynamic mesh (the constant expression of the spline's matrices allows one to use them to interpolate also the time

derivatives); \mathbf{H}^D is the interface matrix for the spatial derivative of the displacement and can be gained differentiating eq.(41) with respect to the local x direction and specializing it for the control points.

The last task to be performed to complete the interfacing for the aerodynamic-structural coupling originates from the following issue: for a correct application of the Kutta-Joukowski theorem, the aerodynamic loads have to be applied in the load points of the vortex ring. In order to use a FEM structural solver, the loads are thought to act on the structural nodes and thus, given an external concentrated load, its transferring to the FE nodes of the triangle shell element has to be performed. The problem, depicted in Fig. 2 can be tackled with an energy conserving approach imposing that the virtual work done by the external force is equal to the virtual work done by the nodal forces of the element. The expression of the forces acting on the

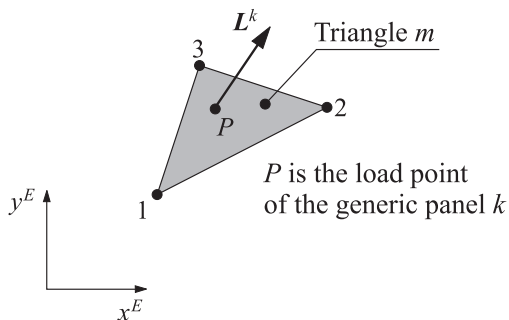


Fig. 2. Applied load in a triangular element

three vertices of the triangle equivalent to the aerodynamical load applied in the point P with coordinates (x^E, y^E) is given by

$$\begin{aligned} \mathbf{L}_1^m &= h_1^m(x_P^E, y_P^E) \mathbf{L}^k \\ \mathbf{L}_2^m &= h_2^m(x_P^E, y_P^E) \mathbf{L}^k \\ \mathbf{L}_3^m &= h_3^m(x_P^E, y_P^E) \mathbf{L}^k \end{aligned} \quad (44)$$

where the shape functions relative to the nodes 1, 2 and 3 of the triangle m are indicated respectively as $h_1^m(x^E, y^E)$, $h_2^m(x^E, y^E)$ and $h_3^m(x^E, y^E)$ and can be evaluated making use of the area coordinates [67].

2. Interface with Moving Least Square derived algorithm

The present interface algorithm has the purpose to solve the typical aeroelastic problem of coupling the aerodynamic and structural meshes granting important features [68]. It is in fact possible to interface both non-matching surfaces or non-matching topologies. Cases in which a control point falls outside the range of the source mesh are also naturally tackled. There is also a relative insensitiveness to the node density variations in the source mesh. A very important feature is the conservation of exchanged quantities, in particular momentum and energy: this is a keypoint since in literature [69] it has been shown how nonconservative interfaces may lead to wrong results. In spite of these valuable advantages, the computational efficiency of interface computation is really high. A further very desirable feature is the relative independence from the numerical formulation of the solvers of the two fields.

PROBLEM STATEMENT Thanks to *meshless* approach it is possible to achieve the previously listed goals. Traditionally, meshless methods were introduced as a method of numerical resolution of partial differential equations different than finite element method (FEM), finite difference method (FDM) and finite volume method (FVM). In these last approaches, spatial domain is often discretized into meshes: the set of differential equations are approximated by a set of algebraic equations for each mesh and then, by assembling in the proper way the contribution of all of them, the final system of algebraic equations for the whole problem is obtained. On the contrary, in mesh free method [25], this system of algebraic equations for the whole problem is obtained using a set of nodes scattered in the domain which do not form a mesh because no information on the relationship between the nodes (e.g., connectivity of an element) is required.

These methods seem to solve some issues of the classical approaches which are here briefly listed. First, the creation of an adequately discretized mesh is notoriously a bottleneck in the process since it is both

manpower and computer time consuming. Second, the classical approaches have a limited regularity of the solution, especially in its derivatives, at the elements' boundaries (although approaches using higher order continuous basis function like *NURBS* were already proposed in [70]). Moreover, with lagrangian grids/meshes there is a lost of accuracy when large deformations are investigated because of the element distortions. A close examination of these difficulties shows that the root of the problem is the necessity to use elements (mesh); on the contrary a meshless method does not have these limitations, and could add or delete nodes when they are needed, providing a great flexibility to the analysis.

In the present effort what is adopted from the meshless method is one of its central features: the shape functions. A number of ways to construct shape functions have been proposed in literature, here the choice falls on Moving Least Square approximation (MLS), which belongs to the family of finite series representation methods. This family of shape functions were originally introduced for data fitting and surface reconstruction [71], while in [72] they were used for the first time to build shape functions for the Diffuse Element Method (DEM), which was among the first ones properly called mesh free method and had a strong impact on the field. The two main features of MSL are the continuity and smoothness in the entire problem domain of the approximated field function, and the ability to produce the desired order of consistency (a method is said to have k -th order consistency if can reproduce polynomials of up to the k -th order). The procedure of constructing shape functions using MLS approximation is fully presented in appendix A, while in this section just the main features are outlined.

MOVING LEAST SQUARE The basic idea is to compute the value of a function $u(\mathbf{x})$ on a set of nodes $\{\boldsymbol{\eta}_1, \boldsymbol{\eta}_2, \dots, \boldsymbol{\eta}_{\hat{N}}\}$ from its values $\hat{u}(\boldsymbol{\xi}_1), \hat{u}(\boldsymbol{\xi}_2), \dots, \hat{u}(\boldsymbol{\xi}_{\hat{n}})$ on scattered centers (or sources) $\{\boldsymbol{\xi}_1, \boldsymbol{\xi}_2, \dots, \boldsymbol{\xi}_{\hat{n}}\}$ without deriving an analytical expression. This extrapolation is denoted \hat{u}^h and is built as a sum of \hat{m} basis functions $\hat{p}_i(\boldsymbol{\eta})$

$$\hat{u}^h(\boldsymbol{\eta}) = \sum_{i=1}^{\hat{m}} \hat{p}_i(\boldsymbol{\eta}) a_i^{\boldsymbol{\xi}}(\boldsymbol{\eta}) = \hat{\mathbf{p}}(\boldsymbol{\eta}) \cdot \mathbf{a}^{\boldsymbol{\xi}}(\boldsymbol{\eta}) \quad (45)$$

where $a_i^{\boldsymbol{\xi}}$ are the unknown coefficients of the basis functions which depend on the point $\boldsymbol{\eta}$ where the value is sought and on the set of scattered centers $\boldsymbol{\xi}$ where the function is known (this dependence, denoted by the superscript in eq.(45), will be omitted in the following for clearness). The array $\hat{\mathbf{p}}$ of basis functions consists often of monomials of the lowest order such to form polynomial basis with minimum completeness but particular functions can be added to reproduce a particular behaviour of the investigated variables.

In the present study linear and quadratic polynomials are adopted. The neighbourhood of the point $\boldsymbol{\eta}$, its *support domain*, is given by a subset of $\boldsymbol{\xi}$, namely $\boldsymbol{\xi}^s$, made of \hat{n}_s nodes which are the only ones used locally to approximate the field function. Each node $\boldsymbol{\eta}$ has a different set $\boldsymbol{\xi}_s$ with in general a different number of nodes \hat{n}_s , that is $\hat{n}_s = \hat{n}_s(\boldsymbol{\eta})$. The \hat{m} coefficients a_i describing (as shown in eq.(45)) the function in the point $\boldsymbol{\eta}$ are obtained minimizing the functional weighted residual (a weighted discrete L_2 norm) $J(\boldsymbol{\eta})$:

$$J(\boldsymbol{\eta}) = \sum_{i=1}^{\hat{n}} W(\boldsymbol{\eta} - \boldsymbol{\xi}_i) [\tilde{u}(\boldsymbol{\xi}_i, \boldsymbol{\eta}) - \hat{u}(\boldsymbol{\xi}_i)]^2 \quad (46)$$

where

$$\tilde{u}(\boldsymbol{\xi}_i, \boldsymbol{\eta}) = \hat{\mathbf{p}}(\boldsymbol{\xi}_i) \cdot \mathbf{a}(\boldsymbol{\eta}) \quad (47)$$

is the approximated value of the the field function in the generical center of the set $\boldsymbol{\xi}$ obtained by means of the same extrapolation process pointed out in eq.(45). The weight function W used in eq.(46) is positive for all the $\boldsymbol{\xi}_i$ centers in the support of node $\boldsymbol{\eta}$ and zero outside, and has two important roles in constructing the MLS shape functions: it provides weighting for the residual at different nodes in the support domain (small weights are wanted for centers far from $\boldsymbol{\eta}$); it ensures a smooth manner for centers to leave and enter the support domain of the considered node. Here comes out the important difference with the FEM shape functions, which are obtained minimizing the residual J in eq.(46) assuming a unitary constant weight function and repeating this operation element by element (which coincides with the support domain of the nodes). By replacing the discontinuous weights of FEM approach with continuous weighting functions evaluated in the centers of the nodes the smoothness of the approximate function is granted. Solving the minimization problem

$$\frac{\partial J(\boldsymbol{\eta})}{\partial \mathbf{a}} = 0 \quad (48)$$

an expression for the coefficient vector $\mathbf{a}(\boldsymbol{\eta})$ is obtained, allowing to rewrite eq.(45)

$$\hat{u}^h(\boldsymbol{\eta}) = \boldsymbol{\Phi}(\boldsymbol{\eta}) \cdot \hat{\mathbf{u}} \quad (49)$$

where $\boldsymbol{\Phi}(\boldsymbol{\eta})$ is the array containing the coefficients of the MLS shape function corresponding to the node $\boldsymbol{\eta}$, while $\hat{\mathbf{u}}$ has the value of the field function on the centers. For more details on the derivation refer to appendix A.

It can be observed that the shape functions in eq.(49) do not satisfy the Kronecker delta criterion $\Phi_i(\boldsymbol{\xi}_j) = \delta_{ij}$ resulting in $\hat{u}^h(\boldsymbol{\xi}_i) \neq \hat{u}(\boldsymbol{\xi}_i)$, that is, the nodal parameters $\hat{u}(\boldsymbol{\xi}_i)$ are not coincident with the nodal values $\hat{u}^h(\boldsymbol{\xi}_i)$; this means that they are not interpolants, but rather approximates of a function; this property can represent a drawback when the imposition of essential boundary conditions is requested, but it is possible to overcome it as shown in appendix A.

As stated, the MLS approximation is able to reproduce the desired order of consistency, depending on the complete order of the monomial basis $\hat{\mathbf{p}}$: if the complete order of the base is k , it can be demonstrated that the shape function will possess k consistency.

The calculation of spatial derivatives of the function \hat{u} , requires to derive eq.(45), that is:

$$\frac{\partial u}{\partial x} \simeq \frac{\partial u^h}{\partial x} = \frac{\partial \hat{\mathbf{p}}}{\partial x} \cdot \mathbf{a} + \hat{\mathbf{p}} \cdot \frac{\partial \mathbf{a}}{\partial x} \quad (50)$$

The second term of eq.(50) is not trivial to evaluate and a straight procedure is showed in [25]; it is not an expensive task itself, however it requires the knowledge of the cloud of particles surrounding each point $\boldsymbol{\eta}$ and, thus, it depends on the point where the information is evaluated; on the contrary, the first term can be evaluated *a priori*. Work [72] proposed the concept of diffusive derivative, which consists in approximating the derivative only with the first term on the right hand side of eq.(50), and it proved convergence at optimal rate.

The great advantage of the problem expressed in this form is the possibility to preserve the local character of the MLS approximation choosing a compact support weight function W , that is supposed to satisfy the following requirements:

- W is a monotonically decreasing function that depends only on a scalar parameter r that represents the Euclidean distance from the two considered points;
- W has a compact support, so

$$\begin{cases} W(r) > 0 & \text{if } r < \bar{r} \\ W(r) = 0 & \text{if } r > \bar{r} \end{cases} \quad (51)$$

- W enjoys normal property such that

$$\int_{\Omega} W(\boldsymbol{\eta} - \mathbf{x}) d\Omega = 1 \quad (52)$$

where \bar{r} is the radius delimiting Ω , the local support of node $\boldsymbol{\eta}$.

Examples of functions that satisfy these requirements are the Radial Basis Function (RBF) family, which can be found in different forms as Multiquadratics, Gaussian, Thin Plate Spline and Logarithmic. In this study the adopted functions possess the lowest possible degree among all piecewise polynomial compactly supported radial functions of a given order of smoothness [73]: this is an important property since the approximate functions are as smooth as the involved weight function.

After the dimension of the local support is chosen, the last operation of the preliminary phase is the determination of the centers which belong to each node $\boldsymbol{\eta}$; several strategies exist to solve this task and a suitable choice from the computational point of view is to rely on *nearest neighbor searching algorithms* [74]: given a set S of n data points in a metric space X in real d -dimensional space, the idea is to preprocess these points so that, given any query point $q \in X$, the k nearest points to q can be efficiently reported. These algorithms perform the geometric preprocessing of building the structure at $O(d)$ cost and the subsequent operation to get the nearest neighbor from the data set with an $O(k \cdot \log d)$ cost.

As previously stated, an important property sought in the present interface algorithm is the conservation of momentum and energy; using eq.(49) to exchange the information of displacement and velocity from the structure to the aerodynamic field, conservation (although not in a strictly mathematical sense) is achieved because a minimization process is performed and so a limited amount of information can be transmitted [68]. While the conservation of momentum transmitted is taken in account with the definition of the Φ interface matrix, other considerations lead to conservation of energy. As demonstrated in appendix A, to ensure the balance of the energy exchanged between fluid and structure, the loads on the structural nodes \mathbf{f}_i have to be evaluated by multiplying the loads \mathbf{F}_i on the aerodynamic grid by the transpose of the interpolation matrix \mathbf{H} (same as Φ of eq.(49)) that matches the two displacement fields.

E. Aeroelastic Coupling

In this section the goal is to express the aerodynamic loads so that they can be combined with the dynamic model presented in section B in order to formulate the aeroelastic problem.

1. Boundary Condition

The starting point to obtain the sought expression is the boundary condition (enforced at the control points). Recalling the matrix formulation from eq.(35), it is worth to highlight the various contributions to the **RHS** vector. The *first* contribution can be written as

$$\mathbf{RHS}_1 = -\mathbf{A}_w \cdot \mathbf{\Gamma}_w \quad (53)$$

where \mathbf{A}_w is the wake influence coefficients matrix and $\mathbf{\Gamma}_w$ is the vector with the strength of the wake singularities, both completely defined from the previous time steps calculations.

The *second* term is the free-stream contribution

$$\mathbf{RHS}_2 = -\mathbf{V}_\infty^n \quad (54)$$

where \mathbf{V}_∞^n is the component of the free-stream velocity along the normal to the ring. In order to evaluate this term, it is useful to consider Fig. 3, in which the k -th body ring as well as the position of the control point and a sketch of both the deformed and undeformed configurations are depicted. Unit vector \mathbf{i} is parallel

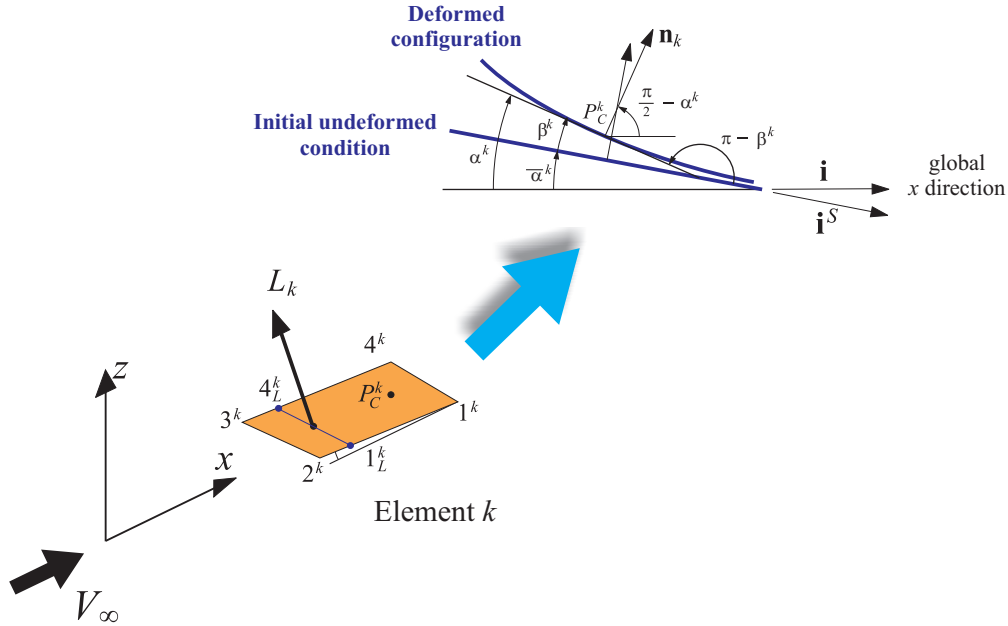


Fig. 3. Geometry and local normal of the body ring

to the free stream, while \mathbf{i}^S is the direction of the free stream projected to the undeformed ring plane. By

definition, the k -th element of \mathbf{V}_∞^n is given by $V_\infty \mathbf{i} \cdot \mathbf{n}_k$, where \mathbf{n}_k is the normal to the ring in its *actual* configuration, and the following holds:

$$\mathbf{i} \cdot \mathbf{n}_k = \cos\left(\frac{\pi}{2} - \alpha^k\right) = \sin \alpha^k = \sin(\bar{\alpha}^k + \beta^k) = \sin \bar{\alpha}^k \cos \beta^k + \cos \bar{\alpha}^k \sin \beta^k \quad (55)$$

being $\bar{\alpha}^k$ the angle of attack of ring k in the undeformed configuration and the angles α^k and β^k the ones reported in Fig. 3. Under the assumption of small angles:

$$\begin{aligned} \cos \bar{\alpha}^k &\approx 1 \\ \cos \beta^k &\approx 1 \\ \sin \beta^k &\approx \tan \beta^k = -\tan(\pi - \beta^k) \end{aligned} \quad (56)$$

A synthetic expression of eq.(55) can be given, discerning the different meanings of the involved terms:

$$V_\infty \mathbf{i} \cdot \mathbf{n}_k = V_{\infty,0}^{n_k} + V_{\infty,d}^{n_k} \quad (57)$$

where $V_{\infty,0}^{n_k} = V_\infty \sin \bar{\alpha}^k$ is the k -th element of $\mathbf{V}_{\infty,0}^n$, and is related to just the change in the rigid angle of attack (*rigid aoa*); it is thus a function of the time only. The second term $V_{\infty,d}^{n_k}$ is the contribution of the free stream due to the deformation of the wing (*elastic aoa*) and is a function of the deformed shape. Observing that $\tan \beta^k$ is equal to the opposite of the derivative of the displacement of the control point in the direction of the *undeformed* normal in respect to the direction \mathbf{i}^S (*undeformed x* direction), it can be written:

$$V_{\infty,d}^{n_k} = -V_\infty \frac{d\hat{Z}_k}{dx_k^S} \quad (58)$$

where the vector $\hat{\mathbf{Z}}$ collects the displacements of the control points along the undeformed aerodynamic rings' normals. This contribution can be directly related to the slope of the normal component of displacement of the control point k .

The third term depends on the strain rate of the structure: it originates from the relative body-flow velocity that is established as the body changes its shape, giving a contribution to the effective flow speed that has to be taken into account for a correct evaluation of eq.(35). This is an important source of aerodynamic damping. It holds:

$$\mathbf{RHS}_3 = \dot{\hat{\mathbf{Z}}} \quad (59)$$

The generic $\dot{\hat{\mathbf{Z}}}$ can be evaluated extrapolating the deformation velocity on the control points from the vector $\dot{\mathbf{U}}$, which contains the generalized velocity of the structural nodes, and multiplying it by the normal to the k -th ring \mathbf{n}_k , in its *actual* configuration.

Now that all the RHS terms have been conveniently treated, eq.(35) can be re-written as:

$$\begin{aligned} \mathbf{A} \cdot \boldsymbol{\Gamma} &= \mathbf{RHS}_1 + \mathbf{RHS}_2 + \mathbf{RHS}_3 \\ &= -\mathbf{A}_w \cdot \boldsymbol{\Gamma}_w - \mathbf{V}_{\infty}^n + \dot{\hat{\mathbf{Z}}} \end{aligned} \quad (60)$$

and inverting \mathbf{A} , this final form is obtained:

$$\boldsymbol{\Gamma} = \boldsymbol{\Gamma}_1 + \boldsymbol{\Gamma}_2 \cdot \mathbf{U} + \boldsymbol{\Gamma}_3 \cdot \dot{\mathbf{U}} \quad (61)$$

$\boldsymbol{\Gamma}_1$ is the known contribution due to the wake and to the *rigid aoa*, i.e., the first term in eq.(57)

$$\boldsymbol{\Gamma}_1 = -\mathbf{A}^{-1} \mathbf{A}_w \cdot \boldsymbol{\Gamma}_w - \mathbf{A}^{-1} \mathbf{V}_{\infty}^n \quad (62)$$

$\boldsymbol{\Gamma}_2$ is the matrix that multiplies the displacement field \mathbf{U} ; it features a matrix performing the interpolation between the aerodynamic and structural meshes in order to get the derivative in respect to x^S (\mathbf{H}_{dx}) of the displacement. This matrix is multiplied by the matrix (\mathbf{N}_0) in order to sample correctly just the component parallel to the *undeformed* normal of the ring:

$$\boldsymbol{\Gamma}_2 = -V_\infty \mathbf{A}^{-1} \mathbf{N}_0 \mathbf{H}_{dx} \quad (63)$$

$\boldsymbol{\Gamma}_3$ multiplies the given velocity field $\dot{\mathbf{U}}$. The matrix (\mathbf{H}_{disp}) performs the interpolation between the two meshes, and is multiplied by (\mathbf{N}_d) in order to sample correctly just the component parallel to the *actual* normal of the ring.

$$\boldsymbol{\Gamma}_3 = \mathbf{A}^{-1} \mathbf{N}_d \mathbf{H}_{disp} \quad (64)$$

2. Aeroelastic Loads

Starting from the Bernoulli equation for an incompressible, irrotational and unsteady flow, and following reference [62] it is possible to evaluate the aerodynamic actions. These relations can be advantageously expressed in matrix form as

$$\mathbf{p} = \rho \mathbf{\Delta} \cdot \mathbf{\Gamma} + \rho \frac{\partial \mathbf{\Gamma}}{\partial t} \quad (65)$$

where p is the array containing the difference between upper and lower pressure for each panel, $\mathbf{\Delta}$ is the matrix that, for each ring of the body, applies the finite difference derivative scheme to $\mathbf{\Gamma}$ and multiplies it with the suitable coefficients. To finally obtain the expression of the lift acting on the load points of the aerodynamic mesh, the direction \mathbf{r}_L^k of the force over the k -th ring is chosen accordingly to the Kutta-Joukowski theorem as:

$$\mathbf{r}_L^k = \mathbf{i} \times \mathbf{r}_{4_L^k - 1_L^k} \quad (66)$$

where $\mathbf{r}_{4_L^k - 1_L^k}$ connects the projections of the load point P_L^k along the segments $3^k - 4^k$ and $2^k - 1^k$ (as depicted in Fig. 4) and has a modulus equal to the width of the ring panel. Calling c_k the chord of the ring

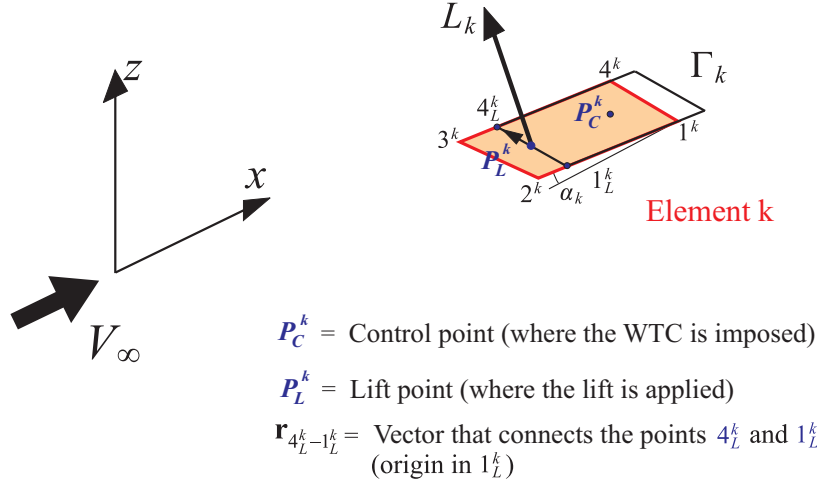


Fig. 4. Direction of the lift over the ring k

and $(\mathbf{i}, \mathbf{j}, \mathbf{k})$ the axes direction in the global coordinate system, it is finally possible to give a general expression of the three components of the lift force acting on the k^{th} ring:

$$\begin{aligned} L_x^k &= c_k \mathbf{i} \cdot \mathbf{r}_{4_L^k - 1_L^k} p_k \\ L_y^k &= c_k \mathbf{j} \cdot \mathbf{r}_{4_L^k - 1_L^k} p_k \\ L_z^k &= c_k \mathbf{k} \cdot \mathbf{r}_{4_L^k - 1_L^k} p_k \end{aligned} \quad (67)$$

which in matrix form becomes:

$$\mathbf{L} = \mathbf{S} \mathbf{p} \quad (68)$$

If N is the number of body rings, \mathbf{S} is a $3N \times N$ matrix such that when multiplied by \mathbf{p} gives rise to the vector \mathbf{L} , whose dimensions are $3N \times 1$, and is assembled repeating the pattern of eq.(67) for each element k .

As it can be seen from eq.(65), the unsteady part of the pressure depends on the derivative of $\mathbf{\Gamma}$ with respect to time. The derivation can be carried out using eq.(61), leading to

$$\frac{\partial \mathbf{\Gamma}}{\partial t} = \frac{\partial \mathbf{\Gamma}_1}{\partial t} + \mathbf{\Gamma}_2 \cdot \dot{\mathbf{U}} + \mathbf{\Gamma}_3 \cdot \ddot{\mathbf{U}} \quad (69)$$

where the derivatives of $\mathbf{\Gamma}_2$ and $\mathbf{\Gamma}_3$ are considered negligible. Now eq.(65) combined with eqs.(61) and (69) lead to the sought expression for the aerodynamic loads

$$\mathbf{L}^{\text{LP}} = \mathbf{L}_1^{\text{LP}} + \mathbf{L}_2^{\text{LP}} \cdot \mathbf{U} + \mathbf{L}_3^{\text{LP}} \cdot \dot{\mathbf{U}} + \mathbf{L}_4^{\text{LP}} \cdot \ddot{\mathbf{U}} \quad (70)$$

with

$$\begin{aligned}
\mathbf{L}_1^{\text{LP}} &= \rho \mathbf{S} \cdot \Delta \cdot \Gamma_1 + \rho \mathbf{S} \cdot \frac{\partial \Gamma_1}{\partial t} \\
\mathbf{L}_2^{\text{LP}} &= \rho \mathbf{S} \cdot \Delta \cdot \Gamma_2 \\
\mathbf{L}_3^{\text{LP}} &= \rho \mathbf{S} \cdot \Delta \cdot \Gamma_3 + \rho \mathbf{S} \cdot \Gamma_2 \\
\mathbf{L}_4^{\text{LP}} &= \rho \mathbf{S} \cdot \Gamma_3
\end{aligned} \tag{71}$$

The superscript LP is used to outline how these are forces applied on the load points of the ring. As for the matrices \mathbf{H}_{dx} and \mathbf{H}_{disp} , the interface algorithm will provide the way to transfer these quantities on the structural nodes.

3. Residual and Tangent Matrix Expression

It is assumed that the aerodynamic forces have been projected to the nodes of the structural solver through one of the load transferring techniques: the previously defined \mathbf{L}_1^{LP} , \mathbf{L}_2^{LP} , \mathbf{L}_3^{LP} and \mathbf{L}_4^{LP} are now named as \mathbf{L}_1^S , \mathbf{L}_2^S , \mathbf{L}_3^S and \mathbf{L}_4^S because they are quantities related to the structural nodes. Recalling section B, there were different options for the time integration, leading to different options for the evaluation of the aerodynamic contribution, namely eqs.(15) and (11). With the expression outlined in eq.(71), and recalling that \mathbf{s} was expressing the generalized structural coordinates whereas \mathbf{U} represents the displacement from an initial reference configuration, it is then immediately possible to give the appropriate value of the aerodynamic loads in the expression of the residual.

Also the derivation of the aerodynamic tangent matrix is trivial. With reference to eq.(21)

$$\frac{d}{d} \frac{t+\Delta t}{\mathbf{s}} \mathbf{L}^S = \frac{\partial}{\partial} \frac{t+\Delta t}{\mathbf{s}} \mathbf{L}^S + \frac{\partial}{\partial} \frac{t+\Delta t}{\dot{\mathbf{s}}} \mathbf{L}^S \frac{\partial}{\partial} \frac{t+\Delta t}{\mathbf{s}} \dot{\mathbf{s}} + \frac{\partial}{\partial} \frac{t+\Delta t}{\ddot{\mathbf{s}}} \mathbf{L}^S \frac{\partial}{\partial} \frac{t+\Delta t}{\mathbf{s}} \ddot{\mathbf{s}} \tag{72}$$

Recalling eqs.(5) and (70), and observing that derivatives with respect to the generalized coordinates are identical to derivatives in respect to displacements, i.e.,

$$\frac{d}{d\mathbf{s}} = \frac{d}{d\mathbf{U}} \tag{73}$$

then, it can be inferred that:

$$\frac{d}{d} \frac{t+\Delta t}{\mathbf{s}} \mathbf{L}^S = \mathbf{L}_2^S + \frac{\gamma}{\beta \Delta t} \mathbf{L}_3^S + \frac{1}{\beta \Delta t^2} \mathbf{L}_4^S \tag{74}$$

F. Aeroelastic Solvers

In the present study three solvers have been used. Each of them is characterized by using different options both on the pure aerodynamic side (but within the model of incompressible potential flow), and on the aeroelastic coupling. The three solvers, called *Solver1*, *Solver2* and *Solver3* have increasing computational cost. Their properties are graphically presented in Fig. 5. A solver based on the *doublet lattice method* (DLM) [36, 38] method is occasionally employed for comparison purposes.

1. Solver1

This model adopts the IPS as interface algorithm and, as outlined in section D.1, this implies simplified hypotheses, inherent both to the limits of the algorithm itself (as the 2D assumption) and to simplifications needed to preserve low computational costs. As a consequence in this model the aerodynamic mesh does not follow the structure, i.e., the coordinates of inducing rings and the induced control points that are employed in the evaluation of the coefficients of the matrices \mathbf{A} and \mathbf{A}_w in section C.2 and C.3 do not depend on the deformation process of the body. However, body's deformation still influences the boundary condition (and thus the aerodynamic load) with the terms \mathbf{RHS}_2 and \mathbf{RHS}_3 discussed in section E.1. Such a choice implies that a prescribed wake model is adopted, as it appears an useless computational task to consider a free-wake model shed from an aerodynamic mesh that does not occupy the real position of the body.

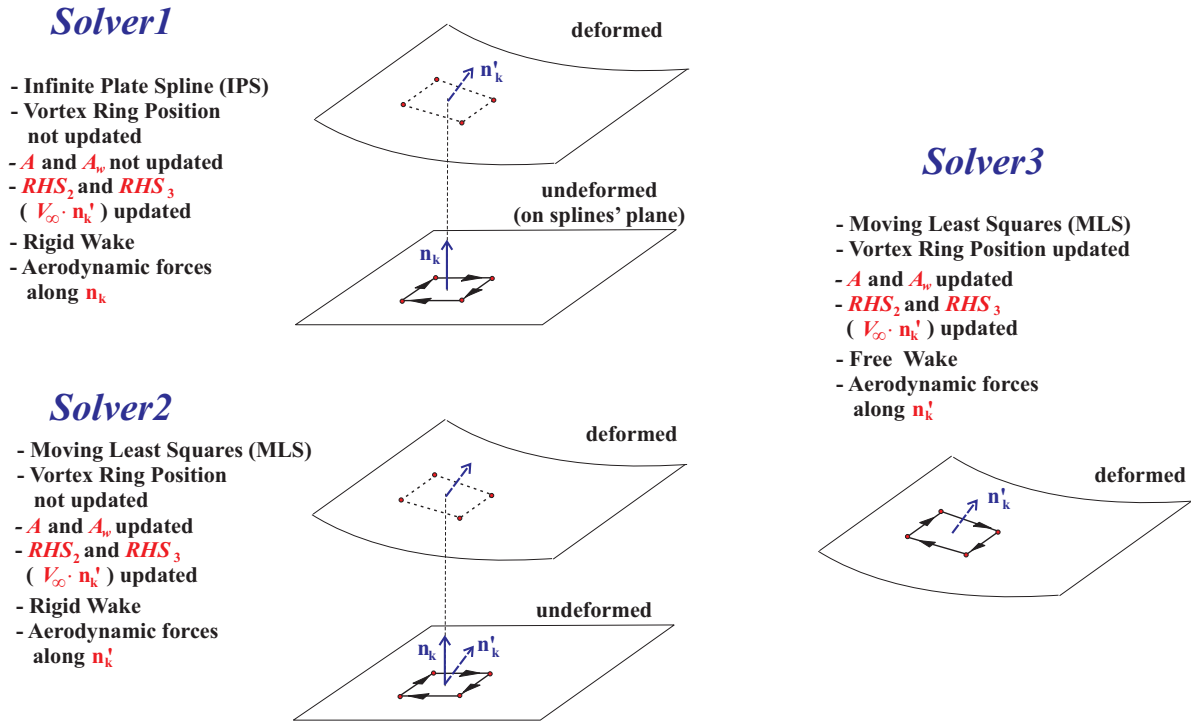


Fig. 5. Differences between the time-domain aeroelastic solvers.

2. Solver2

In *Solver2* the IPS is substituted with the MLS interpolation algorithm. Everything is linked with the coupling of aerodynamic and structural fields, which removes the obstacle of passing information between two sets of points occupying the same planar surface, as necessary with IPS. This allows to build up for each time step the real aerodynamic mesh. However, in this case a mixed approach is chosen: the *velocity vector* used for the matrices \mathbf{A} and \mathbf{A}_w is still evaluated ignoring the new position of the body, but the *aerodynamic coefficients* of these matrices (i.e. the normal components of the velocities) are updated at each timestep because in eqs.(31) and (33) it is considered the actual normal direction \mathbf{n}_k of the ring where the k -th control point is placed.

The reason of this choice is the assumption that for a correct estimate of the *velocity vector* the important aspect is the relative distance between the vortex line and the induced point and this is still in good agreement with the initial one when the body is deformed. On the contrary, what is mainly changed during the dynamic evolution, especially for very deformed configurations as the ones under investigations, is the direction along which the boundary condition should be written. Thus, there is a lack of accuracy to keep projecting the induced velocity vector on the initial normal direction.

Thanks to the MLS is possible to evaluate the updated \mathbf{r}_L^k , which gives the direction of lift produced from the k -th ring, see eq.(66). This is accomplished by means of evaluation of the actual position of the points 4_L^k and 2_L^k in Fig. 4. It is worth to notice that now the aerodynamic load is *follower both in direction and intensity*.

Since the aerodynamic mesh still remains attached to the *undeformed* configuration, free-wake approach has been not considered to be meaningful, thus, *Solver2* represents an improvement in the accuracy comparing to the *Solver1* without an excessive drawback in simulation run time.

3. Solver3

Solver3 adopts the MLS interpolation algorithm and considers the aerodynamic mesh in its actual position, enabling the free-wake model and the *correct* (without further assumptions as the ones made before) expression of all the quantities involved in the evaluation of the aerodynamic loads.

IV. Validation of the Computational Capability

Validation of the in-house computational capabilities is here demonstrated. Some components or even some full aeroelastic solvers have already been validated in previous works. For example, nonlinear structural finite element code, both in the static and dynamic versions, has been already employed in some previous efforts, i.e. [4, 11, 13, 16, 75]. Moreover, also the *DLM* capability has been already described and checked in references [37, 38]. However, some other components have been newly implemented. For example, even if the *VLM* implant was already used in the *DLM*, the new *UVLM* was not yet tested.

A. Validation of the Aerodynamic Solvers

Validation of the pure aerodynamic solvers is here demonstrated. A few words are necessary to introduce the results. Referring to section III.F, two of the several features that distinguish the aeroelastic solvers are the locations of the vortex rings and the treatment of the wake. From a pure aerodynamic perspective, then, the different modelling concerns the wake only. Thus, to validate the unsteady behaviour, the wake is treated both as rigid or deformable.

A common validation mean, popular as the *Wagner's* test case, consists in an impulsive start of an airfoil. There is an analytical expression, see [76] that describes the evolution of the lift coefficient in respect of τ , known as reduced time, which is the covered distance expressed in semi-chords of the airfoil, i.e., $\tau = 2V_\infty t/c$. Here t represents the time and c the chord of the airfoil. If C_L is the lift coefficient, it holds that $C_L(\tau) = C_L(\infty)\Psi(\tau)$, where:

$$\Psi(\tau) = 1 - 0.165 e^{-0.0455\tau} - 0.335 e^{-0.3\tau} \quad (75)$$

Since this test case is a bi-dimensional one, to validate the solvers a wing with large aspect-ratio is considered ($AR = 30$) and the evaluation of the lift coefficient is done at its mid-station. The simulation is run considering $\Delta t V_\infty/c = 1/8$. Results are shown in Fig. 6, where the lift coefficient normalized to the steady lift coefficient is plotted against the reduced time, for both the rigid and deformable wake approaches. Results

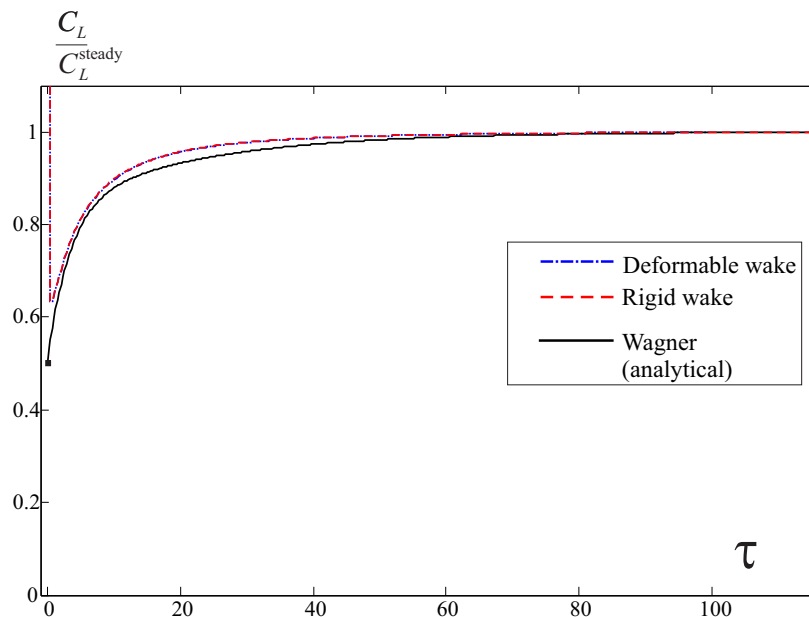


Fig. 6. Results of Wagner's test case using a rigid and a deformable wake: lift coefficient normalized to the steady lift coefficient plotted against the reduced time. The analytical solution is obtained from [76]

are in satisfying agreement.

B. Validation of the Meshless Transferring Capability

Validation of meshless capability has been carried out whereas this is not pursued here for the spline interface (validations were already performed in previous works using the same framework). Since *Solver1* relies

on IPS, a modified version of this solver has been implemented featuring the meshless for the load and displacements transferring. Then, a joined-wing configuration is considered, as the one depicted in Fig. 7. Notice that, this same configurations will be a test case geometry for this paper. A freestream speed of 55 m/s is considered, and the angle of attack α , measured in the symmetric xz plane, has the evolution depicted in the same graph. The results are in an excellent agreement, especially considering that at these large displacements the infinite spline method may begin to have issues related to its formulation, i.e., the assumption of constant projection of the points is no longer exactly satisfied. This results, beside other cases not reported here for brevity, may be considered as a valuable validation for the meshless method.

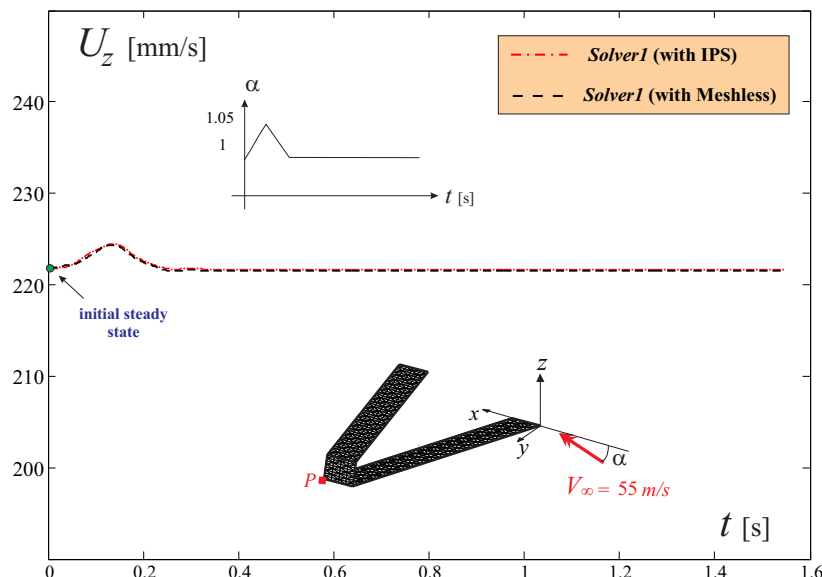


Fig. 7. Aeroelastic transient analysis of a Joined Wing configuration studied the *Solver1* when employing both IPS and Meshless transfers method.

C. Final Validation of the Time Domain Aeroelastic Codes Capabilities

In this final subsection the three time domain solvers are validated against experimental results which are proposed in reference [77]. It consists of a delta wing plate model tested in a low-speed wind tunnel showing limit cycle oscillations. For the geometry and details about the configuration the reader is referred to the original work. This experiment is also performed numerically by the solvers, and results are directly compared with the reference experiment, as well as computational results reported in [37], obtained with a technique that transforms the frequency domain DLM results in time domain response.

1. *Solver1*

Numerical results obtained with *Solver1* are shown in Table 1. To favour the comparisons, the first two columns report reference results, where as the third and fourth show the performances of *Solver1* with two different values of structural damping. Maximum vertical speed of the tip for LCO established at different

	Attar et Al.[77] (experimental)	Demasi et Al.[37]	<i>Solver1</i> $\zeta=3\%$	<i>Solver1</i> $\zeta=5\%$
Flutter velocity	24 m/s	22,7 ($\zeta=1\%$)	24 m/s	24,5 m/s
$\dot{U}_{z_{tip}}$ ($V_{\infty}=25,5$ m/s)	0,5 m/s		0,69 m/s	0,63 m/s
$\dot{U}_{z_{tip}}$ ($V_{\infty}=27$ m/s)	1,36 m/s	1 m/s ($\zeta=5\%$)	1,28 m/s	1,07 m/s
LCO frequency ($V_{\infty}=27$ m/s)	14,5 Hz	14.92 Hz ($\zeta=5\%$)	15,3 Hz	14,8 Hz
$\dot{U}_{z_{tip}}$ ($V_{\infty}=28$ m/s)	1,85 m/s	1,55 m/s ($\zeta=3\%$)	1,5 m/s	1,3 m/s

Table 1. Validation of *Solver1* with Delta Wing test case. $\dot{U}_{z_{tip}}$ is the maximum vertical speed of the tip of the wing.

wind speed are also represented in Fig. 8.

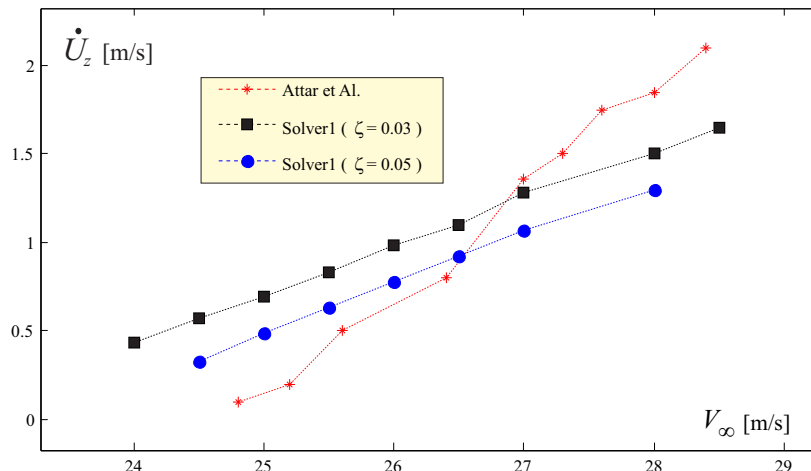


Fig. 8. Results of Delta Wing test case: experimental [77] *Solver1*. The maximum vertical speed of the wing's tip is plotted against the wind speed.

2. *Solver2*

Numerical data for *Solver2* are now shown in Table 2. Maximum vertical speed of the tip for LCO established

	Attar et Al.[77] (experimental)	Demasi et Al.[37]	<i>Solver2</i> $\zeta=3\%$	<i>Solver2</i> $\zeta=5\%$
Flutter velocity	24 m/s	22,7 ($\zeta= 1\%$)	23 m/s	23,5 m/s
$\dot{U}_{z_{tip}}$ ($V_\infty=25,5$ m/s)	0,5 m/s		0,9 m/s	0,66 m/s
$\dot{U}_{z_{tip}}$ ($V_\infty=27$ m/s)	1,36 m/s	1 m/s ($\zeta= 5\%$)	1,36 m/s	1,23 m/s
LCO frequency ($V_\infty=27$ m/s)	14,5 Hz	14.92 Hz ($\zeta= 5\%$)	16 Hz	15,3 Hz
$\dot{U}_{z_{tip}}$ ($V_\infty=28$ m/s)	1,85 m/s	1,55 m/s ($\zeta= 3\%$)	1,55 m/s	1,37 m/s

Table 2. Validation of *Solver2* with Delta Wing test case. $\dot{U}_{z_{tip}}$ is the maximum vertical speed of the tip of the wing.

at different wind speeds is also represented in Fig. 9.

3. *Solver3*

The same process is repeated for *Solver3*. See Table 3. Maximum vertical speed of the tip for LCO established

	Attar et Al.[77] (experimental)	Demasi et Al.[37]	<i>Solver3</i> $\zeta=3\%$	<i>Solver3</i> $\zeta=5\%$
Flutter velocity	24 m/s	22,7 ($\zeta= 1\%$)	24 m/s	24,5 m/s
$\dot{U}_{z_{tip}}$ ($V_\infty=25,5$ m/s)	0,5 m/s		0,77 m/s	0,57 m/s
$\dot{U}_{z_{tip}}$ ($V_\infty=27$ m/s)	1,36 m/s	1 m/s ($\zeta= 5\%$)	1,18 m/s	1 m/s
LCO frequency ($V_\infty=27$ m/s)	14,5 Hz	14.92 Hz ($\zeta= 5\%$)	15,6 Hz	15,1 Hz
$\dot{U}_{z_{tip}}$ ($V_\infty=28$ m/s)	1,85 m/s	1,55 m/s ($\zeta= 3\%$)	1,47 m/s	1,34 m/s

Table 3. Validation of *Solver3* with Delta Wing test case. $\dot{U}_{z_{tip}}$ is the maximum vertical speed of the tip of the wing.

at different wind speed are also represented in Fig. 10.

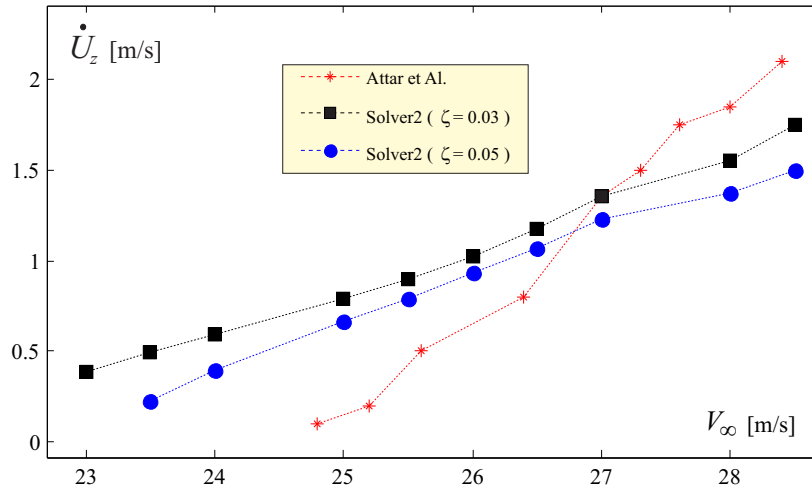


Fig. 9. Results of Delta Wing test case: experimental [77] and *Solver2*. The maximum vertical speed of the wing's tip is plotted against the wind speed.

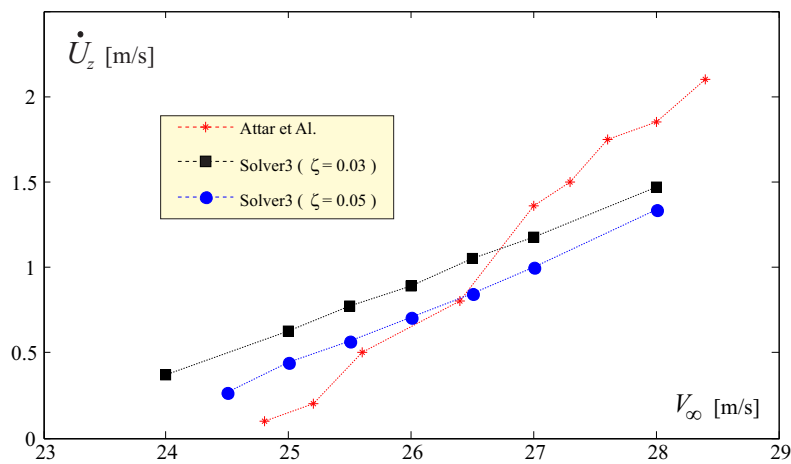


Fig. 10. Results of Delta Wing test case: experimental [77] and *Solver3*. The maximum vertical speed of the wing's tip is plotted against the wind speed.

V. Description of the Analyzed Joined-Wing Configurations

There are different configurations that will be analyzed in this paper. The first one, depicted in Fig. 11, is a Joined Wing (named *JW70*) in which the joint is not located at the tip of both the wings. The thickness of the wings and the joint is 0.7 mm .

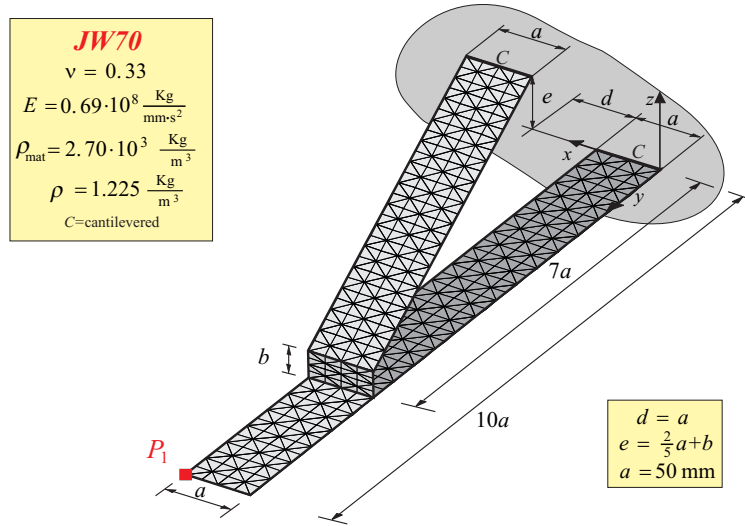


Fig. 11. JW70 model. The joint is located at 70% of the wing span. The thickness of the different parts of the structure is equal to 0.7 mm .

The second configuration (Fig. 12) is a PrandtlPlane-like [2] configuration featuring a swept-back lower wing and a swept-forward upper wing. It is designated *PrP40*. For this layout, the thickness of the wings is varied and specified case by case. Both *JW70* and the *PrP40* have been chosen for reference reasons,

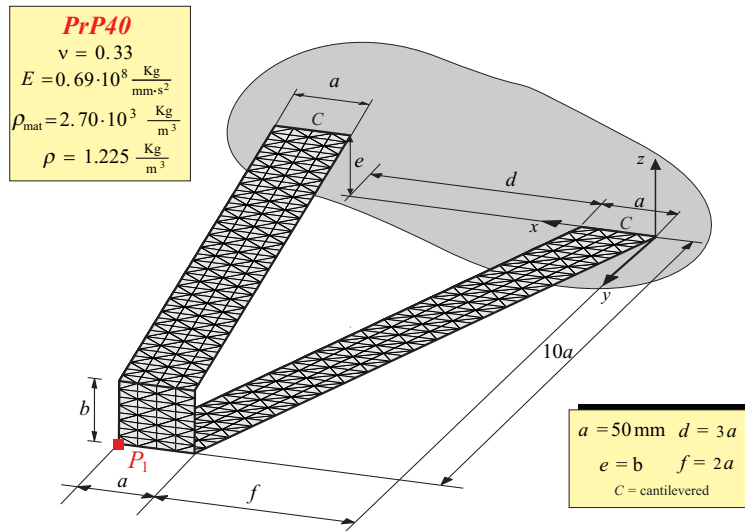


Fig. 12. PrandtlPlane Joined Wing model PrP40. The joint is located at the tip of the wings.

see [4, 11, 13, 16]. The models' dimensions are selected to be consistent with the ones corresponding to wind-tunnel scaled models.

The last layout (Fig. 13) is the typical *Sensorcraft* [78]. The geometrical details are taken from reference [79], a part from the thickness which has been set to 0.7 mm . In this configuration the aft wing is directly joined to the front wing, to act like a strut.

For all the layouts the adopted material is a typical Aluminium, featuring a Young's modulus $E =$

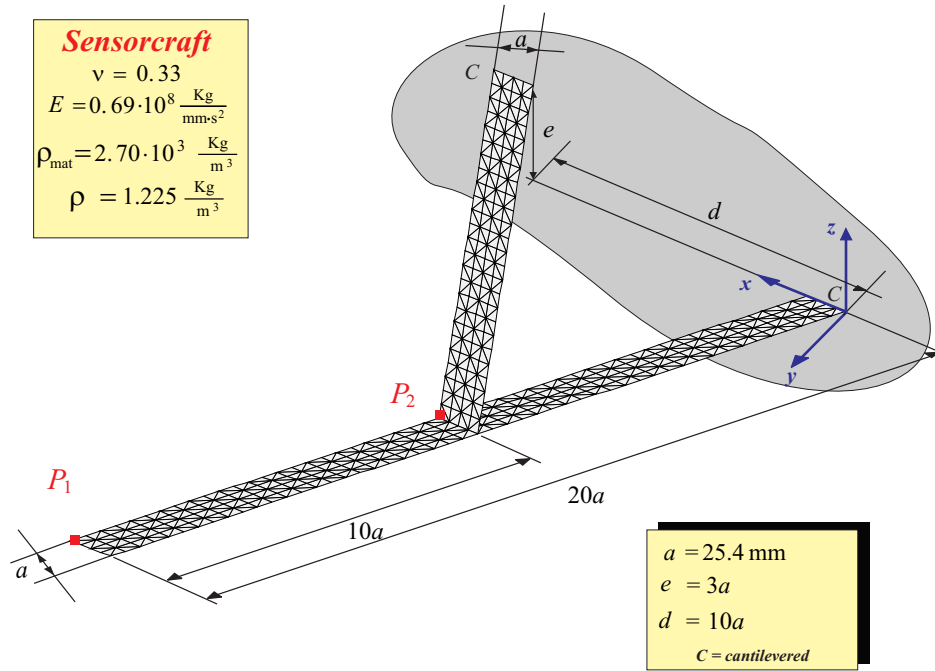


Fig. 13. *Sensorcraft*. The aft wing is connected to the front one at the midspan. The thickness of the wings is equal to 0.7 mm.

$6.9 \cdot 10^7 \left[\frac{\text{Kg}}{\text{mm} \cdot \text{s}^2} \right]$, a Poisson's ratio $\nu = 0.33$ and a density $\rho_{\text{mat}} = 0.69 \cdot 10^3 \text{ kg/m}^3$.

For the aerodynamic analysis, the surface is discretized employing different (usually about 12) elements in the chordwise direction. The overall number of rectangular elements is then between approximately 600 and 3000 for the different cases.

The density of the air is chosen to be the standard air density ($\rho = 1.225 \text{ kg/m}^3$).

VI. Snap Divergence

The concept of *snap divergence* was first introduced in references [13, 80]. It was related to a precise mathematical event, which was the singularity of the aeroelastic tangent matrix. For that critical condition an infinitesimal increment in the onset flow speed was determining an equilibrium not continuously adjacently to the previous one. In other words, a jump phenomenon (from which the word *snap*) was expected. This jump phenomenon could be theoretically demonstrated to happen if the acting forces are of the conservative type, and this actually is pursued and shown in [11, 12]. However, aerodynamic forces are not of the conservative type and the scenario could be much more complicated. First of all, for the case here investigated it has been verified (and will be reported in next sections) that flutter speed is larger than snap-divergence one, thus, the stability (in a local sense) of the equilibrium points could be assessed with static aeroelastic analysis. Moreover, different-than-fixed points type of attractors may theoretically exist, with the consequence that snap may even induce the system to settle, for example, to a limit cycle oscillation.

In this section the snap-divergence response will be shown. The time-domain capability is used, in particular *Solver1*. This choice is dictated by the necessity to keep the aeroelastic modelling consistent to the one used in references [13, 80].

A. Time response on Snap-divergence Occurrence

Consider the static aeroelastic response reported in Fig. 14 (taken and adapted from Refs. [13, 80]). Starting from the steady state A, a perturbation in the onset velocity is applied.

Before describing the perturbation application, it is worth to explain how the simulation was started. The steady state aeroelastic solver was using horse shoe singularities to represent the bound vorticity, whereas in the time domain dynamic capability a vortex ring representation is used. Equivalence has been imposed on the aerodynamic loads, determining thus the circulation of the vortex rings. A further point is the fact that static solutions were considered converged after a tolerance on the residual was reached. Of course, in a real numerical setting it is not possible to reach the perfect equilibrium. Thus, it has been checked that the numerical unbalance was negligible.

With the starting condition (state A in Fig. 14, corresponding to a free-stream speed of $V_\infty = 33$ m/s), the flow speed is first increased to reach $V_\infty = 34.3$ m/s (state B), then decreased to its initial value. This is process a quasi-static process, as could be inferred from the box in Fig. 14, where the wind speed in respect of time is plotted.

Tracking the dynamic response, as long as the speed approaches values close to the one of *snap-divergence*, there is an abrupt increase in the displacement of the wing tip (measure of the deformation of the structure). Comparing the displacements for the static and dynamic cases, the snap-divergence phenomenon may be well recognized. In the inverse phase, where the speed is decreased to its initial value, similar trend is observed and the initial static equilibrium condition is obtained at the end of the transient. Further looking at the response, the inertial effects seem to be of secondary importance in this specific case, in fact no oscillation is observed.

Summarizing, the dynamic response matches closely the static one.

VII. Flutter Evaluated with Linear and Nonlinear Analyses

This section shows how linear and nonlinear tool may predict notably different flutter speeds. As already outlined in section III, the here considered nonlinearity is relative to the large displacement of the configurations (geometric nonlinearity). This comparison was already pursued in [4, 13, 80], for mechanical loading and static aeroelastic conditions, respectively. It was assessed that linear analysis may give unreliable and nonconservative predictions. In some cases linear tools were not even able to correctly evaluate trends when one or more parameters were varied.

In this section the difference between the two approaches from an aeroelastic dynamic point of view is pursued by means of the frequency domain (DLM) solver, see [37]. This solver requires the modes of the structures as an input. Thus, as it will be shown, the process of running different analyses with modes representative of the undeformed or deformed structure is the keypoint in which nonlinear effects are introduced.

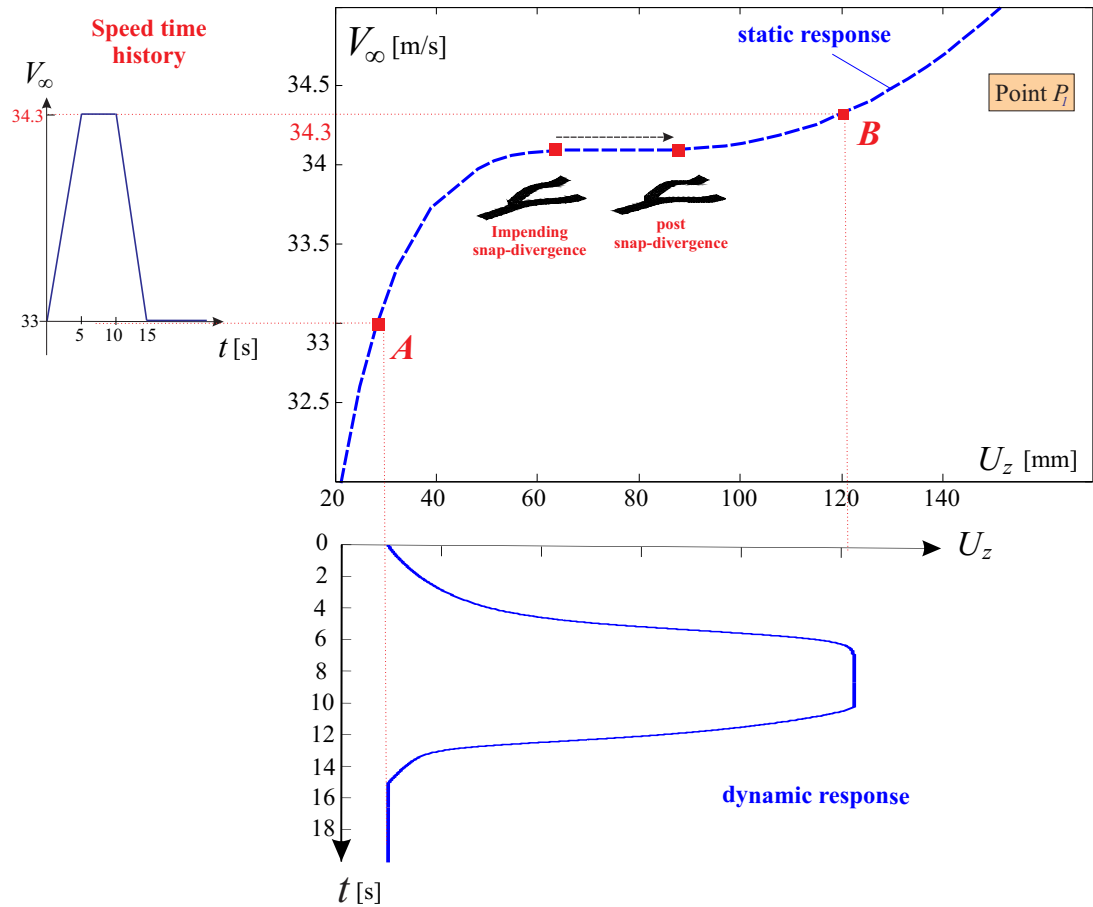


Fig. 14. Aeroelastic static response of *JW70*, speed perturbation in time, and aeroelastic dynamic response to the perturbation. U_z refers to the vertical displacement of the wing tip, point P_1 of Fig. 11.

A. PrP40

The already introduced configuration *PrP40* is first taken into consideration. As said, the DLM method requires the modes of the structures as an input. Thus, evaluating the modal properties of the structures at different point on the static aeroelastic response (the static aeroelastic equilibrium states can be found in [13] and are presented also in the next session), it is possible to have a progressively more refined estimate of the flutter speed (Hopf's bifurcation).

Results are relative to different structural damping values: a chosen value of damping ratio is applied to the considered modes, in the process explained in section III.B.5.

Flutter speeds are 51.5 m/s for the zero damping case, 52.2 when $\zeta = 0.01$, 53.7 when $\zeta = 0.02$ and 54.9 when $\zeta = 0.03$. Discrepancy of the flutter speed evaluated for the undeformed configuration (which is the common practice) and the real one is about 22%. Unfortunately, in this case the discrepancy is in the nonconservative side (overprediction of the critical condition). Actually, increasing the linearization speed enhances this mismatch, at least for a large portion of the response. Interestingly enough, an overprediction of the divergence speed was also found for the aeroelastic static case (see [13, 80]).

In literature it is claimed [81] that DLM model lacks in precision when used for cases in which wake roll-up plays an important role, or for case in which the structural deformation is conspicuous. In other works, e.g. [77], the real wake geometry was judged to be not influent for the specific aeroelastic case under examination. In this regard, next section which will focus more on the LCO, will also present a comparison among flutter speeds predicted with different approaches (frequency vs time domain) and models.

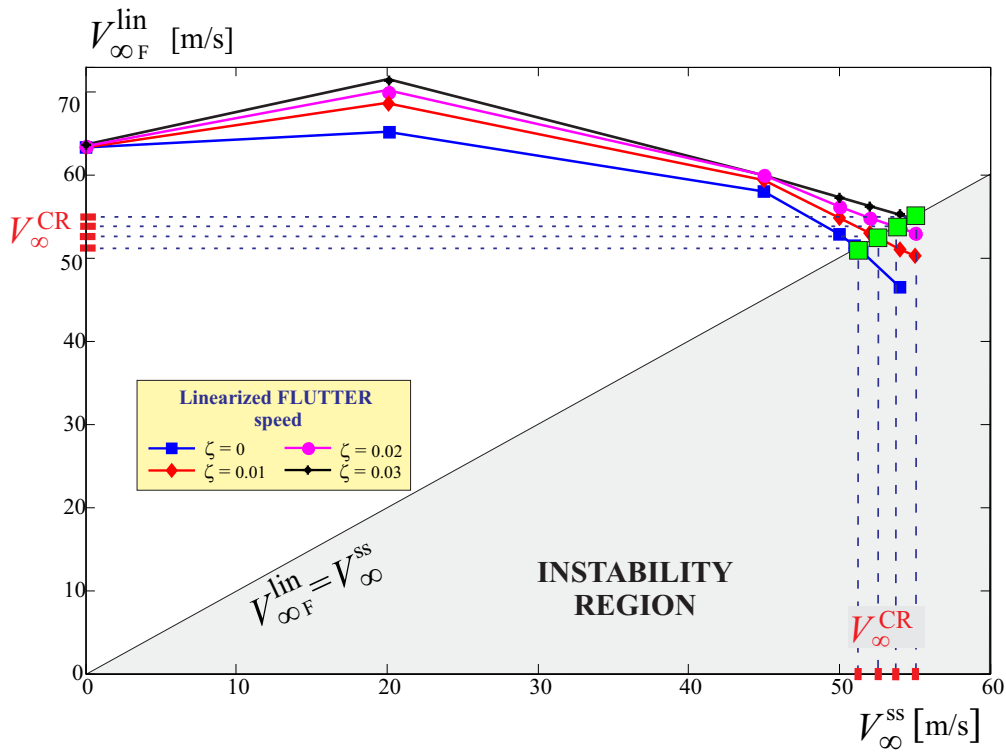


Fig. 15. Flutter speed predicted linearizing about steady state relative to different flow speeds for *PrP40*. The real critical condition (*nonlinear flutter*) happens when these two speeds coincide.

B. Sensorcraft

Here the *Sensorcraft* is considered. Results are shown in Fig. 16. The interesting property of this configuration is the relatively smaller deformation consequences of the chosen geometric properties (this will be better characterized in next section). However, as it could be appreciated, there is still a non-negligible over-prediction of the linear tool. In fact, considering the zero-damping case, the linear prediction gives 59.1 m/s against the 51.6 m/s, with a difference of approximately 15%.

A further aspect to underline is the relative insensitiveness of the flutter speed in respect of the structural damping. This was not the case for the previously examined configuration.

It is interesting to observe that, linearizing about a speed other than the fundamental (zero) one, the flutter prediction instead of being more precise, may actually lead to larger errors. This was observed also for the *PrP40* case, suggesting that, evaluation done with immediate successive linearization may give misleading trends and even more inaccurate predictions, unless the linearization speed is close to the real critical one. These results stress out the big role played by the nonlinearities in Joined Wings configurations.

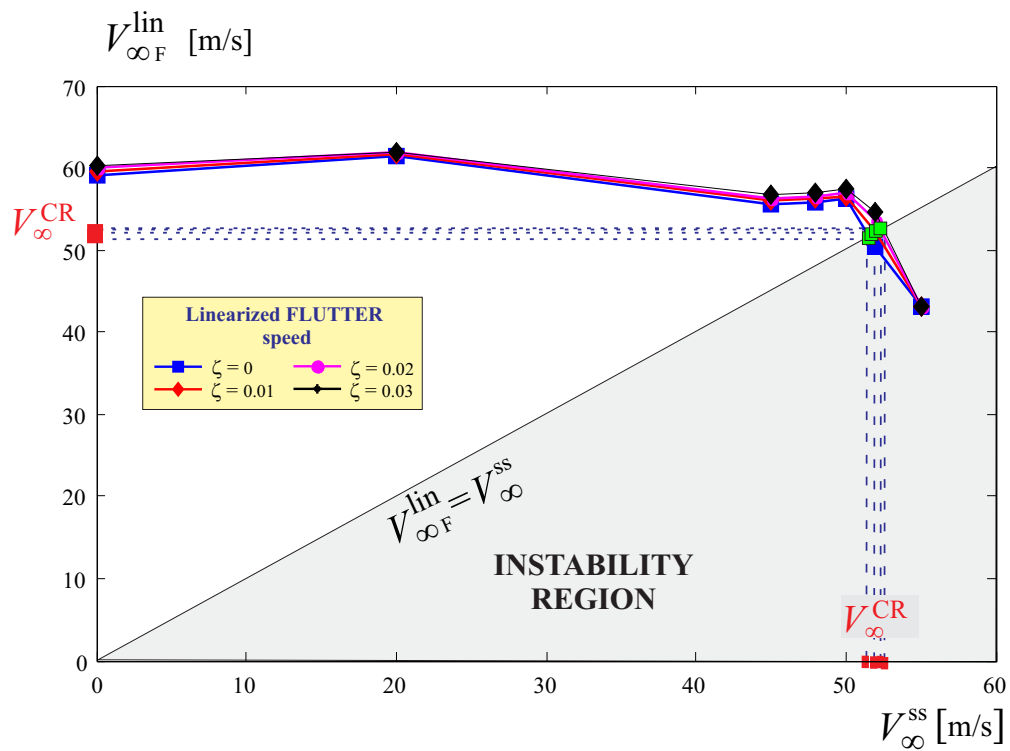


Fig. 16. Flutter speed predicted linearizing about steady state relative to different flow speeds for *Sensorcraft*. The real critical condition (*nonlinear flutter*) happens when these two speeds coincide.

VIII. Postcritical Dynamic Aeroelastic Analysis

In this section different results are shown. Flutter speed as predicted by the time- and frequency-domain solvers are compared, for different values of the damping ratio. For the post-flutter, different dynamic responses, in particular Limit Cycle Oscillations (LCO), are observed for the baseline configurations. These LCOs are obtained perturbing the steady state, or, alternatively, increasing the angle of attack until the target value is reached. The sophistication of the analyses is mitigated by the use of all the solvers as an important mean of comparison and validation. The discrepancies observed when different solvers are employed is discussed in more depth and a physical interpretation of these differences is also attempted, when possible. The outcome of this analysis has important consequences since it suggests which solver should be used to reach a good balance between reliability and computational costs.

A. Limit Cycle Oscillation for JW70

The previous sections gave both a static and dynamic evaluation of the aeroelastic properties of the joined-wing configurations under examination. In particular, flutter speed was assessed with frequency domain solver. In this regard, a time domain solver may be used to assess if the flutter speed was consistently predicted, and, also, to show the post-critical response. Moreover, solvers based on different modelling are used to provide an insight in what are the important requirements for this kind of problem, so that simpler and computationally less expensive solutions may be used with confidence.

1. Solver1

Fig. 17 shows the dynamic response of the *JW70* configuration evolving from an equilibrium state as the ones depicted in the graph. For each case, a vanishing angle of attack perturbation is given to provoke a more observable transient, and eventually induce more rapidly a post-flutter behaviour. This perturbation consists in a linear increase in the angle formed by the onset flow direction and the x -axis, followed by a symmetric decrease to the unperturbed value (which is 1°). The peak is reached at 0.1 seconds, and at its value it holds that $\alpha_x = 1.01$ (this is shown in the box in Fig. 17).

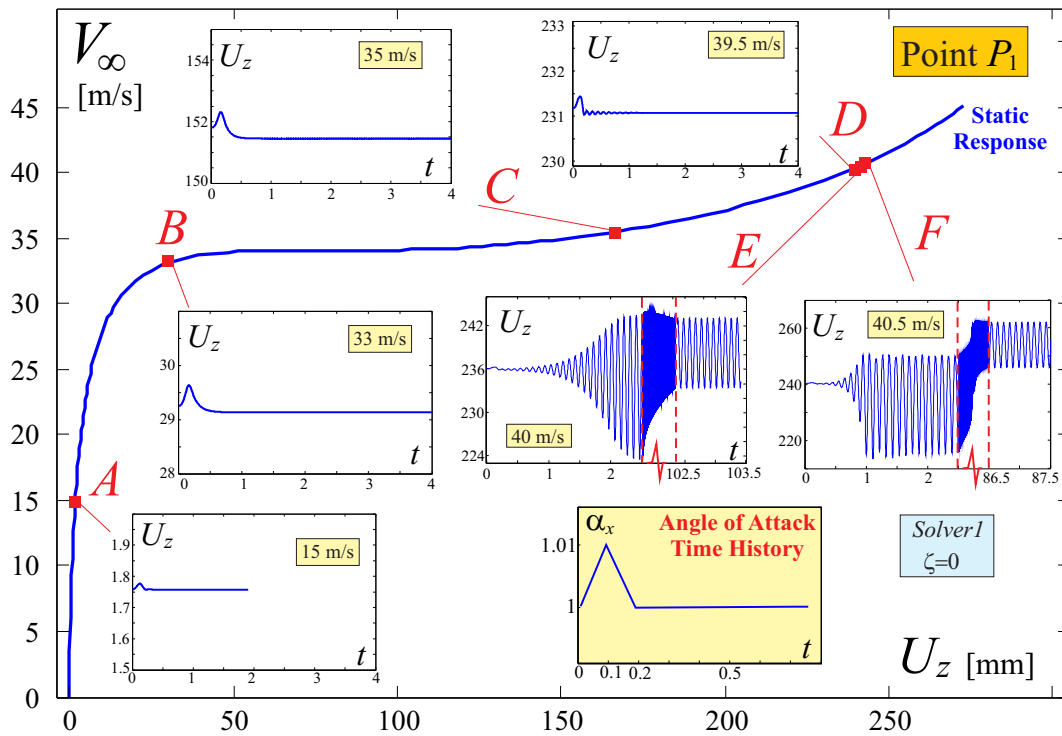


Fig. 17. *Solver1*. Aeroelastic dynamic response of *JW70* starting from steady states relative to different velocities when a vanishing perturbation in angle of attack of the onset flow is given.

All the results have been obtained considering no structural damping. The simulations have been carried out for different speeds, so that both the typical subcritical and supercritical responses could be appreciated. In particular, with this approach, it is possible to locate a small interval in which the flutter speed lies (according to this solver). For the present case, the flutter speed falls in the interval $39,5 \div 40$ m/s. These results are analyzed and discussed in more depth in section 4.

For speed larger than flutter, an LCO is observed. The properties of the LCOs are depicted in Fig. 18. Very interesting is the transient of system before settling to an LCO. Not only the path described in the space

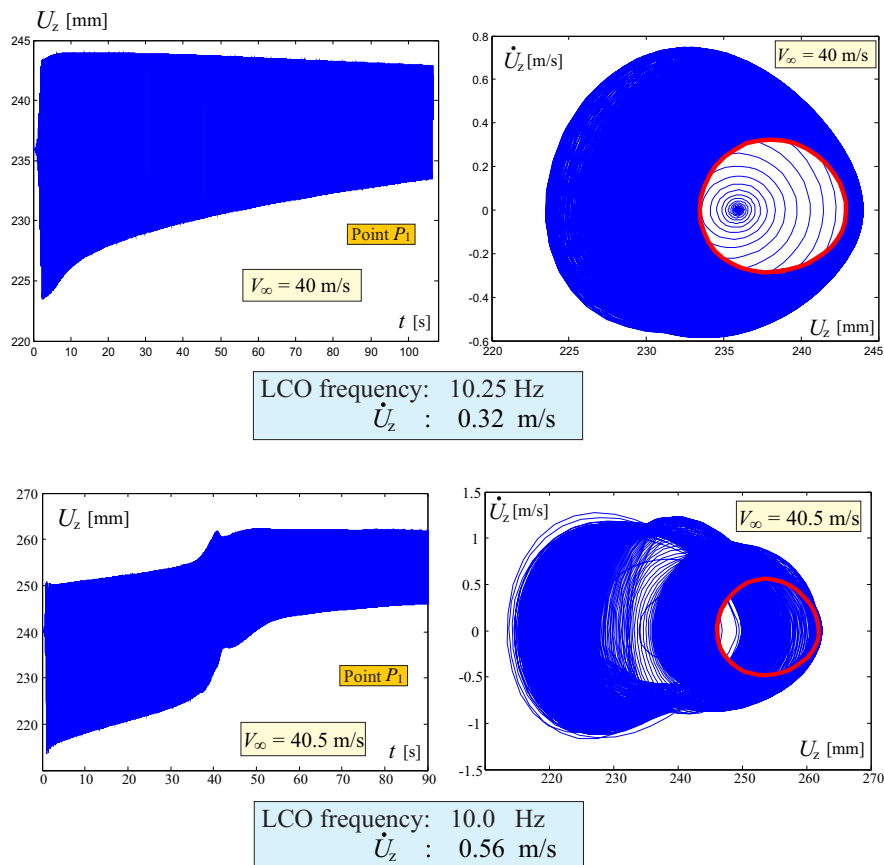


Fig. 18. Time response and Phase-space trajectory for *JW70* configuration, for different flow speeds. *Solver1* is employed. No structural damping is considered.

phase is long before it is finally attracted from the LCO orbit. But, for a wind speed of $V_\infty = 40.5$ m/s it has also an abrupt change in the oscillatory trend. It is the authors' opinion, and actually, it may be supported by physical sense, that this behaviour is largely due to the overconstrained nature of the joined-wing layout. The mutual loads transferred through the joints give raise to a complicated response. This could be easily verified comparing the transient to the LCO shown above with the ones of the Delta Wing case (see reference [37]).

2. Solver2

The same process outlined in the previous section is now repeated using a different aerodynamic solver. The difference with the previous case is concentrated in a more consistent application of the boundary condition (which requires the re-evaluation of the aerodynamic tangent matrix at each timestep) and also the application of the Kutta-Joukowski formula on the real deformed structure. Moreover, all the aerodynamic/structural information are passed thanks to a meshless method. Refer to section III.F for more details.

The static response, used to start a simulation from a steady state condition, is depicted in Fig. 19. It is obtained with a static aeroelastic tool consistent with the above employed hypotheses. It may be well noticed that the snap-divergence has now a more pronounced connotation.

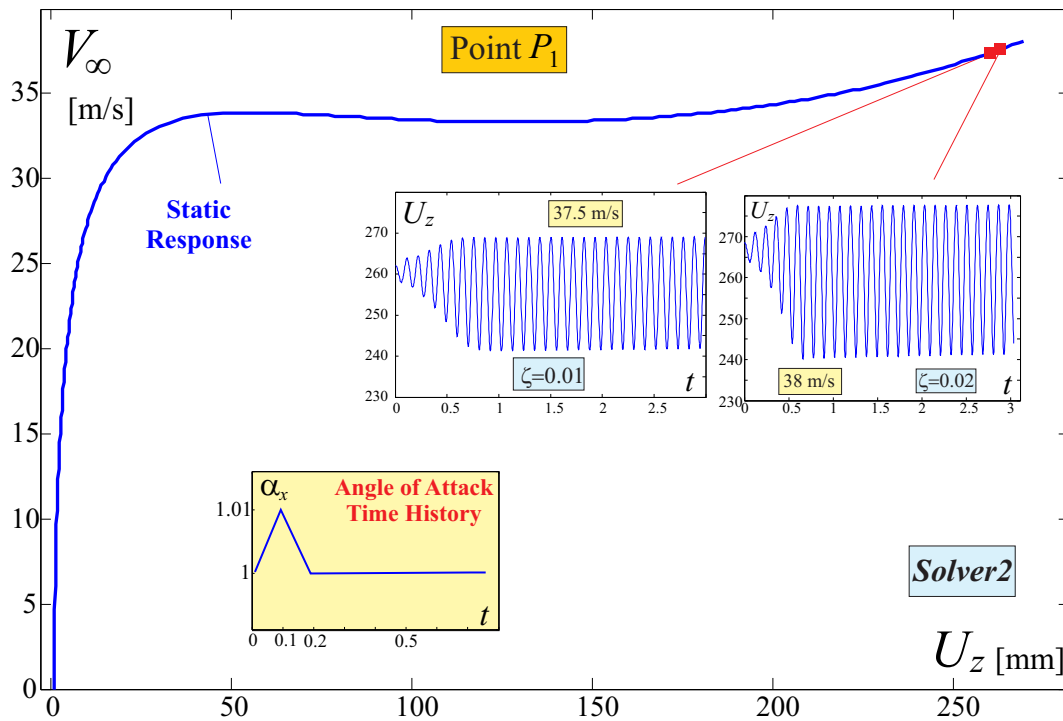


Fig. 19. *Solver2*. Aeroelastic dynamic response of *JW70* starting from steady states relative to different velocities when a vanishing perturbation in angle of attack of the onset flow is given. Different structural damping are considered.

In the same figure and in Fig. 20, the dynamic responses obtained starting from different steady velocity and applying the above described perturbation are given. It may be observed how, with this more realistic modelling, the flutter speed sensibly decreases if compared with the outcome of the above analyses. In fact, even for structural damping ratio of ζ different than zero, and speeds that were subcritical (in term of flutter) when the case was analyzed with the *Solver1*, an LCO is observed.

3. Solver3

The capability of free wake is considered in *Solver3*. The vortex rings are now considered attached to the structure. Thus, differently than *Solver2*, there is a perfect consistency between the control point where boundary condition is applied and inducing singularities panels. Refer again to section III.F for more details.

To consistently compare the results with the the ones presented above, it is necessary to find a suitable steady state condition. There are two generic ways to achieve a steady state. One method is based on an iterative process starting from an initial first guess wake geometry, moving it accordingly with the induced velocity components parallel to a plane perpendicular to the free-stream velocity (see [62]). A further way to proceed, is just to start from a rest condition and follow the transient until a steady state is reached.

Here, an approach similar to the second one is employed. In fact, an impulsive start is given to the configuration, and the angle of attack is slowly increased until it reaches the sought value (in Fig. 21 is depicted the time history of the nominal angle of attack). When these simulations are carried out for larger speeds than the flutter one, then, obviously, a steady state is not observed. Results are summarized in Fig. 21. The time histories suggest that the flutter speed lies in the $36 \div 38$ m/s range, probably closer to 38 m/s. In fact, the LCO observed at this speed has a very limited amplitude, indicating that the state is one immediately following a Hopf's bifurcation. With a small increase in speed, the LCO has a larger amplitude. With a further increment of speed, the response does not seem to have any periodicity, suggesting a transition toward chaos. A in depth analysis is needed to affirm and demonstrate the above possible chaotic behaviour.

It is very interesting to notice how a relatively small variation in speed (see Fig. 21) significantly changes the kind of response.

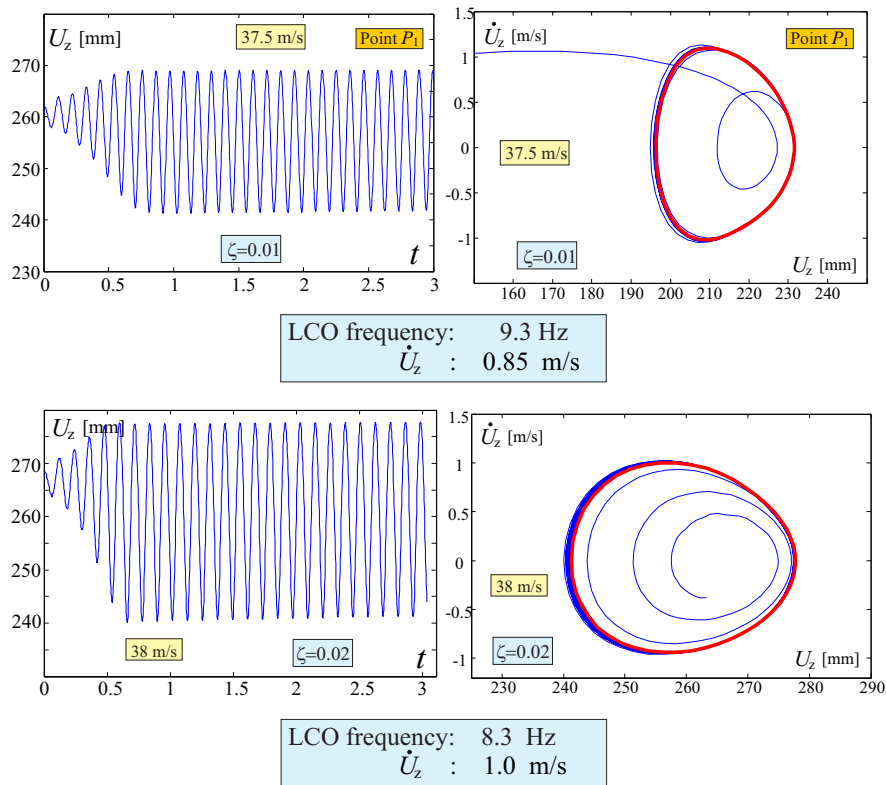


Fig. 20. Time response and Phase-space trajectory for *JW70* configuration, for different flow speeds. *Solver2* is employed.

4. Effects of Solver's Choice and Structural Damping on Flutter Speed

In Fig. 22 it is plotted the flutter speed, as evaluated with the different solvers, with respect to the structural damping ratio. The critical speeds evaluated with the time domain solvers are obtained by considering the two successive speeds for which the response was showing and was not showing an LCO. In the graph, the DLM overestimates the flutter speed in respect with all other methods. In particular, *Solver1* uses the same aerodynamic and load transferring of the DLM one, thus, to prove that this difference is not an artifact of numerics, the number of natural modes, aerodynamic panels and structural elements have been verified to be enough to give convergent results (the details are here omitted for brevity).

Solver2 gives lower flutter speeds. Applying the lift in the appropriate direction and consider the real normal in the application of the boundary condition exacerbates the bending actions. However, in general, even if in agreement with intuition, this may not always hold. For example, it will be shown for the *PrP40* layout that this is not the case.

With *Solver3*, the singularities are bound to the structure, and the wake is free to deform and evolve. Especially this last features has a relevant role in increases the critical speed.

All the solvers show a similar trend of the flutter speed with the structural damping.

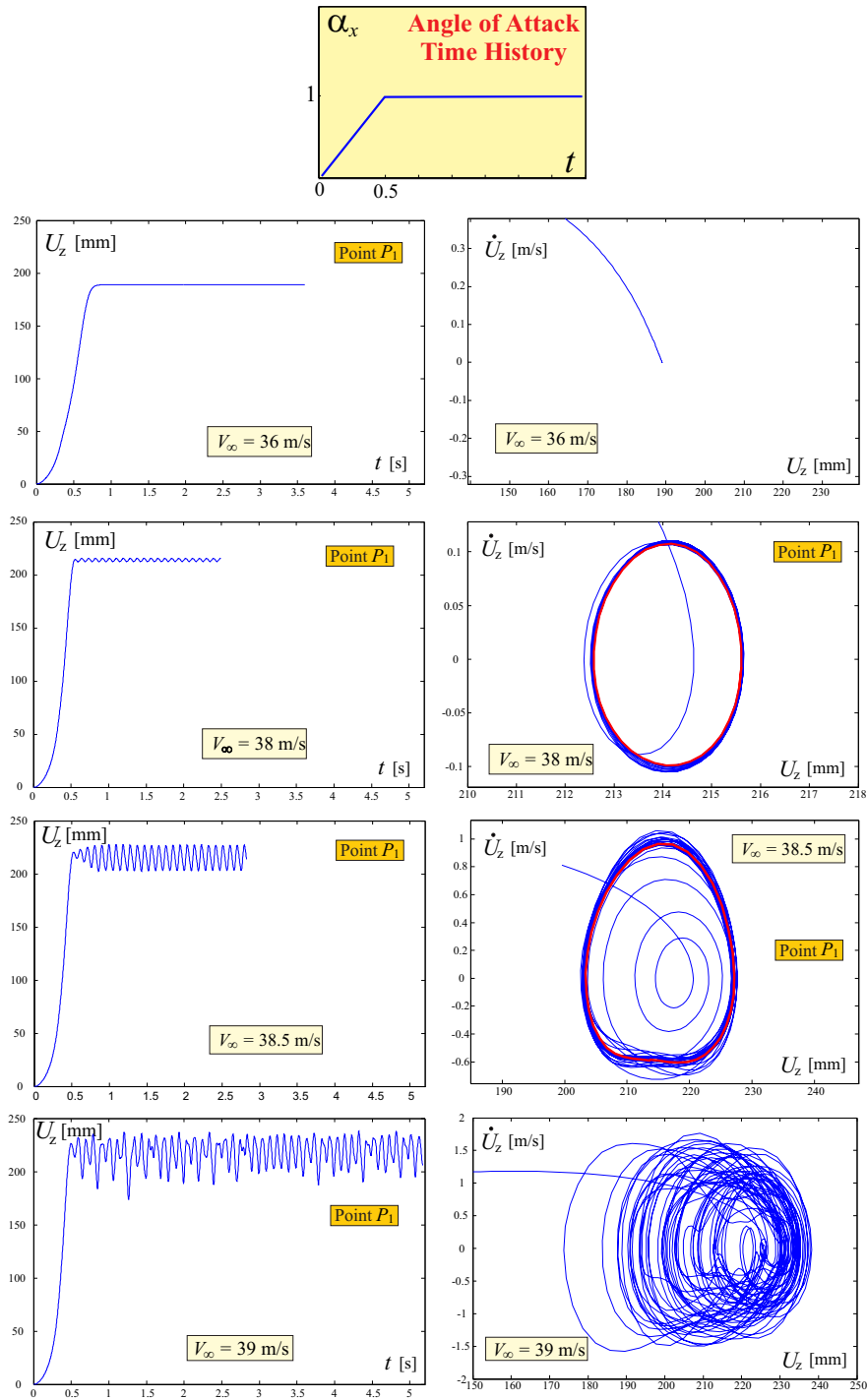


Fig. 21. Time response and Phase-space trajectory for *JW70* configuration, for different flow speeds. *Solver3* is employed. The angle of attack is increased linearly from 0° to 1° in 0.5 seconds. No structural damping is considered. The *LCO* observed at a speed of $V_\infty = 38$ m/s has a frequency of 10.8 Hz. The one at $V_\infty = 38.5$ m/s has a frequency of 10.5 Hz.

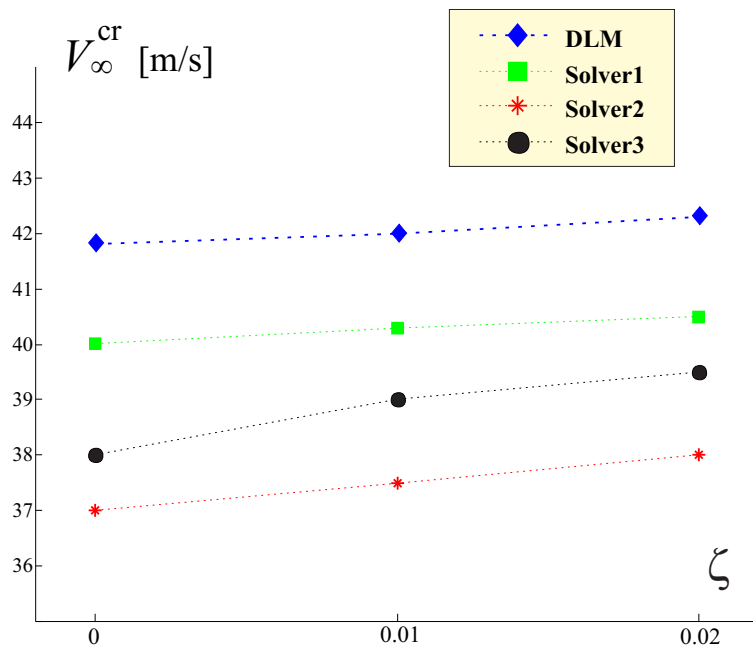


Fig. 22. Flutter speeds for *JW70* configuration, evaluated with the different solvers and for different structural damping ratio values.

B. Limit Cycle Oscillation for PrP40

This section retraces the logics of the previous part. However, the configuration under examination is now the *PrP40*. See Fig. 12 for details about the geometry. For this specific test case, the thickness of the wings is set to $t = 1$ mm. The modality of application of the perturbation strictly follows what done in the previous section.

1. Solver1

Fig. 23 shows both the aeroelastic static response, and the time evolution of the *PrP40* configuration starting from an equilibrium state depicted in the graph and experiencing a vanishing perturbation. This disturbance consists in a linear increase in the angle formed by the onset flow direction and the x -axis, followed by a symmetric decrease to the unperturbed value (which is 1°). The typical times are the same described in the *JW70* case. For all cases the structural damping is set to zero. Both configurations relative to subcritical and supercritical speeds are chosen.

The outcome of the simulations suggests that the flutter speed is in the $58 \div 59$ m/s range. Observing the response for speed larger than the flutter's one, it may be noticed how, differently than the *JW70* case, the response is not settling to his final LCO with the typical pattern observed before, in which the oscillating motion was very slowly cutting its amplitude and shifting its mean value before reaching the asymptotic behaviour. On the contrary, after a very brief peak, the response immediately sets to the asymptotic mean value, and the amplitude of the oscillation rapidly reaches the regime one. This could be observed with the

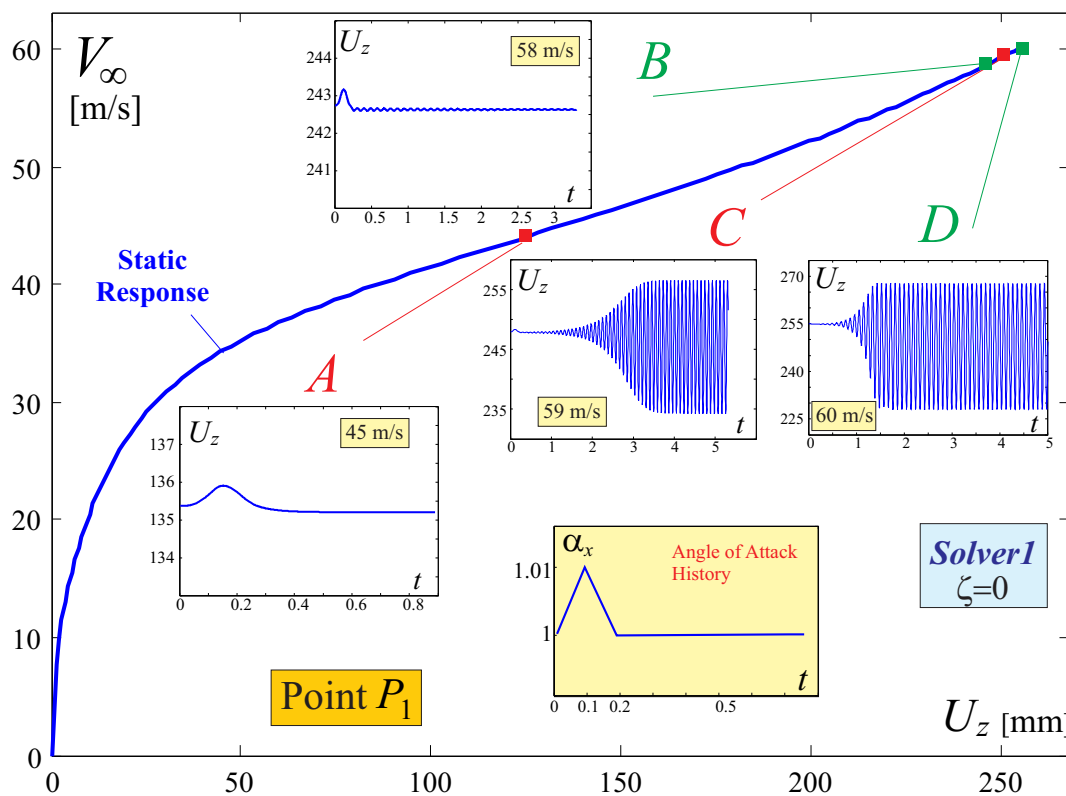


Fig. 23. *Solver1*. Aeroelastic dynamic response of *PrP40* starting from steady states relative to different velocities when a vanishing perturbation in angle of attack of the onset flow is given.

aid of Fig. 24.

Repeating the simulation with a value of the damping ratio $\zeta = 0.03$ the critical speed increases, however, the time response reminds the ones of the undamped system. Thus, this cases are not shown here for brevity.

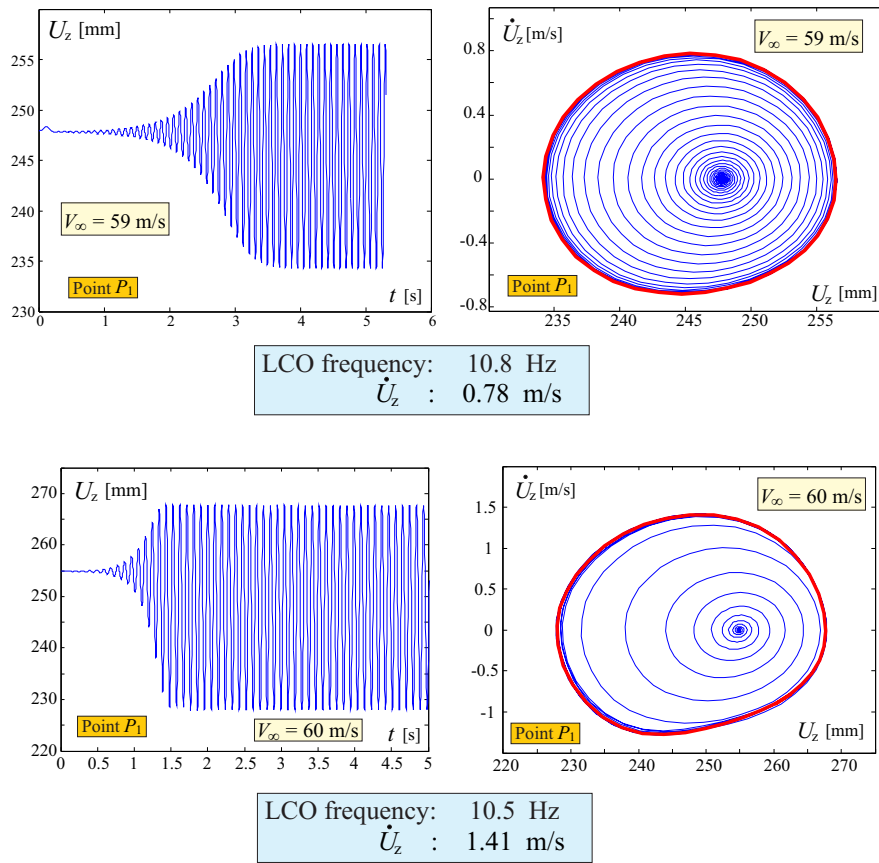


Fig. 24. Time response and Phase-space trajectory for *PrP40* configuration, for different flow speeds. *Solver1* is employed. No structural damping is considered.

2. Solver2

The static aeroelastic response is first obtained in a way consistent with the hypothesis of the aerodynamic solver. Then, picking a speed, the initial configuration is automatically chosen, the perturbation is applied and the response is studied. Results are shown in Fig. 25, whereas the LCOs in the phase-space diagram are given in Fig. 26.

An interesting direct comparison of the LCO properties at a fixed speed (59 m/s) when choosing two different solvers is shown in Fig. 27. Exploiting the geometrical follower nature of the aerodynamic forces (taken into account with *Solver2*) has an important effect on the amplitude of the LCO, and also on the frequency: both of them increase by a considerable extent. Although it is always difficult to rely on intuition when studying flutter, the increase in amplitude “is expected” in the sense that a follower force tends to exacerbate the deformation.

3. Solver3

Time responses and phase spaces of the limit cycle oscillations found by means of the *Solver3* are not reported. However, the performances of this tool in predicting flutter speed are analyzed in the next section.

4. Effects of Solver’s Choice and Structural Damping on Flutter Speed

In Fig. 28 it is plotted the flutter speed, as evaluated with the different solvers, with respect to the structural damping ratio. Considering the undamped case, the DLM solver found a flutter speed of approximately 51.5 m/s, whereas, *Solver1* predicts a critical speed of 58.5 m/s. The relative error is in the order of 12%, definitely larger than the discrepancy observed for the *JW70* case. Further analyses are needed to explain

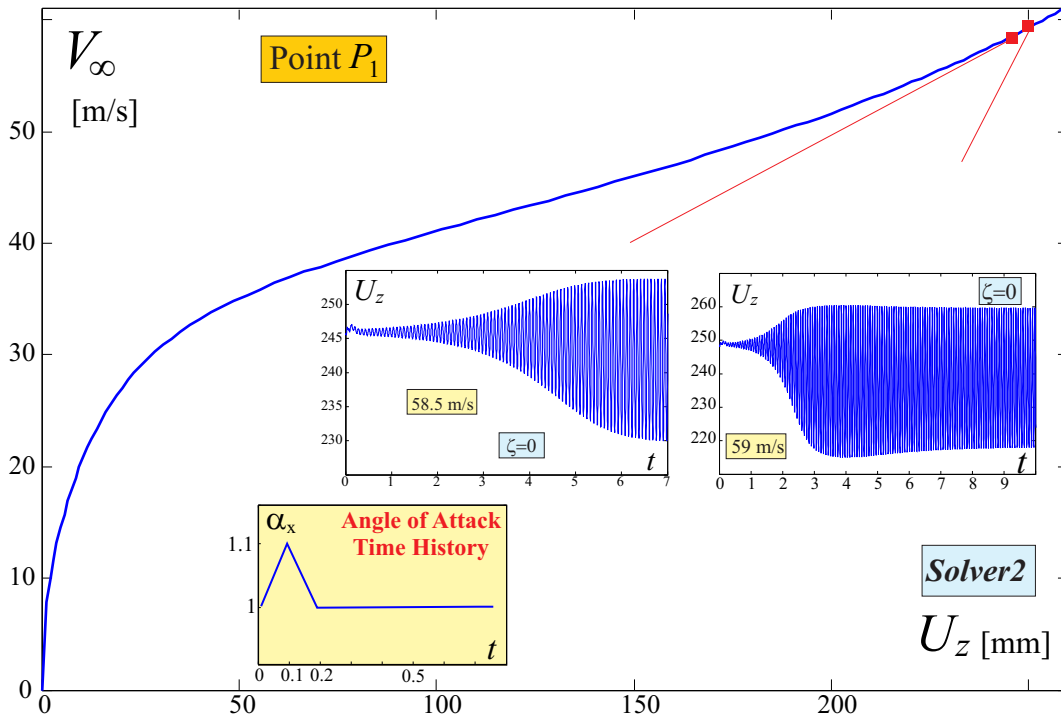


Fig. 25. *Solver2*. Aeroelastic dynamic response of *PrP40* starting from steady states relative to different velocities when a vanishing perturbation in angle of attack of the onset flow is given.

this difference. A further comment is that, differently than previous case, now the DLM predicts the lowest speed, giving thus a conservative estimation of the flutter speed.

Another difference from the *JW70* case is the higher flutter speeds predicted by *Solver2* when compared to *Solver1*, for nonzero damping ratios.

However, the most relevant observation is the discrepancy of *Solver3* with all other solvers. Here, an explanation is tempted based on physical arguments. Comparing *Solver3* with *Solver2* the most significant source of differences is the treatment of the wake. To isolate this effect, a pure aerodynamic case is introduced.

An impulsive start of an undeformable *PrP40*, immersed in a flow with an angle of attack of 5° is now considered. Both a rigid wake and a flexible (free) wake model are used. The lift coefficient evolution in time is depicted in Fig. 29. In the immediate transient there is a small difference between the lift coefficient which vanishes when evolving in time. If, for a time in which the global lift coefficients are identical, the lift distribution along the wingspan is compared, effects of the different modelling of the wake could be better appreciated. When free wake is modeled, there is a decrease, especially concentrated on the outer part of the upper wing, of the lift; on the other hand on the front wing there is an almost uniformly distributed increase.

A similar aerodynamic study was repeated for an unstaggered *PrandtlPlane*-like configuration: it was deduced that the large load redistribution due to wake deformation was not just strictly connected with the stagger of the *PrP40* configuration. Thus, it is expected that also the other joined-wing layouts experience a considerable load redistribution when a free-wake model is adopted. The question has still to be answered regarding why the *PrandtlPlane*-like configuration is much more sensitive to the wake modelling. The following speculative explanation could be attempted. It may be noticed that in this configuration both of the wings extend spanwise to the same amount, and the redistribution of loads on the wing-tip area has large bending moment effects due to the large moment arm with respect to the wing root. Thus, it seems reasonable to link these actions to a consistently different aeroelastic response. However, as said, this has to be demonstrated, especially considering that this redistribution is of course particular of the specific case under examination (undeformed wings), thus it is not immediate to extend these results to the real deformed case.

A further note about the redistribution is that, it would affect the induced drag of the configuration. This was already shown in reference [82], where a free-wake modelling was shown to predict a lower induced

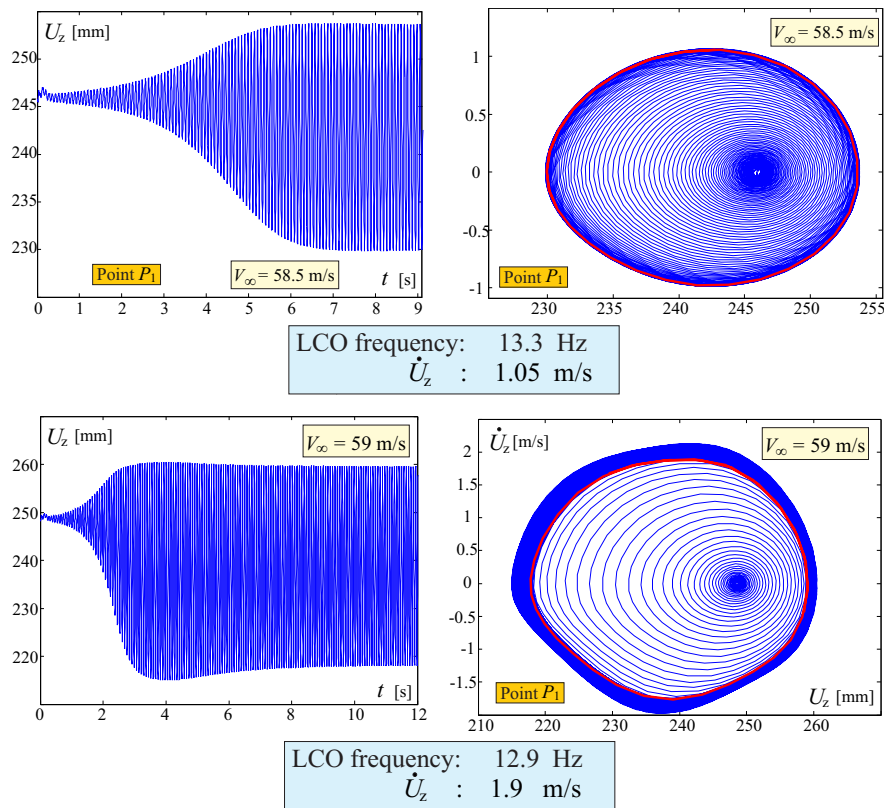


Fig. 26. Time response and Phase-space trajectory for *PrP40* configuration, for different flow speeds. *Solver2* is employed. No structural damping is considered.

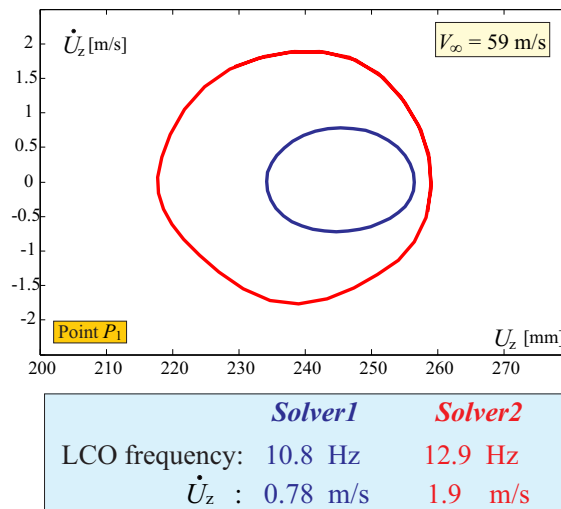


Fig. 27. LCOs of *PrP40* at a speed of $V_\infty = 59$ m/s as predicted by *Solver1* and *Solver2*.

drag whereas the lift coefficient was not experiencing differences. It is then suggested that, application of classic formulae [83–86] for a first evaluation of the induced drag may be slightly penalizing.

C. Sensorcraft

Now the *Sensorcraft* configuration is considered. The undisturbed flow forms with the x -axis an angle of 3° , and this enables to track an aeroelastic static response as shown in Fig. 30. The dynamic response is studied

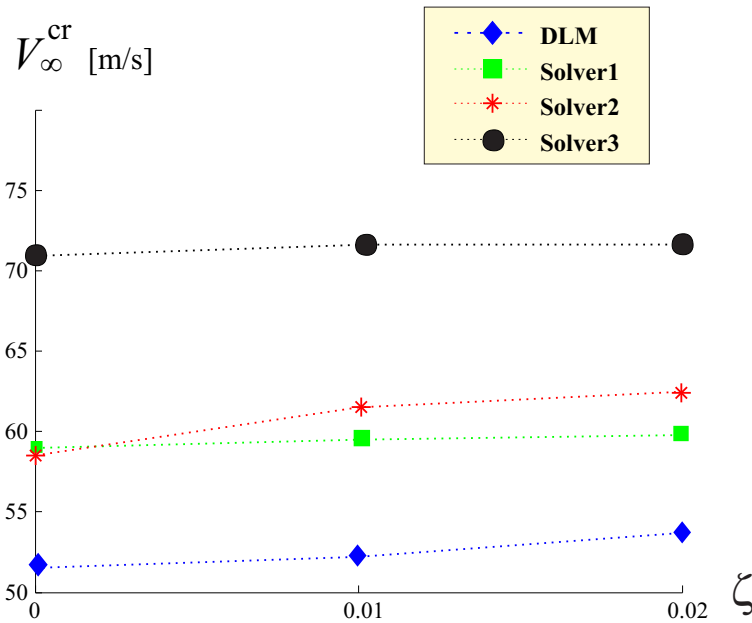


Fig. 28. Flutter speeds for *PrP40* configuration, evaluated with the different solvers and for different structural damping ratio values.

applying a vanishing perturbation in angle of attack, as described for the previous cases.

1. Solver1

Solver1 is here used to track the response. However, before further proceeding, it is interesting to comment the aeroelastic static response of this configuration, as shown in Fig. 30. It features the vertical displacement of both point P_1 , lying on the wing tip, and P_2 , at the midspan, as depicted in Fig. 13. The extreme nonlinear response presents a sequence of softening and stiffening. In the first stiffening region (for wing's tip), the deformation of the upper wing produces a bending moment transmitted directly to the lower wing, such that the tip of the wing does not experience any vertical displacement for a wide range of speeds.

Dynamic responses are presented in Fig. 31 for different speeds. Focus is first on the LCO for a speed of $V_\infty = 52.5$ m/s. Considering the midspan point P_2 , the trajectory described by this point when a limit cycle oscillation is established is the usual wave-like response. However, this does not hold for wing tip P_1 . In fact, considering a period, during the ascending part the motion is temporarily reversed and some higher frequency oscillations of smaller amplitude establish before continuing again the ascending motion. The descending motion does not show such a pattern. This response has been observed also when structural damping (algorithmic damping as explained in section III.B.2, has always been used in the present simulations) was considered (not shown here) suggesting thus, that this phenomenon is not an artifact of numerics but rather real expression of the physics.

If the speed is slightly increased to $V_\infty = 53.5$ m/s, the same pattern is observed, however now the oscillation observed within the ascending motion increases its amplitude. It is natural then to repeat this process for higher speeds and observe what happens. A speed of $V_\infty = 59$ m/s is considered, and the response is depicted in Fig. 32. The response does not show any aeroelastic instability, although the speed is increased from the previous cases showing LCOs. This result is unexpected and underlines, once again, the difficulties inherent to the design of such a configuration. With the aid of Fig. 33 this property is shown: starting from a stable situation, the speed is slowly decreased until a critical condition is reached. It can be appreciated that, for $V_\infty = 57$ the response immediately loses its stability (in the static sense) and an LCO is developed after the transient.

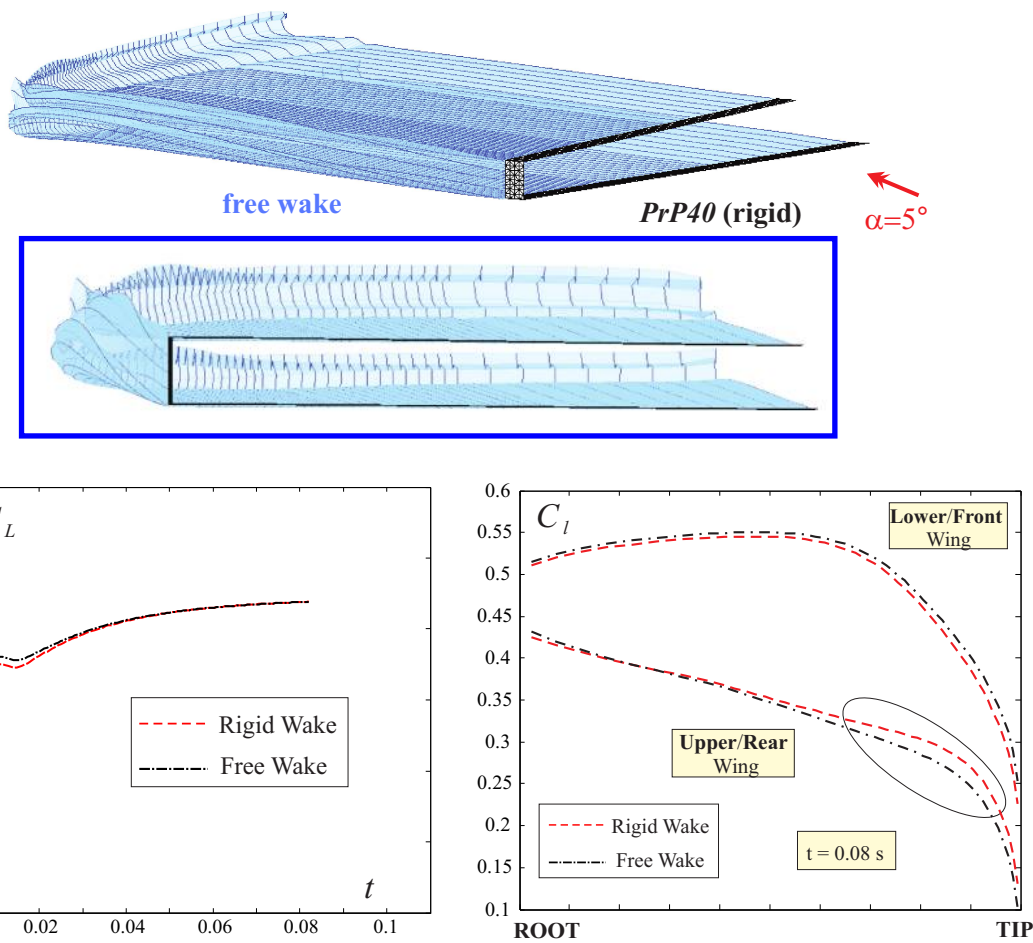


Fig. 29. Wake models and their effects on the lift coefficients of the PrP40's wings.

2. Solver2

Use of *Solver2* does not seem to give large differences from what previously observed. What can be noticed is a small decrease of the frequency, as shown in Fig. 34 when compared with the previous results. Also the same oscillating pattern during the ascending motion is observed. In order to better visualize this phenomenon, it is interesting to plot the *snapshots* of the configuration during a period, Fig. 35. As it can be easily verified, the states *c*, *d* and *e* describe the small oscillation during the ascending motion. Focusing then on the upper wing, it can be observed a unique smooth wave-like pattern identified by a compression and an extension, whereas for the outer portion of the wing this does not hold. It is not trivial to understand why the portions of the wing system have different dynamics, since different sources of difficulties are present: nonlinear structure, coupled aerodynamic structural and inertial effects, and also overconstrained nature of the system. As it will be shown in the next section, adding a further source of nonlinearity (wake roll up) also influences the above mentioned pattern.

3. Solver3

Results obtained with *Solver3* are presented in Fig. 36. The speed is selected so that it was possible to observe the small oscillation pattern of the tip of the wing (point P_1). The angle of attack is increased until the value of 3° is obtained. It is interesting to observe that the high frequency oscillation pattern earlier observed is now present in the descending portion of the LCO. To visualize this pattern, *snapshots* of the

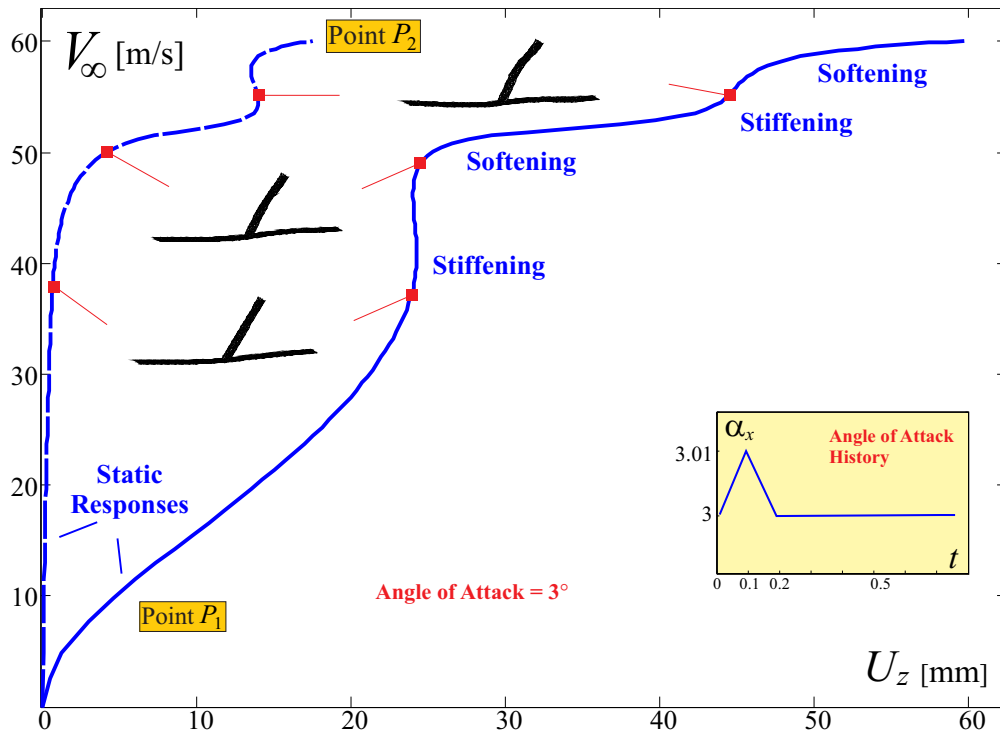


Fig. 30. Aeroelastic static response of *Sensorcraft*. Vertical displacements of points P_1 and P_2 are taken into consideration (see Fig. 13). Angle of attack is 3° . The vanishing perturbation that is applied to track the dynamic response is also represented.

configuration during a period are presented in Fig. 37. States f , g and h describe the small oscillation during the descending motion. It can be verified how, even if the midspan point P_2 is monotonically descending in this window of time, the outer portion of the wing inverts its motion bending upward before restarting its descend.

4. Effects of Solver's Choice and Structural Damping on Flutter Speed

In Fig. 38, it is plotted the flutter speed, as evaluated with the different solvers, with respect to the structural damping ratio. The predictions are now much closer, and the differences are negligible. This is related both to the particular layout and to the smaller deformations involved, which do not enhance the modelling differences of the solvers.

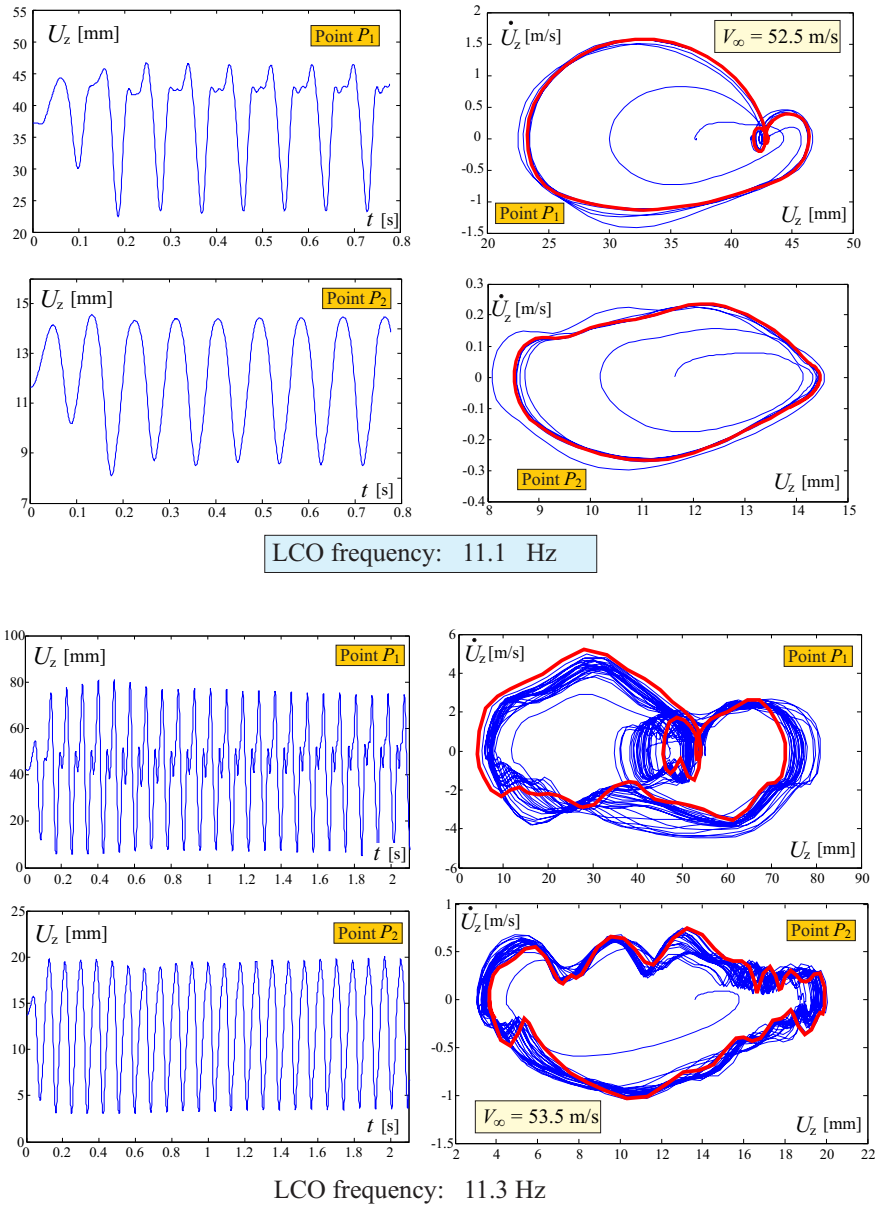


Fig. 31. Time response and Phase-space trajectory for *Sensorcraft* configuration, for different flow speeds. *Solver1* is employed. No structural damping is considered. Vertical displacements of both points P_1 and P_2 are considered (see Fig. 13).

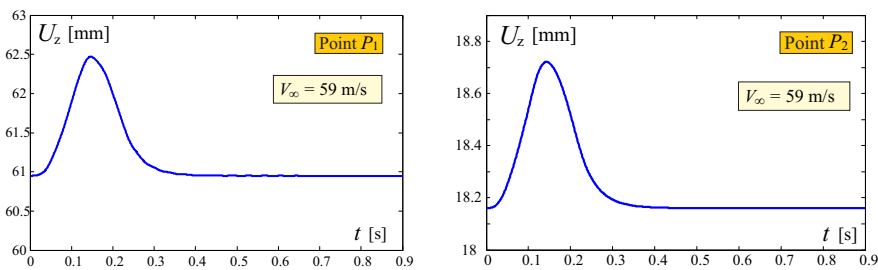


Fig. 32. Time response for *Sensorcraft* configuration, for $V_\infty = 59$ m/s. *Solver1* is employed. No structural damping is considered. Vertical displacements of both points P_1 and P_2 are considered (see Fig. 13).

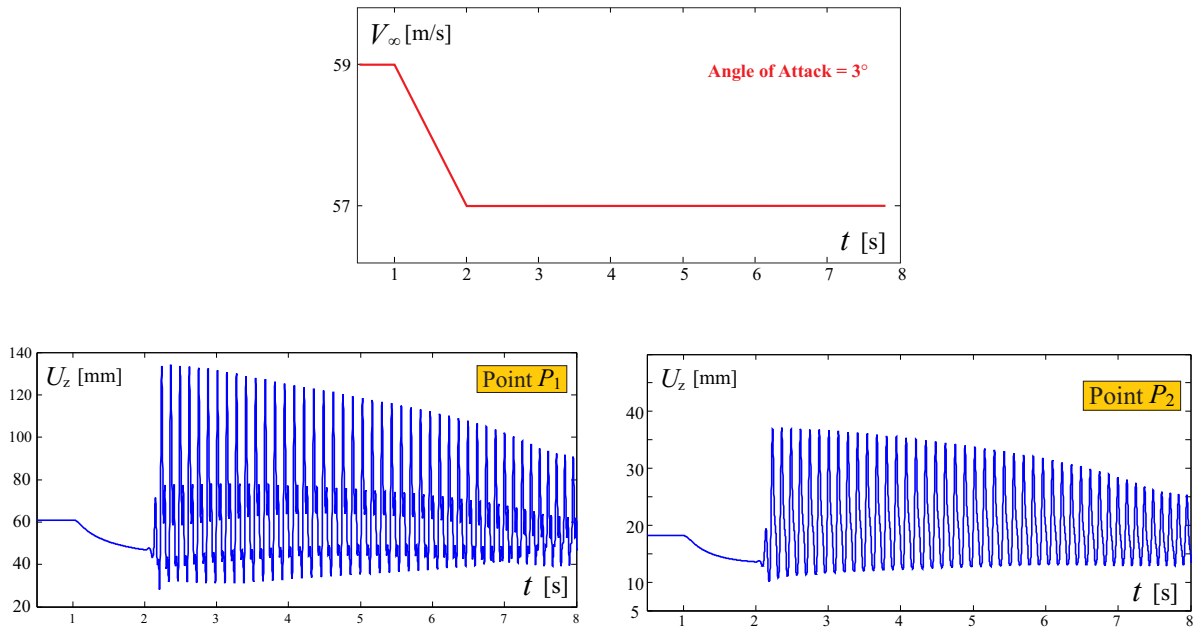


Fig. 33. Time response for *Sensorcraft* configuration, when the speed is decreased from $V_\infty = 59$ m/s to $V_\infty = 57$ m/s, and the angle of attack is maintained to 3° . *Solver1* is employed. No structural damping is considered. Vertical displacements of both points P_1 and P_2 are considered (see Fig. 13).

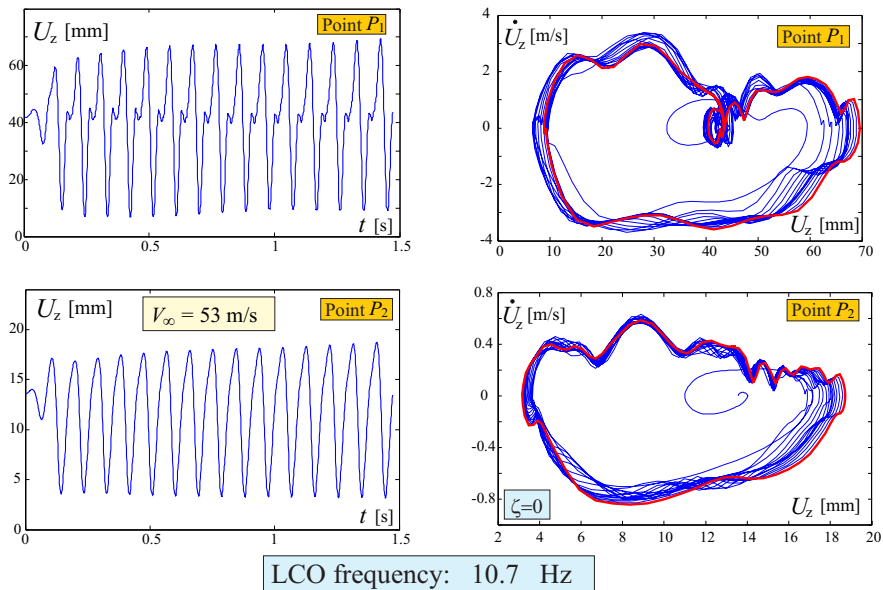


Fig. 34. Time response and Phase-space trajectory for *Sensorcraft* configuration at a speed $V_\infty = 53$ m/s. *Solver2* is employed. Vertical displacements of both points P_1 and P_2 are considered (see Fig. 13).

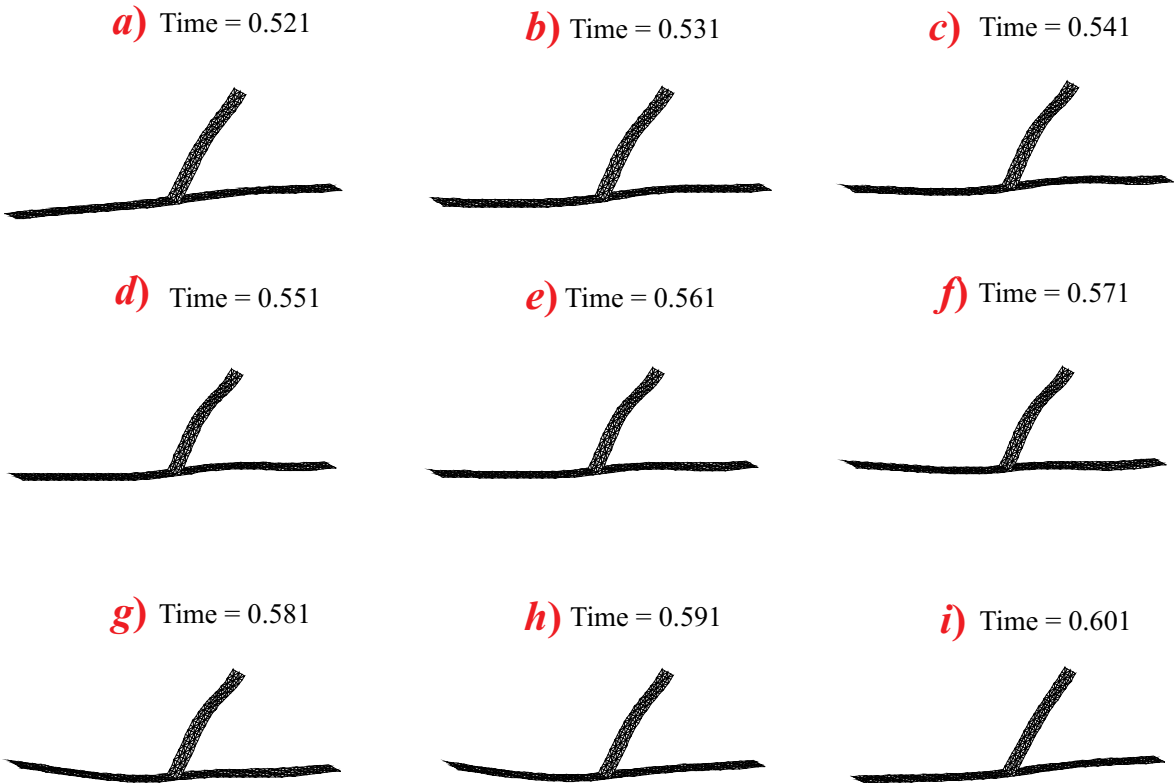
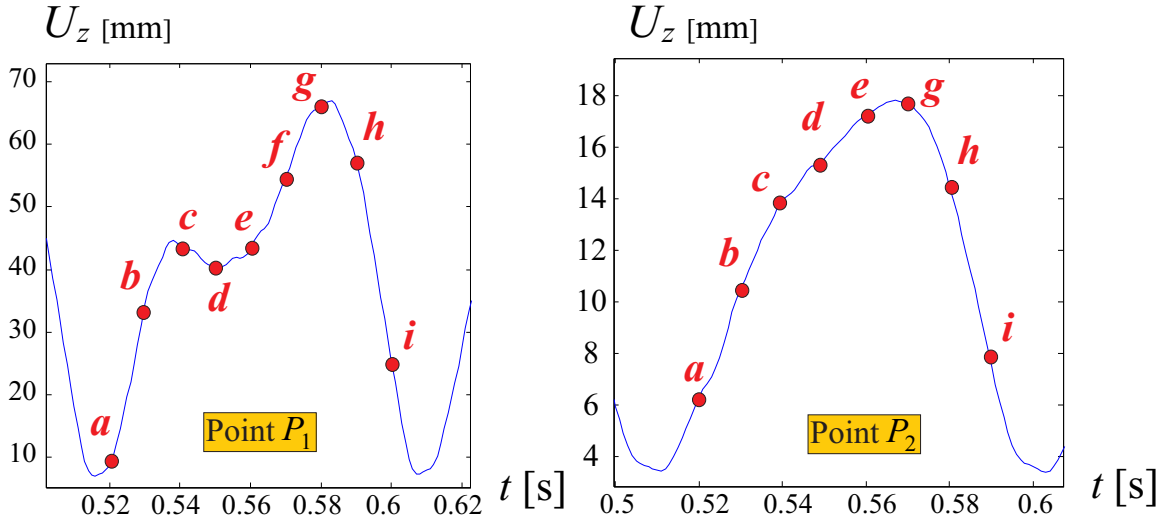


Fig. 35. Sequence of snapshots of the deformed configuration during one period (LCO). *Solver2* is employed and $V_\infty = 53$ m/s. The points c , d and e represent the small oscillation in the ascending motion.

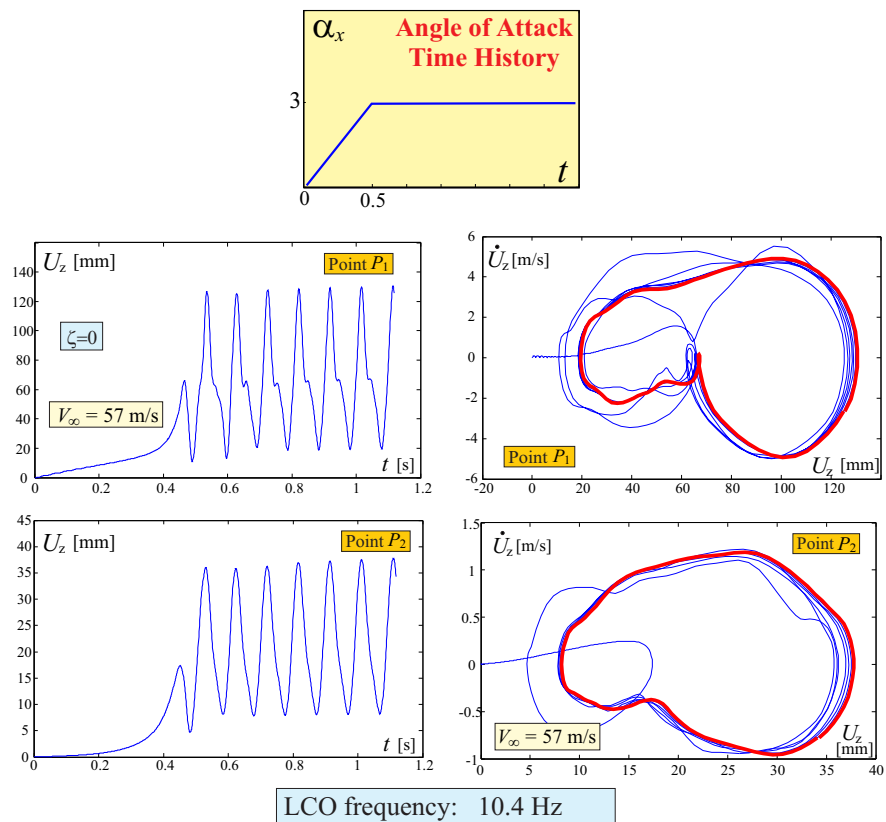


Fig. 36. Time response and Phase-space trajectory for *Sensorcraft* configuration, for $V_\infty = 57$ m/s. *Solver3* is employed. Vertical displacements of both points P_1 and P_2 are considered (see Fig. 13).

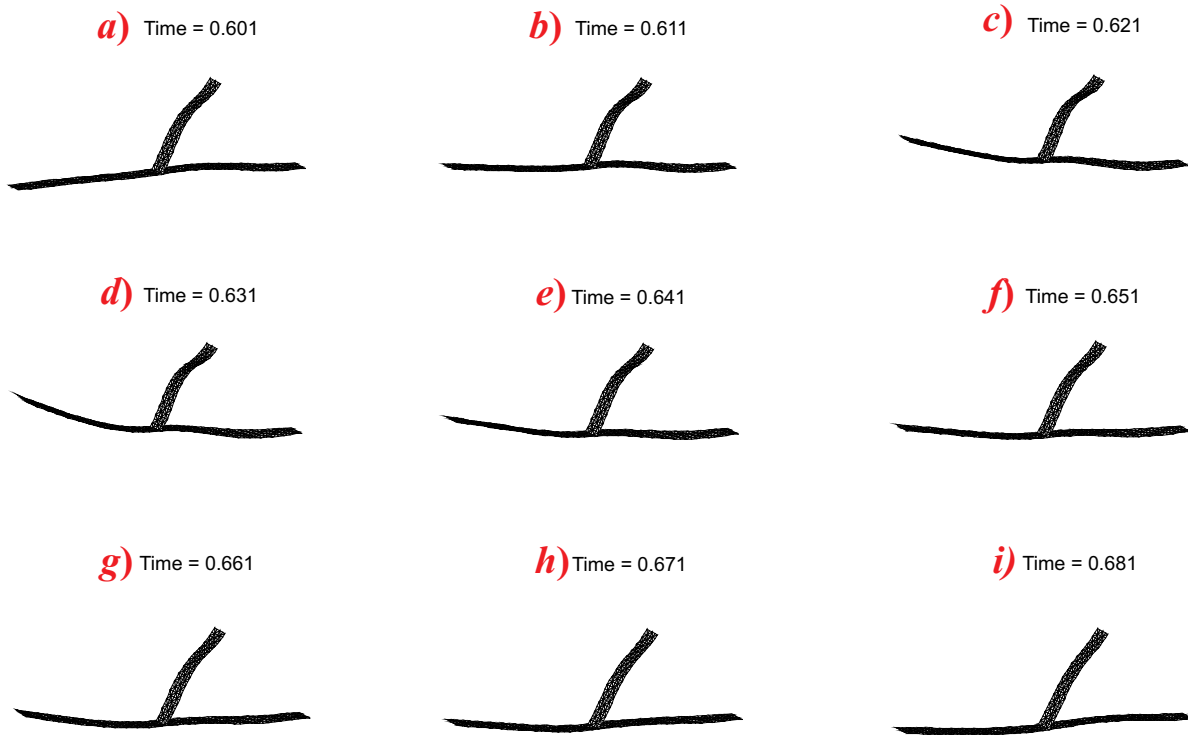
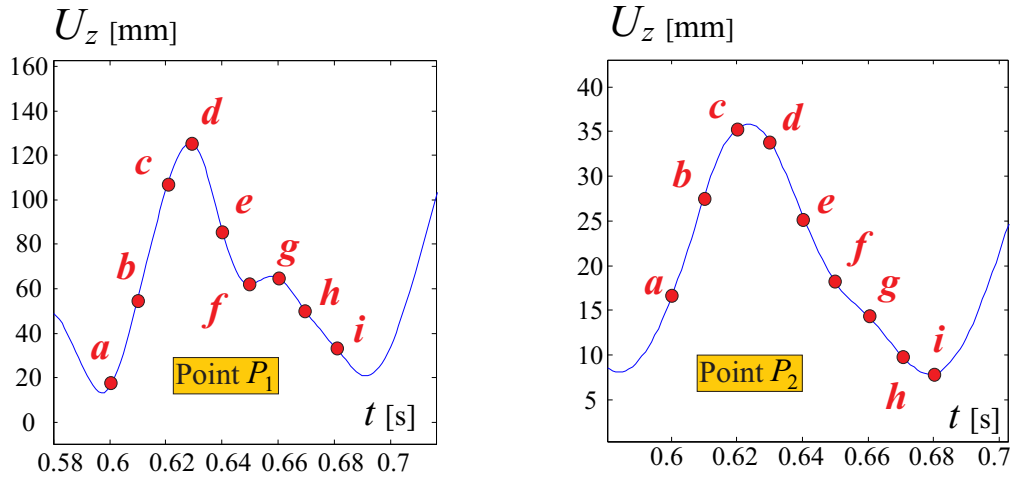


Fig. 37. Sequence of snapshots of the deformed configuration during one period (LCO). *Solver3* is employed and $V_\infty = 57$ m/s. The points *f*, *g* and *h* represent the small oscillation in the descending motion.

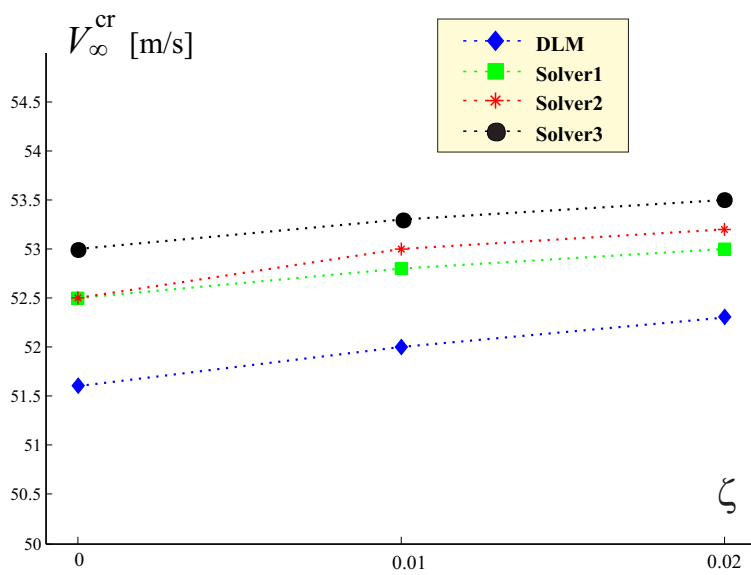


Fig. 38. Flutter speeds for *Sensorcraft* configuration, evaluated with the different solvers and for different structural damping ratio values.

IX. Joined Wings: a Dynamical System Perspective

This section shows the complicated picture of Joined Wings responses described from a dynamical system perspective. Different kinds of bifurcations are detected when tracing the *stability diagram*, and the situation appears very complex.

Before further going into details, the test case is here described. Consider the *PrP40* layout, shown in Fig. 12. The thickness is now selected to be 0.6 mm. The freestream velocity is along the x axis. *Solver1* is used to study the dynamic response. As it will be clear in the following, also aeroelastic static tool with continuation capabilities (arc-length methods) are used.

Being the angle of attack zero, there are no aerodynamic forces in the undeformed (basic) configuration. Thus, it is an equilibrium (fixed point) configuration for all velocities. With reference to the bifurcation diagram of Fig. 39, in which the vertical displacement of the tip of the lower wing (point P_1 in Fig. 12) has been chosen as representative displacement variable and the parameter is the flow speed, these fixed points lie on the ordinate. If the speed is increased, V^{sd} is reached. This speed is associated with saddle

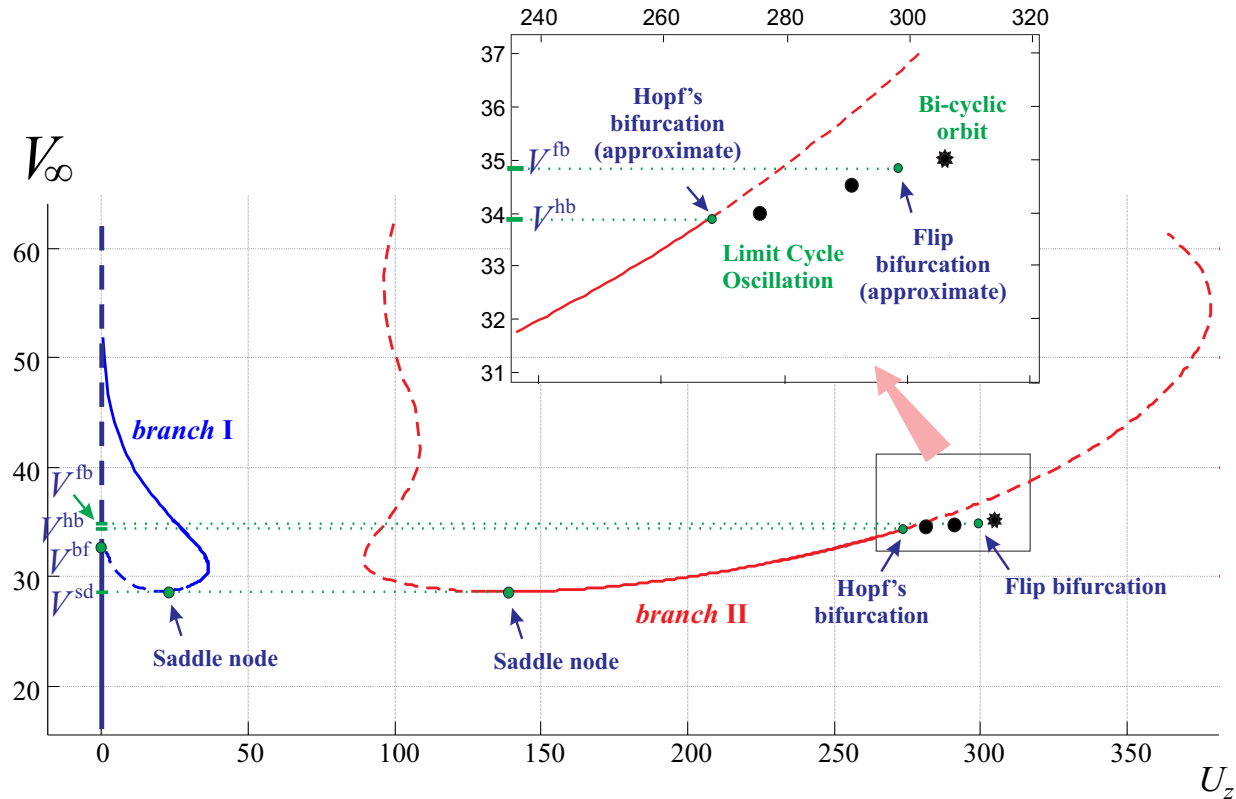


Fig. 39. Bifurcation diagram for the test case. *Solver1* is employed. Solid(dashed) lines represent stable (unstable) fixed points, full circles stand for stable limit cycle oscillations (the largest value is depicted) and the full complex star stand for stable bi-cyclic periodic closed orbit (largest value is depicted in the graph).

node bifurcations occurring on branches far from the fundamental one. What occurs is the inception of two fixed node points on each of the non-fundamental branches. That is, if the speed falls between V^{sd} and V^{bf} , there are *five possible equilibrium configurations*, and three of them are *stable*, see Fig. 39. Thus, a so called *tri-stability* situation is in place. With aid of Fig. 40, a speed in this range has been chosen, i.e. $V_\infty = 29.5$ m/s, and the equilibrium points are represented with a small circles, full (empty) if they are stable (unstable). Consequence of multi-stability have been already explored and discussed for joined-wing layouts in references [11, 12]. This property is demonstrated in Fig. 41 by giving different vanishing perturbations in angle of attack, and observing that after the transient the configuration could settle to the three different equilibrium states on the branches. When speed approaches V^{bf} , there is a bifurcation that leads to change of stability of the main branch: the undeformed configuration loses its stability. What happens in the negative part of U_z is here not studied, thus, any fixed point that may exist in that part of the plane has not been taken into consideration. The typical phase-space diagram for $V_\infty = 33.7$ m/s, which is in the

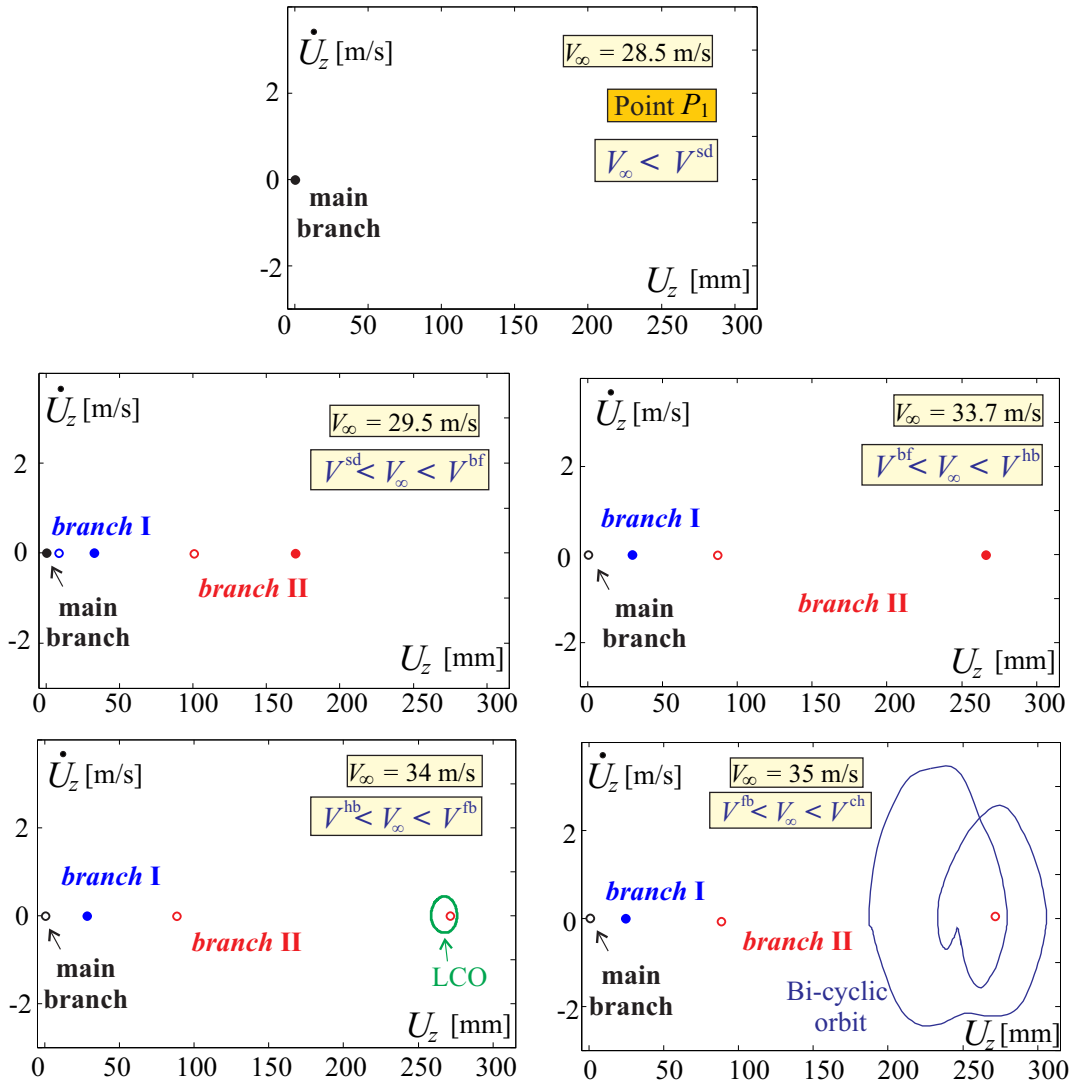


Fig. 40. Phase space for different speeds.

range $V^{bf} \div V^{hb}$ is depicted in Fig. 40. There is a bi-stability, being the stable states on the branch I and II. There are also two unstable poles, the first being on the undeformed configuration and the other one on the branch II. Responses showing this behaviour are represented in Fig. 42.

Increasing the speed, it is finally found an Hopf's bifurcation, V^{hb} . This bifurcation pertains the branch II only. The fixed static solution becomes unstable, and, on the contrary, a stable limit cycle oscillation is developed. The properties of the points on the other branches do not change. Thus, as it is shown for a speed $V_\infty = 34.0$ m/s, which is in the range $V^{hb} \div V^{fb}$, perturbations lead to the response shown in Fig. 43.

The largest bifurcation speed found in this analysis is V^{fb} , for which a flip bifurcation (also called period doubling) occurs. For speeds slightly larger than V^{fb} , then, considering that the only stable point lies on the branch I, there is still a bi-stability. This is shown also in Fig. 44. It is important to notice that, to mathematical assess a flip-bifurcation occurrence the eigenvalues of the so called *Monodromy Matrix* (known also as Floquet characteristic multipliers) [17, 87] have to be studied. However, this analysis is not trivial when relatively large (in terms of number of DOFs) systems are considered. Thus, this was not pursued in this study. On the contrary, period doubling was assessed noticing that, immediately after the bifurcation point, the period of the closed orbit was doubling compared to the one of the limit cycle oscillation established at a speed lower than the period doubling one. Fig. 45 clearly shows the doubling of the period. The closer orbit described after period doubling occurrence is here assessed to as bi-cyclic periodic orbit. It is presented

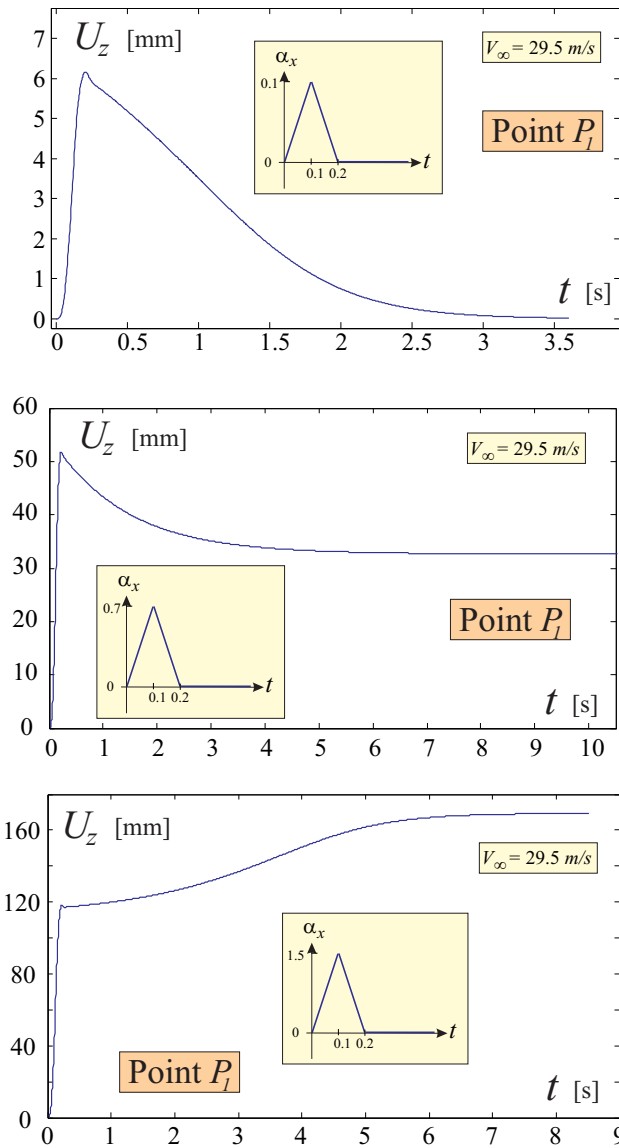


Fig. 41. Tri-stability region, at $V_\infty = 29.5$ m/s. Starting from the initial undeformed configuration different vanishing perturbations in angle attack are given, and the response is tracked.

more in detail in Fig. 45. The time responses as well as the state spaces are plotted considering now three degrees of freedom. Other than the point P_1 , now also vertical displacements of points P_2 and P_3 , shown in Fig. 12, are considered.

When speed is further increased, the response associated with the branch detached from the period doubling bifurcation seems to have a chaotic response, as shown in Fig. 46. In depth analyses are needed to confirm transition to chaos. The branch I stable fixed point is still present (Fig. 39).

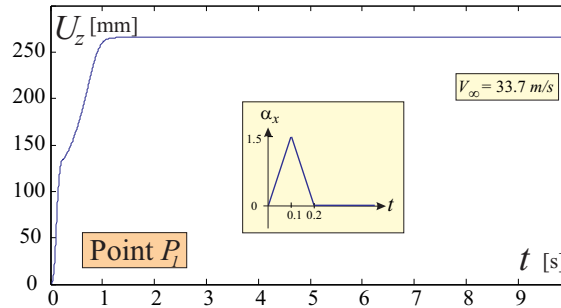
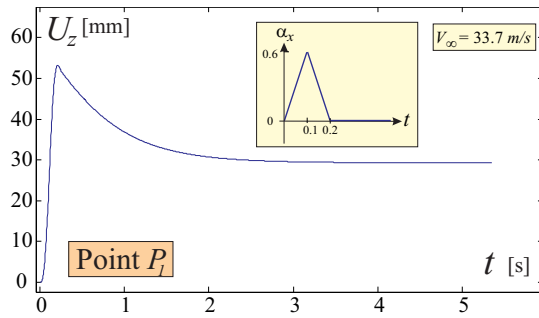


Fig. 42. Bi-stability region, at $V_\infty = 33.7$ m/s. Starting from the initial undeformed configuration different vanishing perturbations in angle attack are given, and the response is tracked. The systems could settle down to both static equilibrium on branches I and II.

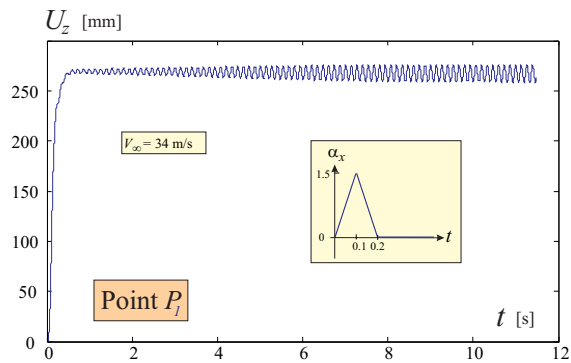
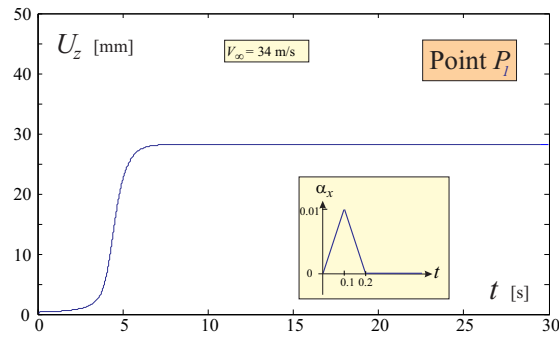


Fig. 43. Bi-stability region. Starting from the initial undeformed configuration different vanishing perturbations in angle attack are given, and the response is tracked. Either the static solution on branch I or the limit cycle oscillation are approached after a transient.

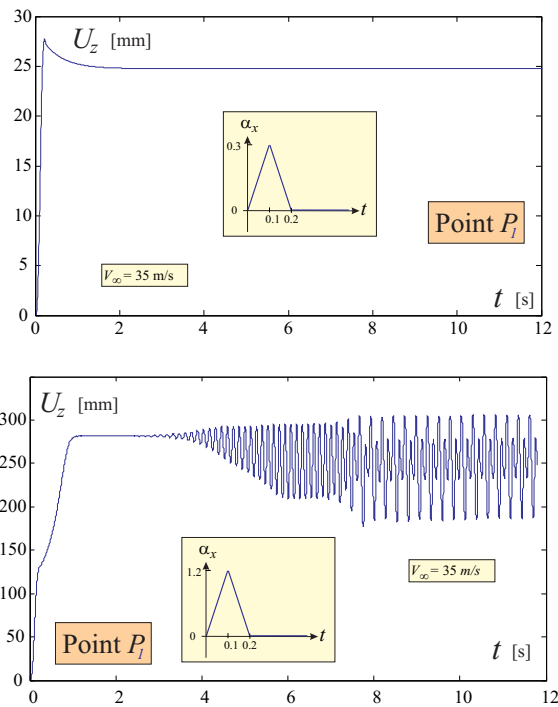


Fig. 44. Bi-stability region. Starting from the initial undeformed configuration different vanishing perturbations in angle attack are given, and the response is tracked. Either the static solution on branch I or the bi-cyclical closed orbit are approached after a transient.

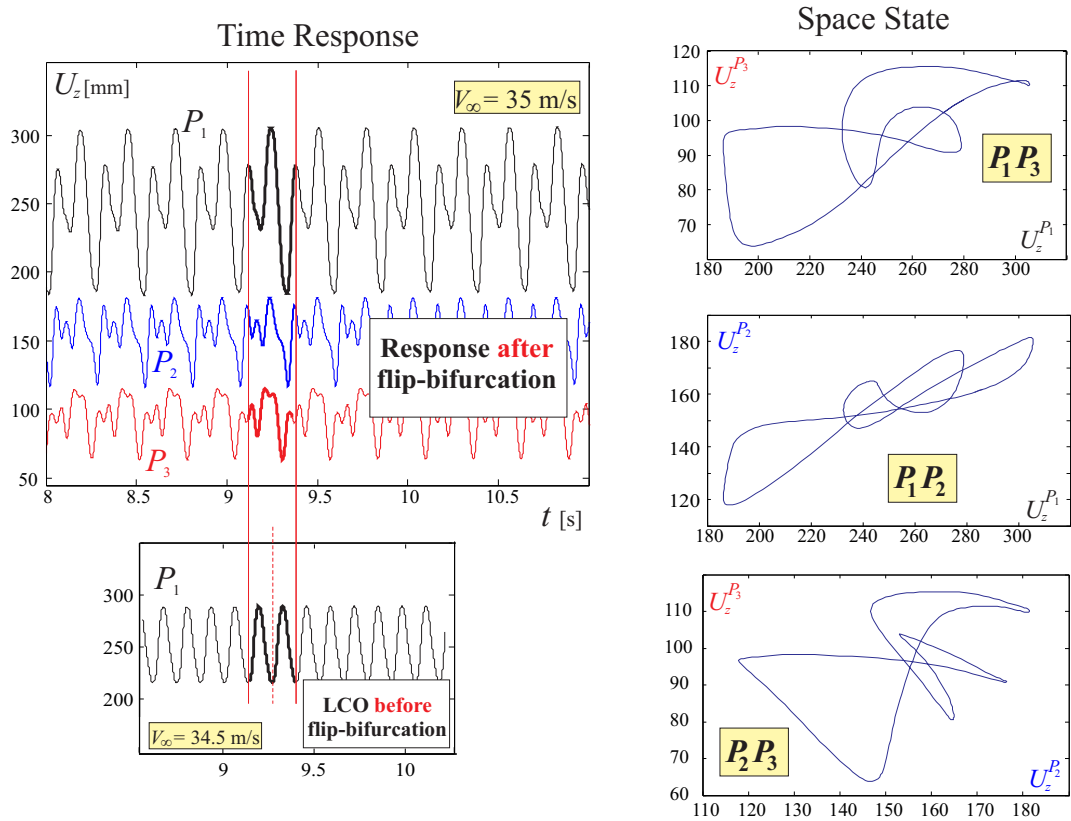


Fig. 45. Closed orbit for higher than flip bifurcation speeds. Time response for points P_1 , P_2 , P_3 , and state spaces for their combinations. The time responses are also compared to a subcritical one to assess the doubling of the period.

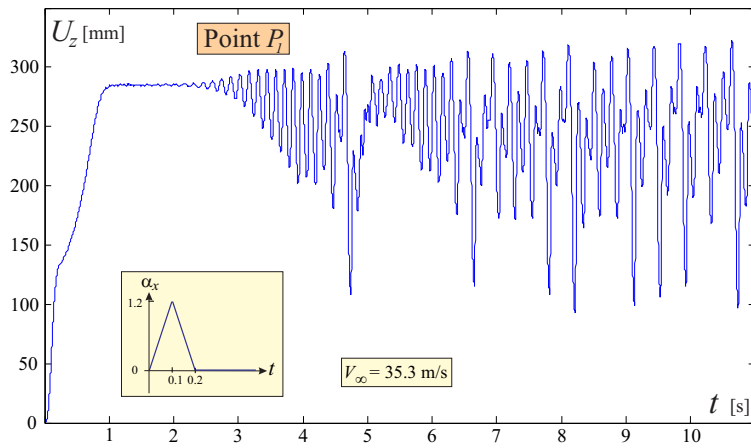


Fig. 46. Time response for $V_\infty = 35.3$ m/s when a vanishing perturbation in angle attack is given: the response does not show any periodicity.

X. Conclusions

Aeroelastic dynamic phenomena of Joined Wings have been here presented. Previous efforts assessed Joined Wings response for mechanical loads and post-critical conditions in static [4,11,16], and dynamic [13] regimes. The true aeroelastic post-critical condition was also studied. As a logical continuation this paper analyzed the aeroelastic dynamic response. The effort was directed towards different perspectives.

First, a dynamic characterization of the *snap-divergence* concept was achieved. In fact, its occurrence was first found in reference [13], and examined by means of an aeroelastic static analysis. The question was then to assess its existence and the behaviour of the system. Results showed that the static predictions were correct, and the characteristic *snap* was observed.

Second, flutter analysis undergone with a linear frequency-domain tool was compared to a nonlinear one, obtained as a sequence of linearizations performed about deformed configurations. These investigations continued what previously assessed in efforts [4,13] for mechanical instability and divergence. It was found that the linear tools were giving nonconservative predictions.

Third, the impact of different modelling of the aeroelastic problem (as the interface method or as the wake description) on flutter speed was assessed for time-domain solvers. Comparisons with the above frequency-domain capability were also given. It was shown that, free-wake modelling was increasing flutter speed (at least for the configurations under examination), and this was put in relation with the particular architecture of the layout. Other differences in the prediction were not enough clear to be assessed.

Fourth, aeroelastic dynamic post-critical regime was explored. Limit cycle oscillations were found. For some combinations of solvers and configurations, the transient to the LCO showed unusual trends: phase-space transient trajectories were not resembling the final periodic orbit and the transient time was relatively long. It was however difficult to give any further physical interpretation without having the support of experimental data. Moreover, for the Sensorcraft-like configuration, at certain speeds, the limit cycle oscillation was showing within a period different patterns between the outer and inner parts of the wing system.

Fifth, the joined-wing behaviour was studied in more depth on a dynamical system perspective. Bi-stability and tri-stability were observed, in analogy with what discovered in reference [11]. For a certain speed, one branch was experiencing an Hopf's bifurcation (flutter), followed by a flip bifurcation (or period doubling). These are common symptoms predicting transition to chaos.

A contribution that this paper aims to give is also represented by the detailed treatise of theory of implementation of the aeroelastic solvers. This has been accomplished describing problems inherent to the time-discretization of the dynamic equation. Moreover, the aeroelastic coupling is presented in detail, with emphasis on the different contributions giving raise to the aerodynamic unsteady forces. And, finally, application and specialization of the meshless method was tackled in depth.

XI. Acknowledgements

The authors acknowledges the support by San Diego State University (College of Engineering). They also like to warmly thank Professor Antonio Palacios of the Department of Mathematics of San Diego State University for his precious suggestions about nonlinear dynamics.

A. Meshless Interface Algorithm

The procedure of constructing shape functions using MLS approximation and the way to apply them in order to obtain the coupling between aerodynamic and structural field with the desired properties is here presented. The values of the function $\hat{u}(\mathbf{x})$ on a set of nodes $\{\boldsymbol{\eta}_1, \boldsymbol{\eta}_2, \dots, \boldsymbol{\eta}_{\hat{n}}\}$ are obtained from its values $\hat{u}(\boldsymbol{\xi}_1), \hat{u}(\boldsymbol{\xi}_2), \dots, \hat{u}(\boldsymbol{\xi}_{\hat{n}})$ on scattered centers (or sources) $\{\boldsymbol{\xi}_1, \boldsymbol{\xi}_2, \dots, \boldsymbol{\xi}_{\hat{n}}\}$ without deriving an analytical expression. This extrapolation is denoted by $\hat{u}^h(\boldsymbol{\eta})$ and is built as a sum of \hat{m} basis functions $\hat{p}_i(\boldsymbol{\eta})$

$$\hat{u}^h(\boldsymbol{\eta}) = \sum_{i=1}^{\hat{m}} \hat{p}_i(\boldsymbol{\eta}) a_i \boldsymbol{\xi}_i(\boldsymbol{\eta}) = \hat{\mathbf{p}}(\boldsymbol{\eta}) \cdot \mathbf{a} \boldsymbol{\xi}(\boldsymbol{\eta}) \quad (76)$$

where a_i are the unknown coefficients of the basis functions which depend on the point $\boldsymbol{\eta}$ where the value is sought; the vector $\hat{\mathbf{p}}$ of basis functions consists often of monomials of the lowest order such to form polynomial basis with minimum completeness but particular functions can be added to reproduce a particular behaviour of the variables investigated. In the present study linear and quadratic polynomials are adopted:

$$\begin{aligned} \hat{\mathbf{p}} &= \{1, x, y, z\} \\ \hat{\mathbf{p}} &= \{1, x, y, z, x^2, xy, y^2, yz, z^2, zx\} \end{aligned} \quad (77)$$

The \hat{m} coefficients a_i describing (as shown in eq.(76)) the function in the point $\boldsymbol{\eta}$ are obtained minimizing the weighted residual functional (a weighted discrete L_2 norm) $J(\boldsymbol{\eta})$

$$J(\boldsymbol{\eta}) = \sum_{i=1}^{\hat{n}} W(\boldsymbol{\eta} - \boldsymbol{\xi}_i) [\tilde{u}(\boldsymbol{\xi}_i, \boldsymbol{\eta}) - \hat{u}(\boldsymbol{\xi}_i)]^2 \quad (78)$$

where

$$\tilde{u}(\boldsymbol{\xi}_i, \boldsymbol{\eta}) = \hat{\mathbf{p}}(\boldsymbol{\xi}_i) \cdot \mathbf{a}(\boldsymbol{\eta}) \quad (79)$$

is the approximated value of the the field function in the generical center of the set $\boldsymbol{\xi}$ obtained by means of the same extrapolation process pointed out in eq.(76). A useful matrix form of eq.(78) can be given as follow:

$$J(\boldsymbol{\eta}) = (\hat{\mathbf{P}} \mathbf{a}(\boldsymbol{\eta}) - \hat{\mathbf{u}}) \cdot (\mathbf{W} (\hat{\mathbf{P}} \mathbf{a}(\boldsymbol{\eta}) - \hat{\mathbf{u}})) \quad (80)$$

where the following vectors and matrices are introduced:

$$\hat{\mathbf{u}} = \{\hat{u}(\boldsymbol{\xi}_1), \hat{u}(\boldsymbol{\xi}_2), \dots, \hat{u}(\boldsymbol{\xi}_{\hat{n}})\}$$

$$\hat{\mathbf{P}} = \begin{bmatrix} \hat{p}_1(\boldsymbol{\xi}_1) & \hat{p}_2(\boldsymbol{\xi}_1) & \dots & \hat{p}_{\hat{m}}(\boldsymbol{\xi}_1) \\ \hat{p}_1(\boldsymbol{\xi}_2) & \hat{p}_2(\boldsymbol{\xi}_2) & \dots & \hat{p}_{\hat{m}}(\boldsymbol{\xi}_2) \\ \dots & \dots & \dots & \dots \\ \hat{p}_1(\boldsymbol{\xi}_{\hat{n}}) & \hat{p}_2(\boldsymbol{\xi}_{\hat{n}}) & \dots & \hat{p}_{\hat{m}}(\boldsymbol{\xi}_{\hat{n}}) \end{bmatrix} \quad (81)$$

$$\mathbf{W} = \begin{bmatrix} W(\boldsymbol{\eta} - \boldsymbol{\xi}_1) & 0 & \dots & 0 \\ 0 & W(\boldsymbol{\eta} - \boldsymbol{\xi}_2) & \dots & 0 \\ \dots & \dots & \dots & \dots \\ 0 & 0 & \dots & W(\boldsymbol{\eta} - \boldsymbol{\xi}_{\hat{n}}) \end{bmatrix} \quad (82)$$

Solving the minimization problem

$$\frac{\partial J(\boldsymbol{\eta})}{\partial \mathbf{a}} = \mathbf{0} \quad (83)$$

an expression for the coefficient vector $\mathbf{a}(\boldsymbol{\eta})$ is obtained

$$\mathbf{a}(\boldsymbol{\eta}) = \hat{\mathbf{A}}^{-1} \hat{\mathbf{B}} \hat{\mathbf{u}} \quad (84)$$

where $\hat{\mathbf{A}}$ is called the *moment matrix* and is given by

$$\hat{\mathbf{A}} = \hat{\mathbf{P}}^T \mathbf{W} \hat{\mathbf{P}} \quad (85)$$

and $\hat{\mathbf{B}}$ is given by

$$\hat{\mathbf{B}} = \hat{\mathbf{P}}^T \mathbf{W} \quad (86)$$

It is now possible to give a definitive expression of eq.(76) as:

$$\hat{\mathbf{u}}^h(\boldsymbol{\eta}) = \sum_{i=1}^{\hat{n}} \Phi_i(\boldsymbol{\eta}) \hat{u}_i \quad (87)$$

where $\Phi_i(\boldsymbol{\eta})$ is the coefficient of the MLS shape function of node $\boldsymbol{\eta}$ corresponding to the center i , which is given by

$$\Phi_i(\boldsymbol{\eta}) = \sum_{j=1}^{\hat{m}} \hat{\rho}_j(\boldsymbol{\eta}) \left[\hat{\mathbf{A}}^{-1} \hat{\mathbf{B}} \right]_{ji} \quad (88)$$

Eq.(87) can also be written in the following matrix form, suitable for applications to the aeroelastic model

$$\hat{\mathbf{u}}^h(\boldsymbol{\eta}) = \boldsymbol{\Phi}(\boldsymbol{\eta}) \cdot \hat{\mathbf{u}} \quad (89)$$

where $\boldsymbol{\Phi}(\boldsymbol{\eta})$ is the array containing the coefficients of the MLS shape function of node $\boldsymbol{\eta}$.

The Radial Basis Functions (RBF) that can be adopted for the three-dimensional cases [73] are

$$\begin{aligned} W^0(r) &= (1-r)^2 & \mathcal{C}^0 \\ W^2(r) &= (1-r)^4(4r+1) & \mathcal{C}^2 \\ W^4(r) &= (1-r)^6\left(\frac{35}{3}r^2 + \frac{18}{3}r + 1\right) & \mathcal{C}^4 \\ W^6(r) &= (1-r)^8(32r^3 + 25r^2 + 8r + 1) & \mathcal{C}^6 \end{aligned} \quad (90)$$

where r represents the Euclidean distance between the two considered points. The degree of smoothness \mathcal{C}^n of the RBF bounds the maximum number of continuous derivatives of the approximant function $\hat{\mathbf{u}}^h$, as can be argued from the expression of the shape functions in eq.(88). Usually the weight functions in eq.(90) are written using as independent variable r/δ instead of r , where δ is a scaling factor that allows one to change the function support for different centers, making more appropriate the determination of the local support dimension in those cases where there is a great variation in the data density or when it is requested to exactly enforce structural constraints on the aerodynamic mesh.

The minimization problem has a unique solution if the symmetric matrix $\hat{\mathbf{A}}$ is positive definite; this matrix may become singular when the interface is not a well-posed problem, as for example when the number of terms of polynomial basis m is bigger than the number \hat{n} of nodes used in the support domain or when nodes and relative centers are such that the basis functions vanish in the local support. Especially the latter case can often represent an issue if, for example, planar or piecewise planar configurations are analyzed and it is thus useful to resort to the concept of Moore-Penrose pseudoinverse for evaluation of \mathbf{a} in eq.(84). The so-called Moore-Penrose pseudoinverse of matrices [88] is a concept that generalizes the usual notion of inverse of a square matrix, but that is also applicable to singular square matrices or even to non-square matrices. For this reason it proved to be particularly useful in dealing with certain least squares problems, when an approximation for solutions of linear equations like $\hat{\mathbf{A}}\mathbf{z} = \mathbf{c}$ is sought, where $\hat{\mathbf{A}}$ is a given $\hat{m} \times \hat{n}$ matrix and \mathbf{c} is a column vector with \hat{m} components; the solution is expressed as the set of all vectors \mathbf{z}^* such that the Euclidean norm $\|\hat{\mathbf{A}}\mathbf{z}^* - \mathbf{c}\|$ has the least possible value, called the minimizing set of the linear problem, and it can be demonstrated that this set is obtained through a matrix $\hat{\mathbf{A}}^+$, named the Moore-Penrose pseudoinverse of $\hat{\mathbf{A}}$ and satisfying the following properties:

$$\begin{aligned} \hat{\mathbf{A}}\hat{\mathbf{A}}^+\hat{\mathbf{A}} &= \hat{\mathbf{A}} \\ \hat{\mathbf{A}}^+\hat{\mathbf{A}}\hat{\mathbf{A}}^+ &= \hat{\mathbf{A}}^+ \\ \hat{\mathbf{A}}\hat{\mathbf{A}}^+ \text{ and } \hat{\mathbf{A}}^+\hat{\mathbf{A}} &\text{ are self-adjoint} \end{aligned} \quad (91)$$

For the Singular Value Decomposition Theorem [89] a matrix $\hat{\mathbf{A}}$ can always be written as

$$\hat{\mathbf{A}} = \mathbf{V}\mathbf{S}\mathbf{W}^* \quad (92)$$

where \mathbf{V} and \mathbf{W} are unitary matrices given by the *Polar Decomposition Theorem* and \mathbf{S} is a diagonal matrix whose diagonal elements are the singular values of $\hat{\mathbf{A}}$, i.e., the square root of the eigenvalues of $\hat{\mathbf{A}}^T \hat{\mathbf{A}}$. Eq.(92) shows the so-called singular value decomposition of the matrix $\hat{\mathbf{A}}$. It can be demonstrated that the Moore-Penrose pseudoinverse is given by

$$\hat{\mathbf{A}}^+ = \mathbf{W} \mathbf{S}^+ \mathbf{V}^* \quad (93)$$

where \mathbf{S}^+ is a diagonal matrix whose diagonal elements are the reciprocal of the singular values of $\hat{\mathbf{A}}$. The crucial point is the choice of which diagonal elements have to be retained in \mathbf{S}^+ , because this is the way an inverse matrix of a singular one is given, i.e, just the *invertible* part is inverted. In the present effort, the following strategy is chosen: the singular values of $\hat{\mathbf{A}}$ are normalized dividing them by the maximum one and a cut off value is adopted such that all the smaller ones are replaced with 0 in \mathbf{S}^+ (where the reciprocal would be requested). It should be observed that when the matrix $\hat{\mathbf{A}}$ is singular, it has at least one of its singular values equal to zero and so a cut off of 0 could be enough, but it can happen that although $\hat{\mathbf{A}}$ is non singular from a mathematical point of view (no zero eigenvalues) it has a high condition number and eq.(93) without further modifications wouldn't be enough to obtain good results.

The final issue is the conservation of energy [68]. To present the problem and its solution in the most general way, the following coupling conditions are considered

$$\begin{aligned} \boldsymbol{\sigma}^s \mathbf{n} &= -p \mathbf{n} + \boldsymbol{\sigma}^f \mathbf{n} \\ \boldsymbol{\eta}^s &= \boldsymbol{\eta}^f \\ \dot{\boldsymbol{\eta}}^s &= \dot{\boldsymbol{\eta}}^f \quad \text{or} \quad \frac{\partial \dot{\boldsymbol{\eta}}^s}{\partial n} = \frac{\partial \dot{\boldsymbol{\eta}}^f}{\partial n} \end{aligned} \quad (94)$$

where $\boldsymbol{\eta}^s$ denotes the structural boundary position, $\boldsymbol{\eta}^f$ is the aerodynamic counterpart, p is the pressure, $\boldsymbol{\sigma}^s$ and $\boldsymbol{\sigma}^f$ are respectively the structure stress tensor and the fluid viscous stress tensor, and \mathbf{n} is the normal vector to either a newly defined virtual interface surface or the surface of the fluid. The first relation expresses the dynamic equilibrium between stresses on the two fields, whereas the others are kinematic compatibility conditions on displacement and speed; for the latter one, just the normal component can be used if an inviscid flows is considered (wall tangency condition). As these conditions are valid for continuous systems and the two fields are discretized to solve the problem, conservation properties have to be assured: the change of energy in the fluid-structure system need to be equal to the energy supplied by external forces. In the following it is demonstrated how this property can be retained enforcing the coupling conditions in a weak sense through the use of Virtual Work. Calling $\delta \boldsymbol{\eta}^f$ and $\delta \boldsymbol{\eta}^s$ the admissible displacements for the two respective fields, the relation between nodal quantities (i and j are respectively the generical aerodynamic and structural node) is

$$\delta \boldsymbol{\eta}_i^f = \sum_{j=1}^{j_s} \Phi_j(\boldsymbol{\eta}_i^f) \delta \boldsymbol{\eta}_j^s \quad (95)$$

where i^f and j^f are respectively the number of aerodynamic and structural nodes considered. The resulting virtual displacement of the aerodynamic surface Γ^f is obtained assuming N_i base functions belonging to the aerodynamic field discretization space corresponding to the i^f nodes of the same surface; in this way, the following relation holds

$$\delta \boldsymbol{\eta}^f = \sum_{i=1}^{i_f} N_i \sum_{j=1}^{j_s} \Phi_j(\boldsymbol{\eta}_i^f) \delta \boldsymbol{\eta}_j^s \quad (96)$$

The virtual work of the aerodynamic load is equal to

$$\delta W^f = \int_{\Gamma^f} (-p \mathbf{n} + \boldsymbol{\sigma}^f \mathbf{n}) \cdot \delta \boldsymbol{\eta}^f d\Gamma \quad (97)$$

Calling \mathbf{f}_j the load on the structural node j induced by the fluid, the virtual work of the forces acting on the structure is

$$\delta W^s = \sum_{j=1}^{j_s} \mathbf{f}_j \delta \boldsymbol{\eta}_j^s \quad (98)$$

Imposing equivalence of the virtual works and rearranging eq.(97) through eq.(95) and eq.(96) the following holds

$$\mathbf{f}_j = \sum_{i=1}^{i^f} \mathbf{F}_i \Phi_j(\boldsymbol{\eta}_i^f) \quad (99)$$

where \mathbf{F}_i is given by

$$\mathbf{F}_i = \int_{\Gamma^f} (-p \mathbf{n} + \boldsymbol{\sigma}^f \mathbf{n}) N_i d\Gamma \quad (100)$$

Consider now \mathbf{f} (\mathbf{F}) to be the matrix whose rows are the forces evaluated at the generic aerodynamic (structural) j -th (i -th) node, \mathbf{f}_j (\mathbf{F}_i). Thus eq.(99) may be written in the matrix form:

$$\mathbf{f} = \boldsymbol{\Psi}^T \mathbf{F} \quad (101)$$

being $\boldsymbol{\Psi}$ the interpolation matrix that matches the two displacement's fields, i.e., $\Psi_{ij} = \Phi_j(\boldsymbol{\eta}_i^f)$. Eq.(101) shows the sought result: to ensure the balance of the energy exchanged between fluid and structure, the loads on the structural nodes \mathbf{f} have to be evaluated multiplying the loads \mathbf{F} on the aerodynamic grid by the transpose of the interpolation matrix.

References

- ¹Wolkovitch, J., "The Joined Wing Aircraft: an Overview," *Journal of Aircraft*, Vol. 23, No. No. 3, March 1986, pp. 161–178.
- ²Frediani, A., Cipolla, V., and Rizzo, E., "The PrandtlPlane Configuration: Overview on Possible Applications to Civil Aviation," *Variational Analysis and Aerospace Engineering: Mathematical Challenges for Aerospace Design*, edited by G. Buttazzo and A. Frediani, Vol. 66 of *Springer Optimization and Its Applications*, Springer US, 2012, pp. 179–210, 10.1007/978-1-4614-2435-2-8.
- ³Blair, M., Canfield, R. A., and Roberts Jr., R. W., "Joined-Wing Aeroelastic Design with Geometric Nonlinearity," *Journal of Aircraft*, Vol. 42, No. No. 4, July 2005, pp. 832–848.
- ⁴Demasi, L., Cavallaro, R., and Razon, A., "Post-critical Analysis of PrandtlPlane Joined-Wing Configurations," *AIAA Journal*, Vol. 51, No. 1, 2013, pp. 161–177.
- ⁵Cavallaro, R., Demasi, L., and Passariello, A., "Nonlinear Analysis of PrandtlPlane Joined Wings - Part II: Effects of Anisotropy," No. AIAA 2012-1462, 53rd AIAA/ASME/ASCE/AHS/ASC Structures, Structural Dynamics, and Materials Conference, Honolulu, Hawaii, 23-26 April 2012.
- ⁶Chambers, J. R., *Innovation in Flight: Research of the NASA Langley Research Center on Revolutionary Advanced Concepts for Aeronautics*, No. 39 in Monograph in Aerospace History, NASA, November 2005, NASA SP 2005-4539.
- ⁷Demasi, L. and Livne, E., "The Structural Order Reduction Challenge in the Case of Geometrically Nonlinear Joined-Wing Configurations," 2007, Presented at the 48th AIAA/ASME/ASCE/AHS/ASC Structures, Structural Dynamics & Materials Conference, Honolulu, Hawaii, 23-26 April 2007.
- ⁸Demasi, L. and Palacios, A., "A Reduced Order Nonlinear Aeroelastic Analysis of Joined Wings Based on the Proper Orthogonal Decomposition," 2010, Presented at the 51st AIAA/ASME/ASCE/AHS/ASC Structures, Structural Dynamics & Materials Conference, Orlando, Florida, 12-15 April 2010.
- ⁹Tiso, P., Demasi, L., Teunisse, N., and Cavallaro, R., "A Computational Method for Structurally Nonlinear Joined Wings Based on Modal Derivatives," No. AIAA 2014-0494, 55th AIAA/ASMe/ASCE/AHS/SC Structures, Structural Dynamics, and Materials Conference, AIAA Science and Technology Forum and Exposition (SciTech2014) National Harbor, Maryland, American Institute of Aeronautics and Astronautics, 13-17 January 2014.
- ¹⁰Philipot, G., Wang, X., Mignolet, M., Demasi, L., and Cavallaro, R., "Reduced Order Modeling for the Nonlinear Geometric Response of Some Joined Wings," No. AIAA 2014-0151, 55th AIAA/ASMe/ASCE/AHS/SC Structures, Structural Dynamics, and Materials Conference, AIAA Science and Technology Forum and Exposition (SciTech2014) National Harbor, Maryland, American Institute of Aeronautics and Astronautics, 13-17 January 2014.
- ¹¹Cavallaro, R., Demasi, L., and Bertucelli, F., "Risks of Linear Design of Joined Wings: a Nonlinear Dynamic Perspective in the Presence of Follower Forces," No. AIAA 2013-1558, 54rd AIAA/ASME/ASCE/AHS/ASC Structures, Structural Dynamics, and Materials Conference, Boston, Massachusetts, American Institute of Aeronautics and Astronautics, 8-11 April 2013.
- ¹²Cavallaro, R., Demasi, L., Bertucelli, F., and Benson, D. J., "Risks of Linear Design of Joined Wings: a Nonlinear Dynamic Perspective in the Presence of Follower Forces," 2013, Submitted for Publication.
- ¹³Demasi, L., Cavallaro, R., and Bertucelli, F., "Post-Critical Analysis of Joined Wings: the Concept of Snap-Divergence as a Characterization of the Instability," No. AIAA 2013-1559, 54rd AIAA/ASME/ASCE/AHS/ASC Structures, Structural Dynamics, and Materials Conference, Boston, Massachusetts, American Institute of Aeronautics and Astronautics, 8-11 April 2013.
- ¹⁴Demasi, L. and Livne, E., "Contributions to Joined-Wing Aeroelasticity," 2009, Presented at the International Forum on Aeroelasticity and Structural Dynamics Conference, Seattle, Washington, 21-25 June 2009.
- ¹⁵Bhasin, S., Chen, P., Wan, Z., and Demasi, L., "Dynamic Nonlinear Aeroelastic Analysis of the Joined Wing Configuration," No. AIAA 2012-1791, 53rd AIAA/ASME/ASCE/AHS/ASC Structures, Structural Dynamics, and Materials Conference, Honolulu, Hawaii, 23-26 April 2012.
- ¹⁶Cavallaro, R., Demasi, L., and Passariello, A., "Nonlinear Analysis of PrandtlPlane Joined Wings: Effects of Anisotropy," *AIAA Journal*, 2014, In press.
- ¹⁷Seydel, R., *Practical Bifurcation and Stability Analysis*, Interdisciplinary Applied Mathematics, Springer, 2009.
- ¹⁸Dowell, E., Edwards, J., and Strganac, T., "Nonlinear Aeroelasticity," *Journal of Aircraft*, Vol. 40, No. 5, September 2003, pp. 857–874.
- ¹⁹Thompson, J. and Stewart, H., *Nonlinear Dynamics and Chaos: Geometrical Methods for Engineers and Scientists*, A Wiley-Interscience publication, Wiley, 1986.
- ²⁰Strogatz, S. H., *Nonlinear Dynamics And Chaos: With Applications To Physics, Biology, Chemistry, And Engineering (Studies in Nonlinearity)*, Studies in nonlinearity, Perseus Books Group, 1st ed., Jan. 1994.
- ²¹Gordnier, R. E. and Melville, R. B., "Numerical Simulation of Limit-cycle Oscillations of a Cropped Delta Wing Using the Full Navier-Stokes Equations," *International Journal of Computational Fluid Dynamics*, Vol. 14, No. 3, 2001, pp. 211–224.
- ²²Gordnier, R. E., "Computation of Limit-Cycle Oscillations of a Delta Wing," *Journal of Aircraft*, Vol. 40, No. 6, 2003, pp. 1206–1208.
- ²³Attar, P. and Gordnier, R., "Aeroelastic prediction of the limit cycle oscillations of a cropped delta wing," *Journal of Fluids and Structures*, Vol. 22, No. 1, 2006, pp. 45 – 58.
- ²⁴Harder, R. L. and Desmarais, R. N., "Interpolation using surface splines," *Journal of Aircraft*, Vol. 9, No. 2, 1972, pp. 189–191.
- ²⁵Liu, G., *Mesh Free Methods: Moving Beyond the Finite Element Method*, Taylor & Francis, 2010.
- ²⁶Lange, R. H., Cahill, J. F., Bradley, E. S., Eudaily, R. R., Jenness, C. M., and Macwilkinson, D. G., "Feasibility Study of the Transonic Biplane Concept for Transport Aircraft Applications," 1974, NASA CR–132462, Lockheed–Georgia Company.
- ²⁷Miranda, L. R., "Boxplane Wing and Aircraft," US Patent 3,834,654, September 1974.

- ²⁸Divoux, N. and Frediani, A., “The Lifting System of a PrandtlPlane, Part 2: Preliminary Study on Flutter Characteristics,” *Variational Analysis and Aerospace Engineering: Mathematical Challenges for Aerospace Design*, edited by G. Buttazzo and A. Frediani, Vol. 66 of *Springer Optimization and Its Applications*, Springer US, 2012, pp. 235–267, 10.1007/978-1-4614-2435-2_10.
- ²⁹DalCanto, D., Frediani, A., Ghiringhelli, G. L., and Terraneo, M., “The Lifting System of a PrandtlPlane, Part 1: Design and Analysis of a Light Alloy Structural Solution,” *Variational Analysis and Aerospace Engineering: Mathematical Challenges for Aerospace Design*, edited by G. Buttazzo and A. Frediani, Vol. 66 of *Springer Optimization and Its Applications*, Springer US, 2012, pp. 211–234, 10.1007/978-1-4614-2435-2_9.
- ³⁰Frediani, A., “Velivolo Biplano ad Ali Contrapposte,” 2003, Italian Patent FI 2003A000043, 19 February 2003.
- ³¹Frediani, A., “New Large Aircraft,” 2002, European Patent EP 0716978B1, 20 March 2002.
- ³²Frediani, A., “Large Dimension Aircraft,” 1999, US Patent 5,899,409, 1999.
- ³³Felippa, C. and Geers, T. L., “Partitioned analysis for coupled mechanical systems,” *Engineering Computations*, Vol. 5, No. 2, 1988, pp. 123 – 133.
- ³⁴Deparis, S., Discacciati, M., Fourestey, G., and Quarteroni, A., “Fluidstructure algorithms based on SteklovPoincaré operators,” *Computer Methods in Applied Mechanics and Engineering*, Vol. 195, No. 4143, 2006, pp. 5797 – 5812, John H. Argyris Memorial Issue. Part II.
- ³⁵Küttler, U. and Wall, W. A., “Fixed-point fluidstructure interaction solvers with dynamic relaxation,” *Computational Mechanics*, Vol. 43, 2008, pp. 61–72.
- ³⁶Rodden, W. P., Taylor, P. F., and McIntosh, S. C., “Further Refinement of the Subsonic Doublet-Lattice Method,” *Journal of Aircraft*, Vol. 35, No. 5, September 1998, pp. 720–727.
- ³⁷Demasi, L. and Livne, E., “Dynamic Aeroelasticity of Structurally Nonlinear Configurations Using Linear Modally Reduced Aerodynamic Generalized Forces,” *AIAA Journal*, Vol. 47, 2009, pp. 71–90.
- ³⁸Demasi, L. and Livne, E., “Aeroelastic coupling of geometrically nonlinear structures and linear unsteady aerodynamics: Two formulations,” *Journal of Fluids and Structures*, Vol. 25, No. 5, 2009, pp. 918 – 935.
- ³⁹Levy, R. and Gal, E., “Triangular Shell Element for Large Rotations Analysis,” *AIAA Journal*, Vol. 41, No. 12, December 2003, pp. 2505–2508.
- ⁴⁰Levy, R. and Spillers, W., *Analysis of geometrically nonlinear structures*, No. v. 1, Kluwer Academic Publishers, 2003.
- ⁴¹Gal, E. and Levy, R., “The Geometric Stiffness of Triangular Composite-Materials Shell Elements,” *Computers and Structures*, Vol. 83, 2005, pp. 2318–2333.
- ⁴²Gal, E., Levy, R., Abramovich, H., and Pavsner, P., “Buckling analysis of composite panels,” *Composite Structures*, Vol. 73, No. 2, 2006, pp. 179 – 185, International Conference on Buckling and Postbuckling Behavior of Composite Laminated Shell Structures.
- ⁴³Hughes, T. J. R., *The Finite Element Method: Linear Static and Dynamic Finite Element Analysis*, Prentice-Hall, 1987.
- ⁴⁴Crisfield, M., *Non Linear Finite Element Analysis of Solid and Structures*, Vol. 2, John Wiley & Sons, 1991.
- ⁴⁵Belytschko, T., Liu, W., and Moran, B., *Nonlinear finite elements for continua and structures*, Wiley, 2000.
- ⁴⁶Kuhl, D. and Ramm, E., “Generalized EnergyMomentum Method for non-linear adaptive shell dynamics,” *Computer Methods in Applied Mechanics and Engineering*, Vol. 178, No. 34, 1999, pp. 343 – 366.
- ⁴⁷Newmark, N. M., “A method of computation for structural dynamics,” *Journal of Engineering Mechanics, ASCE*, Vol. 85 (EM3), 1959, pp. 67–94.
- ⁴⁸Hughes, T. J., “Stability, convergence and growth and decay of energy of the average acceleration method in nonlinear structural dynamics,” *Computers & Structures*, Vol. 6, No. 45, 1976, pp. 313 – 324.
- ⁴⁹Chung, J. and Hulbert, G. M., “A Time Integration Algorithm for Structural Dynamics With Improved Numerical Dissipation: The Generalized-alpha Method,” *Journal of Applied Mechanics*, Vol. 60, No. 2, 1993, pp. 371–375.
- ⁵⁰Hilber, H. M., Hughes, T. J. R., and Taylor, R. L., “Improved numerical dissipation for time integration algorithms in structural dynamics,” *Earthquake Engineering & Structural Dynamics*, Vol. 5, No. 3, 1977, pp. 283–292.
- ⁵¹Wood, W. L., Bossak, M., and Zienkiewicz, O. C., “An alpha modification of Newmark’s method,” *International Journal for Numerical Methods in Engineering*, Vol. 15, No. 10, 1980, pp. 1562–1566.
- ⁵²Park, K. C., “An Improved Stiffly Stable Method for Direct Integration of Nonlinear Structural Dynamic Equations,” *Journal of Applied Mechanics*, Vol. 42, No. 2, 1975, pp. 464–470.
- ⁵³Hughes, T. J. R., “A note on the stability of Newmark’s algorithm in nonlinear structural dynamics,” *International Journal for Numerical Methods in Engineering*, Vol. 11, No. 2, 1977, pp. 383–386.
- ⁵⁴Wood, W. L. and Oduor, M. E., “Stability properties of some algorithms for the solution of nonlinear dynamic vibration equations,” *Communications in Applied Numerical Methods*, Vol. 4, No. 2, 1988, pp. 205–212.
- ⁵⁵Kuhl, D. and Crisfield, M. A., “Energy-conserving and decaying Algorithms in non-linear structural dynamics,” *International Journal for Numerical Methods in Engineering*, Vol. 45, No. 5, 1999, pp. 569–599.
- ⁵⁶Kuhl, D. and Ramm, E., “Constraint Energy Momentum Algorithm and its application to non-linear dynamics of shells,” *Computer Methods in Applied Mechanics and Engineering*, Vol. 136, No. 34, 1996, pp. 293 – 315.
- ⁵⁷Belytschko, T. and Schoeberle, D. F., “On the Unconditional Stability of an Implicit Algorithm for Nonlinear Structural Dynamics,” *Journal of Applied Mechanics*, Vol. 42, No. 4, 1975, pp. 865–869.
- ⁵⁸Simo, J. C. and Tarnow, N., “The discrete energy-momentum method. Conserving algorithms for nonlinear elastodynamics,” *Zeitschrift für Angewandte Mathematik und Physik (ZAMP)*, Vol. 43, 1992, pp. 757–792, 10.1007/BF00913408.
- ⁵⁹Dong, S., “BDF-like methods for nonlinear dynamic analysis,” *Journal of Computational Physics*, Vol. 229, No. 8, 2010, pp. 3019 – 3045.
- ⁶⁰Krenk, S., “Energy conservation in Newmark based time integration algorithms,” *Computer Methods in Applied Mechanics and Engineering*, Vol. 195, No. 4447, 2006, pp. 6110 – 6124.
- ⁶¹Ginsberg, J., *Mechanical and Structural Vibrations: Theory and Applications*, Wiley, 2001.

- ⁶²Katz, J. and Plotkin, A., *Low-Speed Aerodynamics*, Cambridge Aerospace Series, Cambridge University Press, 2001.
- ⁶³Leishman, J. G. and Bhagwat, M. J., “Generalized viscous vortex model for application to free-vortex wake and aeroacoustic calculations,” 58th Annual Forum and Technology Display of the American Helicopter Society International, Montreal, Canada, 11-13 June 2002.
- ⁶⁴Leishman, J. G., *Principles of helicopter aerodynamics*, Cambridge aerospace series, Cambridge University Press, Cambridge, New York, 2000.
- ⁶⁵Hess, J. and Smith, M., “Calculation of Potential Flows about Arbitrary Bodies,” 1967.
- ⁶⁶Smith, M. J., Hodges, D. H., and Cesnik, C. E. S., “An Evaluation of Computational Algorithms to Interface Between CFD and CSD Methodologies,” 1995.
- ⁶⁷Bathe, K. J., “Finite Element Procedures,” 1996, Prentice Hall, Englewood Cliffs, NJ, USA.
- ⁶⁸Quaranta, G., Masarati, P., and Mantegazza, P., “A conservative mesh-free approach for fluid structure problems in Coupled Problems,” *International Conference for Coupled Problems in Science and Engineering, Santorini, Greece, 23-29 May 2005*, pp. 24–27.
- ⁶⁹Cebral, J. R. and Lohner, R., “Conservative Load Projection and Tracking for Fluid-Structure Problems,” *AIAA Journal*, Vol. 35, No. 4, 1997, pp. 687–692.
- ⁷⁰Celniker, G. and Gossard, D., “Deformable Curve and Surface Finite-elements for Free-form Shape Design,” *SIGGRAPH Comput. Graph.*, Vol. 25, No. 4, July 1991, pp. 257–266.
- ⁷¹Lancaster, P. and Salkauskas, K., “Surfaces Generated by Moving Least Squares Methods,” *Mathematics of Computation*, Vol. 37, No. 155, 1981, pp. 141–158.
- ⁷²Nayroles, B., Touzot, G., and Villon, P., “Generalizing the finite element method: Diffuse approximation and diffuse elements,” *Computational Mechanics*, Vol. 10, 1992, pp. 307–318.
- ⁷³Wendland, H., “Piecewise polynomial, positive definite and compactly supported radial functions of minimal degree,” *Advances in Computational Mathematics*, Vol. 4, 1995, pp. 389–396.
- ⁷⁴Arya, S., Mount, D. M., Netanyahu, N. S., Silverman, R., and Wu, A. Y., “An optimal algorithm for approximate nearest neighbor searching fixed dimensions,” *J. ACM*, Vol. 45, No. 6, Nov. 1998, pp. 891–923.
- ⁷⁵Demasi, L., Gordnier, R. E., Santarpia, E., and Dipace, A., “High-Fidelity Simulations of a Flexible Flapping Wing in Forward Flight,” No. AIAA 2013-1648, 54th AIAA/ASME/ASCE/AHS/ASC Structures, Structural Dynamics, and Materials Conference, Boston, Massachusetts, American Institute of Aeronautics and Astronautics, 8-11 April 2013.
- ⁷⁶Kier, M. T., “Comparison of Unsteady Aerodynamic Modelling Methodologies with Respect to Flight Loads Analysis,” *AIAA Atmospheric Flight Mechanics Conference and Exhibit Guidance, Navigation, and Control and Co-located Conferences*, No. AIAA 2005-6027, August 2005.
- ⁷⁷Attar, P. J., Dowell, E. H., and White, J., “Modeling the LCO of a delta wing using a high fidelity structural model,” Vol. 3, 2004, pp. 1986 – 2000.
- ⁷⁸Lucia, D., “The SensorCraft Configurations: A Non-Linear AeroServoElastic Challenge for Aviation,” No. AIAA 2005-1943, 46th AIAA/ASME/ASCE/AHS/ASC Structures, Structural Dynamics and Materials Conference, American Institute of Aeronautics and Astronautics, 18-21 April 2005.
- ⁷⁹Patil, M. J., “Nonlinear Aeroelastic Analysis of Joined-Wing Aircraft,” 2003, Presented at the 44th AIAA/ASME/ASCE/AHS/ASC Structures, Structural Dynamics & Materials Conference, Norfolk, Virginia, April 7-10, 2003.
- ⁸⁰Demasi, L., Cavallaro, R., and Bertucelli, F., “Post-Critical Analysis of Highly Deformable Joined Wings: the Concept of Snap-Divergence as a Characterization of the Instability,” 2013, Submitted for Publication.
- ⁸¹Murua, J., Palacios, R., and Graham, J. M. R., “Applications of the unsteady vortex-lattice method in aircraft aeroelasticity and flight dynamics,” *Progress in Aerospace Sciences*, Vol. 55, No. 0, 2012, pp. 46 – 72.
- ⁸²Bernardini, G., *Problematiche Aerodinamiche Relative alla Progettazione di Configurazioni Innovative*, Ph.D. thesis, Politecnico di Milano, Nov 1999.
- ⁸³Prandtl, L., “Induced Drag of Multiplanes,” Tech. Rep. TN 182, NACA, March 1924.
- ⁸⁴Frediani, A. and Montanari, G., “Best wing system: an exact solution of the Prandtl’s problem,” *Variational Analysis and Aerospace Engineering*, Vol. 33 of *Springer Optimization and Its Applications*, Springer New York, 2009, pp. 183–211.
- ⁸⁵Demasi, L., Dipace, A., Monegato, G., and Cavallaro, R., “An Invariant Formulation for the Minimum Induced Drag Conditions of Non-planar Wing Systems,” *AIAA Journal*, 2014, In press.
- ⁸⁶Demasi, L., Monegato, G., Dipace, A., and Cavallaro, R., “Minimum Induced Drag Theorems for Joined Wings, Closed Systems, and Generic Biwings,” In Preparation.
- ⁸⁷Quaranta, G., Mantegazza, P., and Masarati, P., “Assessing the local stability of periodic motions for large multibody nonlinear systems using POD,” *Journal of Sound and Vibration*, Vol. 271, 2003, pp. 1015–1038.
- ⁸⁸Moore, E. H., “On the reciprocal of the general algebraic matrix,” *Bulletin of the American Mathematical Society*, Vol. 26, pp. 394–395.
- ⁸⁹Barata, J. C. A. and Hussein, M. S., “The Moore-Penrose Pseudoinverse. A Tutorial Review of the Theory,” 2011.